UNIVERSITÀ DEGLI STUDI DI TRIESTE

XXX CICLO DEL DOTTORATO DI RICERCA IN INGEGNERIA E ARCHITETTURA

ANTENNA AND RANDOM ACCESS SOLUTIONS FOR NANOSATELLITE AND 5G NETWORKS OPERATING IN THE MILLIMITER-WAVE DOMAIN

Settore scientifico-disciplinare: ING-INF/03 Telecomunicazioni

DOTTORANDO
ALESSANDRO CUTTIN

COORDINATORE
Prof. DIEGO MICHELI

SUPERVISORE
Prof. MASSIMILIANO COMISSO

CO-SUPERVISORE
Prof. FULVIO BABICH

ANNO ACCADEMICO 2016/2017

UNIVERSITÀ DEGLI STUDI DI TRIESTE

XXX CICLO DEL DOTTORATO DI RICERCA IN INGEGNERIA E ARCHITETTURA

ANTENNA AND RANDOM ACCESS SOLUTIONS FOR NANOSATELLITE AND 5G NETWORKS OPERATING IN THE MILLIMITER-WAVE DOMAIN

Settore scientifico-disciplinare: ING-INF/03 Telecomunicazioni

DOTTORANDO
ALESSANDRO CUTTIN .....

COORDINATORE
Prof. DIEGO MICHELI .....

SUPERVISORE
Prof. MASSIMILIANO COMISSO .....

CO-SUPERVISORE
Prof. FULVIO BABICH

ANNO ACCADEMICO 2016/2017

There are two kinds of thesis:
a good thesis and a done thesis.

S. Z. Sternberg

Sommario

L'obiettivo di questa tesi è la discussione di soluzioni tecniche per reti satellitari basate su nanosatelliti e reti 5G, operanti in onde millimetriche. I contributi originali di questo lavoro interessano due settori che ricoprono un ruolo chiave nel contesto delle comunicazioni digitali ad alta velocità e alta capacità: i meccanismi di condivisione del mezzo trasmissivo basati sull'accesso casuale e le antenne a schiera riconfigurabili e compatte. I risultati ottenuti in questi due ambiti sono poi applicati in un'architettura di rete che integra sistemi 5G terrestri e una costellazione di nanosatelliti in orbita bassa.

Le comunicazioni satellitari sono sempre più parte integrante della vita quotidiana: broadcasting, posizionamento e comunicazioni personali sono applicazioni ormai comuni, senza contare quelle scientifiche e militari. Negli ultimi anni, si è registrata una crescita notevole dei piccoli satelliti (da 1 a 100 kg), sia in termini di tecnologia, che di frequenza di utilizzo. Non solo vengono lanciati in gran numero, ma si è iniziato ad utilizzarli in costellazioni da diverse decine di unità. Questa attività è l'indicatore di una prospettiva ormai prossima: gli sviluppi nel settore dell'Information and Communication Technology hanno avviato diverse iniziative che puntano ad utilizzare megacostellazioni di satelliti come reti per la fornitura di servizi di comunicazione a banda larga.

Lo sfruttamento delle onde millimetriche rappresenta quindi un punto cardine per soddisfare la crescente richiesta di capacità dei sistemi radio di prossima generazione. Inoltre, lo scenario che ne risulta è tale da richiedere una connettività completa, così che ogni satellite operi come un nodo di rete a tutto tondo, con possibilità di collegamento tra la terra e lo spazio, e da satellite a satellite.

In tale contesto, il ricorso a moderne tecniche di accesso casuale è particolarmente indicato. Negli ultimi anni si è assistito a un rinnovato interesse per i protocolli di tipo Aloha, grazie alla possibilità di dotare i ricevitori di sistemi di cancellazione dell'interferenza. A tale proposito, viene presentato un nuovo algoritmo che affianca alla cancellazione iterativa di interferenza lo sfruttamento dell'effetto cattura, tenendo al tempo stesso presente la possibile non idealità della cancellazione, e quindi la presenza di un residuo. Le sue prestazioni sono confrontate con i metodi attualmente adottati negli standard, mostrando un miglioramento del throughput maggiore del 30 %.

Viene inoltre presentata la sintesi di un'antenna a schiera operante in banda Ka adatta per l'uso su nanosatelliti. La schiera risultante offre interessanti benefici in termini di larghezza di banda, polarizzazione e versatilità, essendo possibile un utilizzo dual-task (downlink verso terra e collegamento intersatellitare).

I risultati così ottenuti sono poi utilizzati per dimostrare, in un simulatore tempo discreto ed evento discreto, le prestazioni ottenibili da un'architettura di rete integrante segmenti di rete radiomobile 5G con una dorsale costituita da una costellazione di nanosatellti. Il simulatore si avvale inoltre di un modello teorico per valutare l'impatto della distribuzione geometrica dei nodi interferenti su una comunicazione in onde millimetriche di tipo line-of-sight. Tale modello, validato con simulazioni di tipo Monte Carlo, contempla i diagrammi di radiazione delle antenne e i recenti modelli di canale in onde millimetriche, che tengono in considerazione rumore, dispersione angolare, fading e bounded path loss. Sono state ricavate delle formulazioni analitiche per la distribuzione della potenza di rumore e interferenza, che consentono di valutare in forma chiusa la probabilità di cattura. Tale impostazione è stata infine usata per discutere gli effetti dell'interferenza sulla capacità di un collegamento in uplink operante in onde millimetriche, prendendo in considerazione delle condizioni realistiche per il canale.

Contents

Sommario 5

List of Figures 9

List of Tables 11

Acronyms 13

Symbols 17

I Background 19

1 Introduction 21

2 Modern random access methods 25
2.1 Aloha . . . 26
2.2 Slotted Aloha . . . 27
2.3 Diversity Slotted Aloha . . . 28
2.4 Modern Random Access methods . . . 29
2.5 Coded Slotted Aloha . . . 36
2.6 Modern random access and 5G . . . 37

3 Antenna technologies for small satellites in the mm-wave domain 41
3.1 Microstrip antennas . . . 42
3.2 Design workflow for a rectangular patch antenna . . . 46
3.3 Techniques to achieve circular polarization . . . 48
3.4 Design of singly fed circularly polarized patch antennas . . . 49
3.5 Bandwidth widening . . . 50
3.6 Optimization of the design . . . 51
3.7 Antenna arrays . . . 52
3.8 Reflectarrays . . . 54

II Original Results **57**

4 Random multiple access uplink in 5G millimeter-wave cellular networks **59**
4.1 Introduction 59
4.2 System and channel models 60
4.3 IDIC receiver 63
4.4 Numerical Results 67
4.5 Summary 73

5 Phased Array Design for Extending CubeSat Operations to Ka-band **77**
5.1 Introduction 77
5.2 Array structure 79
5.3 Pattern synthesis 83
5.4 Feasibility aspects 85
5.5 Summary 88

6 Nanosatellite–5G networks integration in the millimeter wave domain **91**
6.1 Introduction 91
6.2 Scenario 93
6.3 PHY layer 96
6.4 MAC layer 100
6.5 NET and higher layers 106
6.6 Application 107
6.7 Summary 110

7 Conclusions **113**

A Proof of Proposition 1 **115**

B Proof of Proposition 2 **117**

C Proof of Proposition 3 **119**

D BA-CGR algorithm **121**

Bibliography **125**

List of Publications **135**

List of Figures

2.1 The Aloha System. 27
2.2 Throughput comparison for Aloha and SA. 28
2.3 Throughput comparison for DSA, SA, and Aloha. 29
2.4 Illustrative example of replicas transmitted in a RAF. 32
2.5 Decoding procedure 32
2.6 Bipartite graph representation of the RAF in Figure 2.4. 33
2.7 Throughput upper bound of CRDSA for different values of $\iota_{\max}$. . 35
2.8 Comparison of SA, CRDSA and IRSA 36
2.9 Frame structure for CSA. 37
2.10 Comparisong of the throughput versus normalized offered traffic for IRSA and CSA. 38

3.1 Geometry for circular polarization: a square patch with mitered corners. 49

4.1 Throughput vs. input load at different iterations 66
4.2 Throughput vs. input load for IDIC-1 with $\iota_{\max} = 10$ in different channel conditions. 70
4.3 Throughput vs. input load for IDIC-2 with $\iota_{\max} = 10$ in different channel conditions. 72
4.4 Throughput vs. input load in the presence of path-loss, shadowing, and fading for $\iota_{\max} = 10$ and different SINR thresholds. 74

5.1 Mechanical mock-up of a 1U CubeSat. 80
5.2 Subarray building block: (a) front-view design, (b) side-view design. 80
5.3 Subarray building block: fabricated prototype. 81
5.4 Subarray performance: (a) return loss, (b) 2D gain pattern cuts in the $x - z$ plane, (c) 2D gain pattern cuts in the $y - z$ plane. 82
5.5 Array structure: front view. 84
5.6 Array structure: back view (feeding network). 84
5.7 Reconfigurable array performance: (a) return loss, (b) 2D gain pattern cuts for task 1, (c) 2D gain pattern cuts for task 2. 86

6.1 End-to-end communication scenario. 92
6.2 Network architecture. 95

6.3 Ccdfs of the SINR: (a) terrestrial links, (b) space links (a: analysis, s: simulation). 101
6.4 TU MAC frame. 102
6.5 SU MAC frame. 105
6.6 Channel efficiency as a function of the instantaneous offered load for the CSA and CRDSA schemes in the presence and in the absence of capture. 106

List of Tables

4.1 IDIC and compared schemes settings 65
4.2 Adopted parameters 65
4.3 Results of the paired-sample Student's *t*-test to evaluate the equivalence between simulation with fixed and variable topology. 68

5.1 Link budget for task 1 (CubeSat-ground station downlink). 89
5.2 Link budget for task 2 (intersatellite communication). 90

6.1 PHY layer parameters 98
6.2 MAC layer parameters. 105
6.3 Application parameters. 108
6.4 Performance as a function of the number of MSs per cell and BSs visible to a nSAT. 108
6.5 Performance as a function of the nSAT buffer size. 111

Acronyms

5G 5th Generation wireless systems.

ACK ACKnowledgment.

ADCS Attitude Determination and Control Subsystem.

AR Axial Ratio.

BA-CGR Buffer Aware CGR.

BL Bundle Layer.

BP Bundle Protocol.

BS Base Station.

CCSDS Consultative Committee for Space Data Systems.

CDMA Code Division Multiple Access.

CGR Contact Graph Routing.

CP Circular Polarization.

CRDSA Contention Resolution Diversity Slotted Aloha.

CRDSA++ Contention Resolution Diversity Slotted Aloha++.

CSA Coded Slotted Aloha.

CSMA Carrier Sensing Multiple Access.

DAMA Direct Assignment Multiple Access.

DSA Diversity Slotted Aloha.

DTN Delay/disruption Tolerant Networking.

DVB-RCS2 Digital Video Broadcasting - Return Channel Satellite 2.

DVB-S2 Digital Video Broadcasting - Satellite 2.

EIRP Effective Isotropic Radiated Power.

FSA Framed Slotted Aloha.

FSPL Free Space Path Loss.

HPBW Half-Power BeamWidth.

IDIC Iterative Decoding and Interference Cancellation.

IoT Internet of Things.

IP Internet Protocol.

IRSA Irregular Repetition Slotted Aloha.

ISARA Integrated Solar Array and Reflectarray Antenna.

LDPC Low-Density Parity-Check.

LEO Low Earth Orbit.

LHCP Left Hand CP.

M2M Machine to Machine.

MAC Medium Access Control.

MS Mobile Station.

NS3 Network Simulator 3.

pdf probability density function.

PHY PHYsical.

RA Random Access.

RAF Random Access Frame.

RFID Radio Frequency IDentification.

RHCP Right Hand CP.

RTT Round Trip Time.

rv random variable.

SA Slotted Aloha.

SAR Synthetic Aperture Radar.

SIC Successive Interference Cancellation.

SINR Signal to Interference plus Noise Ratio.

SNR Signal to Noise Ratio.

SoI Signal of Interest.

UDP User Datagram Protocol.

WSN Wireless Sensor Network.

Symbols

G Normalized logical MAC channel load.

ι Iteration in a SIC process.

$\iota_{\mathbf{max}}$ Maximum number of iterations.

λ Rate of Poisson arrival process.

$\mathtt{R}$ Rate of a repetition based RA scheme.

$\mathtt{r}$ Number of packet replicas transmitted in a RAF.

S Normalized logical MAC channel throughput.

τ_p Time duration of a packet in a SA scenario.

Part I

Background

Chapter 1

Introduction

The work presented in this thesis stems from the title of the grant that sponsored the doctoral research: *innovative broadband telecommunication systems using satellites for safety, prevention, and disaster relief*[1]. It has been carried out within the Telecommunication Group at the Department of Engineering and Architecture at the University of Trieste, during the three year doctoral course in Engineering and Architecture.

Each year, satellite communications are more and more becoming an integrating part of the daily life, in a direct or indirect way. Examples are countless: broadcasting, positioning, personal communications, earth imaging, and so on, without mentioning scientific and military applications. Furthermore, space technology is reactive enough to the demands of new emerging markets, so that the number of applications based on satellite solutions is constantly growing.

Recent years have been characterized by a significant increase of the share of Low Earth Orbit (LEO) satellites in the market, with a consistent growth, both in numbers and in technology of spacecrafts in the 1 kg to 100 kg range. A specific type of small satellites, the CubeSat, has attracted the attention and interest of many space operators, and continue to do so. Many sectors like Machine to Machine (M2M), Internet of Things (IoT), weather forecasts, earth observation, telecommunications can be very well served by the small satellites market and can also take advantage of the frequent re-visit times guaranteed by LEOs.

This class of small satellites has distinguished itself from other space platforms for its unconventional approach: by using mostly Commercial Off-The-Shelf (COTS) devices (that is, non necessarily space graded) and a small and modular form factor, it proved to traditional space actors that shorter development times (from mission inception to launch) and smaller costs are achievable targets. Manufacturers have also been able to standardize their small and nanosatellite platforms, which rapidly reduces the timeframe in

[1]The original title of the grant is *Sistemi di telecomunicazione innovativi a larga banda anche con impiego di satelliti per utenze differenziate in materia di sicurezza, prevenzione e intervento in caso di catastrofi naturali*, "Progetto Giovani Ricercatori" MIUR.

which they take to produce. Thanks to the most recent adaptive digital technology, they are able to provide payloads suitable for a variety of missions.

In the past, small and nanosatellites were mostly used by the scientific community, with the main purpose of validating new technology. Then, they started to represent also a way to provide a standard platform for institutions that usually did not have access to space [1]. Later on, also the industry recognized the benefits of their adoption, enabling the development of a new stream of space based applications. Since then, the capabilities of small satellites have advanced in an unprecedented way: high resolution imagery, Synthetic Aperture Radar (SAR) applications and video streaming have become common services provided by spacecrafts as small as 500 kg. Thanks to their inherent standardization, small and nanosatellites have a high degree of flexibility and, in turn, technology on board can be regularly updated. Such qualities have enabled the industry operators to become more agile and responsive to their end users' needs.

More recently, these apparently simple satellites are launched in great numbers, carried by rockets with dedicated upper stages, bringing the overall capacity up to one hundred satellites per launch[2]. Not only they are launched in great numbers, but also they have started to be used in swarms (since these are not proper constellations like the GPS, or Iridium and Globalstar), counting several tenths of spacecrafts per constellation. This is somehow an indicator of the trend for the future: the recent developments of the information technology and media sector have led to a number of initiatives in the satellite communication sector, where LEO megaconstellations satellite networks based on hundreds to thousands of small satellites will contribute to the delivery of broadband services. A confirmation of this evolution is the number of companies (like Planet, Spire, OneWeb, LeoSat, and Sky and Space Global) that develop a space infrastructure based on large constellations to provide a variety of services, sometimes opening completely new market niches.

Over the past years there has been a dramatic change in the demand of broadband services, caused by the radical change on how individuals consume digital content, mainly on mobile and portable devices. As a result, high speed data connectivity is in high demand. This change is reflected also on nanosatellite technology.

Consequently, as more initiatives seek out to use CubeSats as their main platform, the adoption of standards and best practices has grown. This, in turn, creates a new set of technical challenges, one of them being the necessity of overcoming the bandwidth limitation of radio systems, especially in the downlink. As a matter of fact, scientific and technological payloads are already capable of generating great amounts of data, causing the downlink to be overloaded. Only in the very recent years standard communication wave-

[2]PSLV-C37 Successfully Launches 104 Satellites in a Single Flight `https://www.isro.gov.in/update/15-feb-2017/pslv-c37-successfully-launches-104-satellites-single-flight`.

forms and protocols have been considered; for example the Digital Video Broadcasting - Satellite 2 (DVB-S2), but also the Consultative Committee for Space Data Systems (CCSDS).

Given these premises, the rise of megaconstellations and the increasing adoption of standardized solutions, the scenario that emerges is one where a small satellite is no more an isolated guest of LEO orbits, but it is instead a network node, with connection capabilities both from space to earth (and back), and from space to space. Therefore, not only it will operate in an environment where Round Trip Times (RTTs) are not negligible, but also it will contend the channel with a large number of nodes. In such a scenario it would probably be essential to resort to modern Random Access (RA) techniques, because of the impracticalities deriving from centralized or distributed coordination strategies. With this problem under consideration, a contribution of this work is to consider and improve suitable RA methods to be adopted at the Medium Access Control (MAC) layer of future nanosatellites constellations.

A step forward towards the capacity increase for the space downlink is represented by the exploitation of the millimeter wave bands, between 30 and 300 GHz, in order to acquire the necessary bandwidth and then support high data rates. Their use has been recently identified as a key point for satisfying the huge capacity demand of forthcoming wireless systems [2]. Previously used mainly for large satellites providing broadcasting services, given the commercial availability of Ka-band [3], millimeter-waves (mmWaves) are now under consideration also for small devices in both the space and terrestrial contexts.

These bands are characterized by severe attenuations, mainly due to pathloss and atmospheric absorption. Therefore, given the power constraints imposed by the CubeSat platform (available radiofrequency power is usually of few watts), antennas result to be an essential element to establish a communication link. Accordingly, several research groups are developing antenna systems and transceivers for LEO satellites operating in the K-bands, with a specific interest on CubeSats. In this work, a solution for an antenna providing high directivity, while being at the same time compact and lightweight, is identified. In addition, it is suitable to be used for the space to earth downlink, and also for Inter-Satellite Links (ISLs).

Beside this evolution in spacecraft communications, another technological outbreak is expected to arrive from the realization of the next-generation 5th Generation wireless systems (5G) terrestrial network, in which millimeter waves represent, together with massive multiple input multiple output and densification, one of the *big three* requirements to overcome the capacity limitations of current microwave cellular systems [4]. It is foreseen that the 5G system will be also supported by satellite network segments (for example, to improve coverage), to achieve an integrated network approach. A proposal for such integration is given, by integrating the aforementioned RA MAC schemes and antenna solutions with a Delay/disruption Tolerant Network-

ing (DTN) higher layer.

The thesis is organized in two parts. The first part provides the background material and introduces the topics that will be of interest for the research contribution described in the second part. The second part is dedicated to the original results obtained during the doctoral studies.

With reference to the first part, Chapter 2 presents the state of the art of modern RA methods. Chapter 3 identifies antenna technologies suitable for nanosatellites platforms.

The second part contains the original results. Chapter 4 presents a new receiver to be adopted together with advanced random access protocols that benefit from Successive Interference Cancellation (SIC) in an uncoordinated access scenario. Chapter 5 deals with a reconfigurable phased-array design for CubeSat downlink operations in the Ka-band; simulations and measurements results are presented. Chapter 6 describes a novel network architecture for a hybrid nanosatellite–5G system operating in the millimeter wave domain. Additionally, this chapter provides an accurate analysis of the statistic of the signal to interference-plus-noise ratio and of the capture effect for each link is carried out by accounting for the impact of interference, shadowing, fading, and noise. Finally, Chapter 7 summarizes the thesis contributions and the most relevant conclusions.

Chapter 2

Modern random access methods

When a multiple access scenario is considered, there are essentially two ways of sharing the communication channel:

1. users are coordinated by a single authority, that grants the permission to transmit in an ordered fashion, or
2. users are not coordinated, and use instead a set of rules (or algorithms) with which all nodes are configured from the beginning.

In the first case, known as Direct Assignment Multiple Access (DAMA), the coordination between users and the authority requires the exchange of certain information for the resource allocation (in a sort of a three-way handshake), which generates some overhead before the transmission of the actual information may occur.

In the second case, RA is probably one of the simplest and at the same time very widely used technique to share a communication channel among multiple users. Its use spans from satellite networks to ad hoc and cellular scenarios: this was true in the 1970s, when this technique was devised, and still holds today. While it introduces in the system the risk of collisions (that is, overlapping communications), it remains a solid alternative when the nature of the channel is such that carrier sensing and collision avoidance are unfeasible. For this reason, and also because the propagation times may add up in an unacceptable delay in the channel negotiation phase, in the realm of satellite communications, RA has been often preferred over DAMA, at least for the initiation of the information exchange.

Indeed, Carrier Sensing Multiple Access (CSMA) methods are not suitable for satellite systems, given that the packet transmission time is much shorter than the propagation delay, and therefore the nodes cannot properly carry out the sensing operation to be aware of the state of the channel. For the purposes of this thesis, when referring to RA methods, the reference is exclusively to Aloha-like protocols.

Another aspect differentiating RA from DAMA is the efficiency of the channel usage for different types of traffic. When large amounts of data are

involved, a channel negotiation is preferable, so that its capacity can be fully exploited; but a significant part of the traffic exchanged in present networks is of bursty nature, making the network commitment required for the channel reservation too costly with the actual amount of exchanged information. In this latter case, the channel is more efficiently used without the use of a negotiation, with the acceptable risk of colliding transmissions.

The problem of multiple access does not only apply to satellite communications, but also to scenarios where a potentially very large population of users who wish to transmit over a shared communication medium. Such scenarios, which are receiving an increasing attention, include, but are not limited to:

- Wireless Sensor Networks (WSNs) with a high density of sensors;
- Radio Frequency IDentification (RFID) systems with a high density of tags;
- IoT applications;
- M2M communications;
- 5G.

In these contexts, DAMA protocols may become impractical not because of the physical characteristics of the channel, but because of the large number of active users. Uncoordinated access (RA) protocols may therefore represent an appealing solution; however:

- as previously stated, they necessarily lead to collisions among packets being transmitted by the users;
- a feedback channel may not be feasible for a large population of users and for applications sensitive to delay;
- traditional RA schemes may lead to stability issues as the number of users requiring access to the channel increases.

As it will be presented starting from Section 2.4, recent *modern* Aloha protocols allow to obtain performances comparable to DAMA in terms of throughput. Their advantage is the ability to support, at the same time, a large number of uncoordinated users, in some cases even without retransmissions. In the followings, an overview of the state of the art of Aloha RA methods will be given.

2.1 Aloha

Presented in 1970 [5] as a way to provide internetworking to research centers spread in the Hawaii archipelago, the Aloha system allows nodes to transmit information packets on an uplink channel as soon as they are ready. After

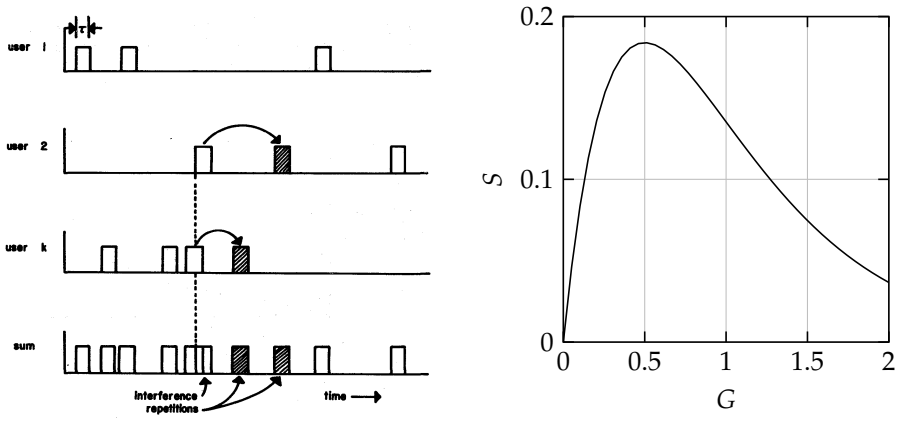

(a) (b)

Figure 2.1: The Aloha System: (a) schematic of the Aloha communication multiplexing [5], and (b) network throughput.

sending a packet, a node waits for the confirmation of its reception, that is, the ACKnowledgment (ACK), on a reliable downlink channel, also known as feedback channel. If the node does not receive the ACK, it considers the previously sent packet as lost, and sends it again on the uplink, after having waited a time interval of random duration (the backoff time), as shown in Figure 2.1(a). The radio interface of the Aloha system was designed assuming that the cause of a missing ACK was essentially the collision of two overlapping packets' transmissions, rather than an effect of poor Signal to Noise Ratio (SNR) conditions. All packets are assumed to be of the same length.

Considering an infinite population of nodes transmitting independently from one another, the rate λ of transmitted packets is also the rate of a Poisson arrival process. As previously stated, under the assumption that retransmission are due only to collisions, as shown in [5], the normalized network throughput S in packets per slot is given by

$$S = Ge^{-2G}, \tag{2.1}$$

where G is the normalized network load. The maximum throughput yielded by Aloha is $S_{\max} = 1/2e$ for a load $G^* = 0.5$.

2.2 Slotted Aloha

The first improvement on Aloha is presented in [6]. Named τ_p the time duration of a single packet transmission, in Aloha the potential conflict period is $2\tau_p$. Introducing a synchronization among all transmitting nodes, the channel can be slotted into time segments whose duration is equal to the packet transmission time. Then, nodes are required to start a packet transmission

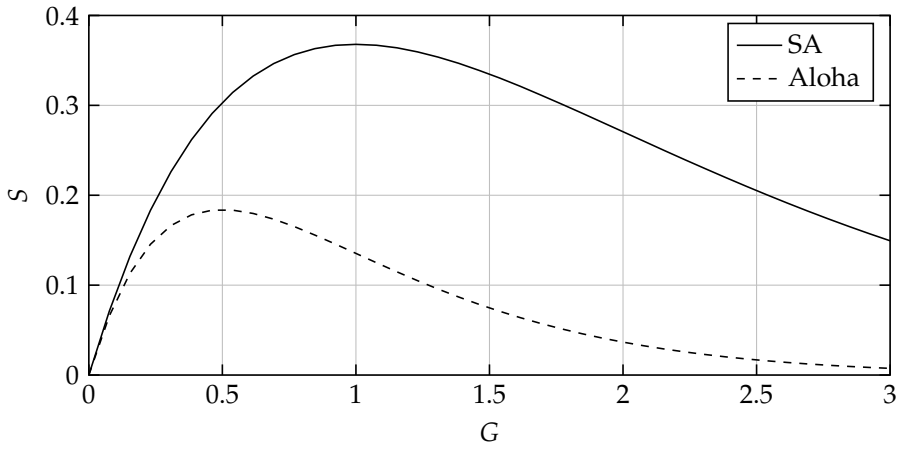

Figure 2.2: Throughput comparison for Aloha and SA.

only at the beginning of a slot. Therefore, the conflict period is reduced from $2\tau_p$ to τ_p.

Taking into consideration this new fact, the relationship between load G, intended as the average number of packet transmissions per slot, and throughput S, the probability of successful packet transmission per slot, now becomes

$$S = Ge^{-G}. \tag{2.2}$$

Therefore, the division in slots allows to double the maximum throughput, as $S_{\max} = 1/e$ for $G^* = 1$, as shown in Figure 2.2. Slotted Aloha (SA) is still adopted as the initial access scheme in both cellular terrestrial and satellite communication networks.

2.3 Diversity Slotted Aloha

Diversity Slotted Aloha (DSA) is a generalization of the SA scheme presented in the previous section. The generalization consists in the fact that each node is no longer limited at sending each packet only one time on the channel [7]. It can, instead, send $\mathtt{r} \geqslant 1$ packet replicas, each one separated by a random number of slots from the other, hoping that at least one of them will receive an ACK despite the increased channel load. In [7] this is referred to as time diversity.

According to this new enhancement, the throughput attainable for $\mathtt{r}$ replicas is

$$S = G\left[1 - \left(1 - e^{-\mathtt{r}G}\right)^{\mathtt{r}}\right]. \tag{2.3}$$

As it can be seen in Figure 2.3, packet repetition allows to achieve a slight throughput enhancement with respect to SA only at low load values. Indeed, as the injected traffic increases, replicas only contribute at generating more collisions.

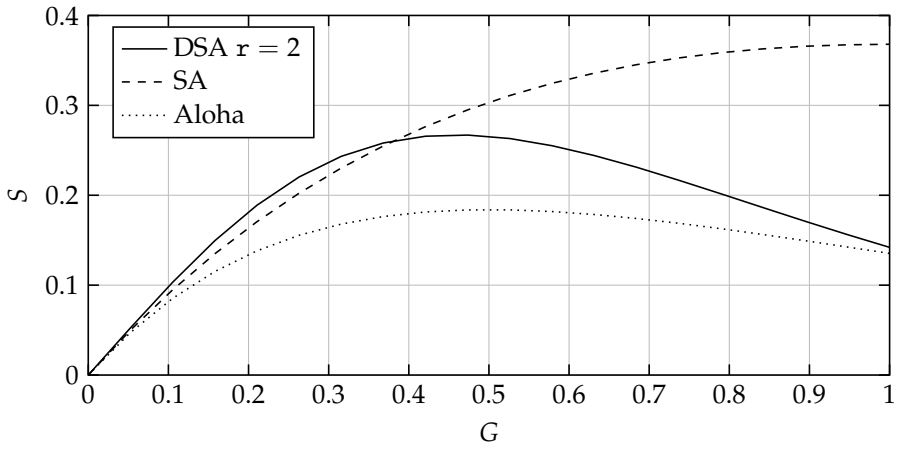

Figure 2.3: Throughput comparison for DSA, SA, and Aloha.

However, as will be seen in the next section, this improvement is a stepping stone in the development of modern RA schemes.

2.4 Modern Random Access methods

Thanks to recent advances in the implementation of SIC at the physical layer of modern receivers, a rethinking of Aloha-like RA methods has been triggered [8]. The joint capability of buffering large amounts of signal samples and of applying complex signal processing algorithms to them, allows a receiver to remove unwanted interference from the incoming signal in an iterative fashion. This brought to the development of what now are called *modern* random access schemes [9]. The introduction of SIC, previously investigated in [10] for Code Division Multiple Access (CDMA) systems, is responsible for a remarkable paradigmatic change: collisions, previously seen as destructive events to be prevented, are now embraced in the design of a new class of access protocols based on collision-resolution.

2.4.1 System model

Before describing the protocols that represent the state of the art, it is convenient to detail those aspects of the system model that they have in common.

First of all, a very large number of nodes (tending towards infinity) is considered. They transmit packets of information over a shared wireless channel to a common receiver, each having duration τ_p. Transmissions are such that each burst can be sent only within predetermined time intervals, therefore the time is *slotted*. For an asymptotically large population, the number of nodes that access the channel at any given time (that is, slot), can be modeled as a Poisson random variable (rv) of parameter λ. Then, nodes are not distributed according to a specified topology, and perfect power control is

assumed. Therefore, the capture effect is not considered [6, 11]. Multi-user detection functionalities are not available, also.

In this context, indeed common for slotted systems, the collision of two or more bursts in the same slot leads to *destructive interference*, which means that none of the collided bursts can be correctly received, unless SIC is implemented. This kind of channel is referred to as *erasure channel*, and the main consequence of its adoption is that a burst, in order to be correctly received, must be free of interference in the slot where it belongs. In the following, a burst of this kind will be referred to as *clean burst*, and the slot where it has been transmitted is called *singleton* [9].

In [9] a condition for reliable communications in an n-user Gaussian MAC channel is derived, which essentially defines an upper limit to the admissible transmission rate for each of the n nodes. The assumptions that led to its formulation, relevant for the present discussion, are the following:

1. nodes have an average power constraint,

2. each node is self aware of the maximum rate it can use, based on its own transmitted power and on a general awareness of it surrounding nodes (their number and their current rate),

3. all nodes have a message to transmit at the same time.

In a real scenario it is very likely for these assumptions not to be met, at least not all of them at the same time. Specifically, number 2 implies a certain amount of network signaling to enable each node to be aware of the active users at any given time. This may result in an unpractical level of complexity, because it requires the collection of information about the status of each node, and its subsequent retransmission to all the other nodes.

Uncoordinated RA, instead, overcomes this need, because the term *uncoordinated* refers to the fact that the access method is designed so that each node may initiate a transmission being at the same time agnostic with respect to the status of the surrounding network.

2.4.2 Iterative decoding procedure

In the scenario described in the previous section, M active nodes are considered, each attempting a packet transmission within a MAC frame. A MAC frame consists of m slots of duration $T_s = \tau_p$, so that the duration of the frame is $T_F = m\tau_p$. A node can inject in randomly chosen slots (within the same frame) a certain number $\mathtt{r}$ of replicas of the packet to be transmitted; replicas of the same packet cannot be injected in the same slot. The knowledge of where they have been transmitted is ensured by pointers contained in each replica, they indicate the slot position where the other respective copies has been sent; this is required in order to fully exploit the capabilities enabled by SIC, as will be shown in the next sections. Given this randomness in the

packets transmission, a MAC frame will be referred to as Random Access Frame (RAF).

According to the system model described early on, the RAF processing relies on the following assumptions:

- interference is destructive: the superposition of two or more packets in the same slot prevents the correct decoding of any of them;
- in presence of a clean packet, it is always correctly received (that is, ACKed);
- the interference cancellation is perfect, meaning that whenever a packet is decoded, its replicas are completely subtracted from the frame, causing no more interference.

The decoding procedure is as follows [12, 9]:

1. Upon the reception of a complete RAF, it is inspected for clean packets (or, equivalently, singleton slots).
2. Clean packets are decoded, and the pointers to their other $r - 1$ replicas are extracted.
3. The SIC process removes from the RAF the interference contribution of the replicas of decoded packets, thanks to the pointers.
4. The removal of the replicas may generate new singleton slots, so the process can be iterated from 1 (inspection for clean packets).

The steps 1–4 may be iterated as long as packets are *cleaned* by SIC, or until a maximum number of iterations $\iota_{\max}$ has been reached. It is worth noting that the decoding procedure may end even if not all packets have been decoded; this is because the superposition of the replicas in the RAF may generate *loops* that prevent the collision resolution [13].

In Figure 2.4 an illustrative RAF is shown with users that inject replicas with different repetition rates $r = \{2, 3\}$, and in Figure 2.5 the decoding process described in steps 1–4 is applied to the same RAF.

2.4.3 Bipartite graphs applied to slotted protocols

A strong connection between modern RA protocols and bipartite graphs has been formalized over the course of recent years [14, 15, 12, 16]. As a result, the general SIC process, on which modern RA protocols rely, can be described first according to this representation, and then each protocol will be presented as a particular case of this more general approach.

The status of a RAF can be described by a bipartite graph $\mathbb{G} = (\mathbb{B}, \mathbb{S}, \mathbb{E})$, where $\mathbb{B}$ is the set of burst nodes, $|\mathbb{B}| = M$, representing sent packets, $\mathbb{S}$ is the set of sum nodes, $|\mathbb{S}| = m$, each one representing one slot in the RAF, and $\mathbb{E}$ is the set of edges. An edge $e_k \in \mathbb{E}$ represents a burst replica, and therefore

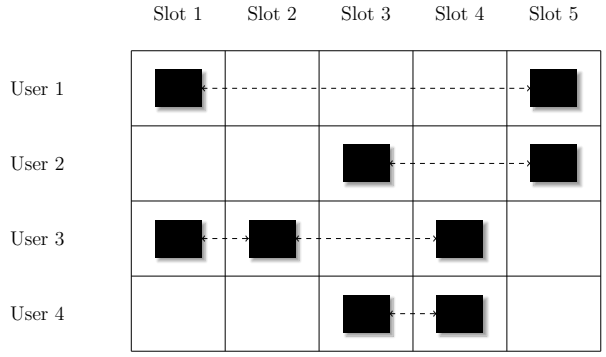

Figure 2.4: Illustrative example of replicas transmitted in a RAF [9]

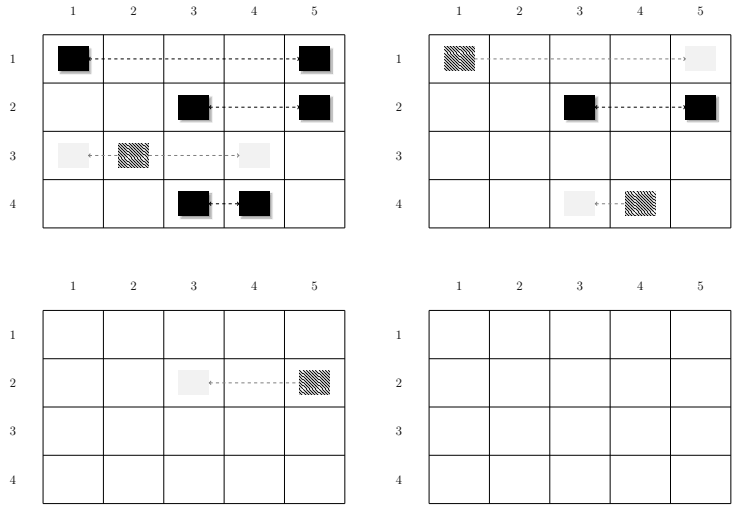

Figure 2.5: Decoding procedure of steps 1–4 applied to the RAF of Figure 2.4 [9].

connects a burst $b_i \in \mathbb{B}$ to a sum (that is, slot) node $s_j \in \mathbb{S}$ if and only if a replica of the i-th burst has been transmitted in the j-th slot. The number of edges connected to a sum node is the number of replicas colliding in that slot. If a burst has $\mathtt{r}$ replicas, its corresponding burst node will have $\mathtt{r}$ edges; this corresponds also to its degree. Modern RA protocols can be divided according to the degree of their graph's nodes. If the degree $\mathtt{r}$ is constant, the graph is called *regular*; if $\mathtt{r}$ can vary between burst nodes, instead, the graph is *irregular*. This difference has an impact on the asymptotic analysis of the protocols, which ultimately sets the achievable performance in terms of throughput [9]. An example of this analysis will be shown in the next section.

Thanks to the bipartite graph, the SIC process can be described as a message-passing along the edges of the graph, in a way equivalent to the it-

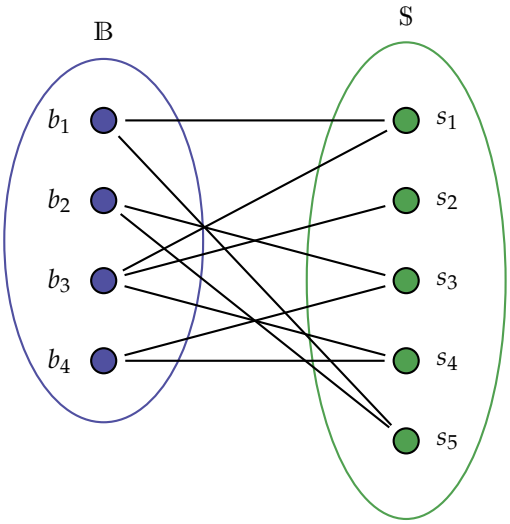

Figure 2.6: Bipartite graph representation of the RAF in Figure 2.4.

erative erasure decoding of a doubly-generalized Low-Density Parity-Check (LDPC) code [17].

Following the decoding procedure of steps 1–4, a clean packet corresponds to a sum node that has only one edge, it can therefore be removed from the graph, together with the other $r - 1$ edges connected to the same burst node. Then the search for other single-edged sum nodes can be iterated.

2.4.4 Contention Resolution Diversity Slotted Aloha

Contention Resolution Diversity Slotted Aloha (CRDSA) is a protocol with $r = 2$, therefore it originates regular graph. It represents the foundation of the new, SIC based, approach to RA [13]. Since the general workings of the protocol have been described in the previous sections, it is convenient to present its asymptotic analysis.

In CRDSA, each packet is transmitted twice on a given frame. The probability that a packet b_i (represented by the two replicas b_i^A and b_i^B) is present on a given slot s_j from the set of m slots available in one frame, assuming that slots are selected randomly with uniform probability distribution and the same slot is never selected twice, is:

$$P\{b_i \in s_j\} = P\{b_i^A \in s_j\} + P\{b_i^A \notin s_j\}P\{b_i^B \in s_j\} \tag{2.4}$$

$$= \frac{2}{m}. \tag{2.5}$$

Thus, the probability that k interfering packets are present on a given slot s_j can be derived as a binomial distribution where k packets are present in the

slot s_j and the remaining $Gm-1$ packets are not present in slot s_j:

$$P_{\text{int}}(k \mid G) = \binom{Gm-1}{k} \left[P\{b_i \in s_j\}\right]^k \left[1 - P\{b_i \in s_j\}\right]^{Gm-1-k} \tag{2.6}$$

$$= \binom{Gm-1}{k} \left(\frac{2}{m}\right)^k \left(1 - \frac{2}{m}\right)^{Gm-1-k}, \tag{2.7}$$

thanks to Equation (2.5). $Gm-1$ can also be seen as the maximum number of interfering packets that can be present in one slot. Consequently, the probability that the twin A of packet b_i is alone on a given slot s_j is equivalent to having zero interfering packets in that slot:

$$P_{\text{al}}^A(G) = P_{\text{int}}(0 \mid G) \tag{2.8}$$

$$= \left[1 - P\{b_i \in s_j\}\right]^{Gm-1} \tag{2.9}$$

$$= \left(1 - \frac{2}{m}\right)^{Gm-1}, \tag{2.10}$$

thanks to Equation (2.5). Now, given a certain system load G, the probability of successful reception of a packet during the successive interference cancellation is equal to the probability of successfully decoding it in one of the ι iteration of the SIC procedure $P_{\text{pd}}(\iota \mid G)$. By indicating with P_{pd}^A and P_{pd}^B the probabilities that the twins A and B of the same packet are successfully decoded, and by noting that $P_{\text{pd}}^A = P_{\text{pd}}^B$ because of symmetry, $P_{\text{pd}}(\iota \mid G)$ can be derived as

$$P_{\text{pd}}(\iota \mid G) = 1 - \left[\left(1 - P_{\text{pd}}^A(\iota \mid G)\right)\left(1 - P_{\text{pd}}^B(\iota \mid G)\right)\right] \tag{2.11}$$

$$= 1 - \left(1 - P_{\text{pd}}^A(\iota \mid G)\right)^2. \tag{2.12}$$

An upper bound for P_{pd}^A ca be recursively derived as follows:

$$P_{\text{pd}}^A(\iota \mid G) \leqslant P_{\text{al}}^A(G) + \sum_{l=1}^{Gm-1} \left\{P_{\text{int}}(l \mid G)\left[P_{\text{pd}}^B(\iota - 1 \mid G)\right]^l\right\} \tag{2.13}$$

recalling that $P_{\text{pd}}^A = P_{\text{pd}}^B$,

$$P_{\text{pd}}^A(\iota \mid G) \leqslant P_{\text{al}}^A(G) + \sum_{l=1}^{Gm-1} \left\{P_{\text{int}}(l \mid G)\left[P_{\text{pd}}^A(\iota - 1 \mid G)\right]^l\right\}, \tag{2.14}$$

where P_{al}^A represents the probability, given by Equation (2.10), that packet A is a clean burst, and $P_{\text{int}}(l \mid G)$, given by Equation (2.7) represents the probability that the useful burst is colliding with other k interfering bursts on the same slot. By initializing $P_{\text{pd}}^A(\iota \mid G)$ for $N_{\text{iter}} = 0$ as $P_{\text{pd}}^A(0 \mid G) = 0$, the recursion is now possible [13]. Figure 2.7 shows the achievable throughputs for some values of the maximum number of iterations $\iota_{\max}$. The peak normalized throughput (defined as the probability of successful packet transmission per slot) is $S \simeq 0.55$ for $\iota_{\max} \geqslant 10$.

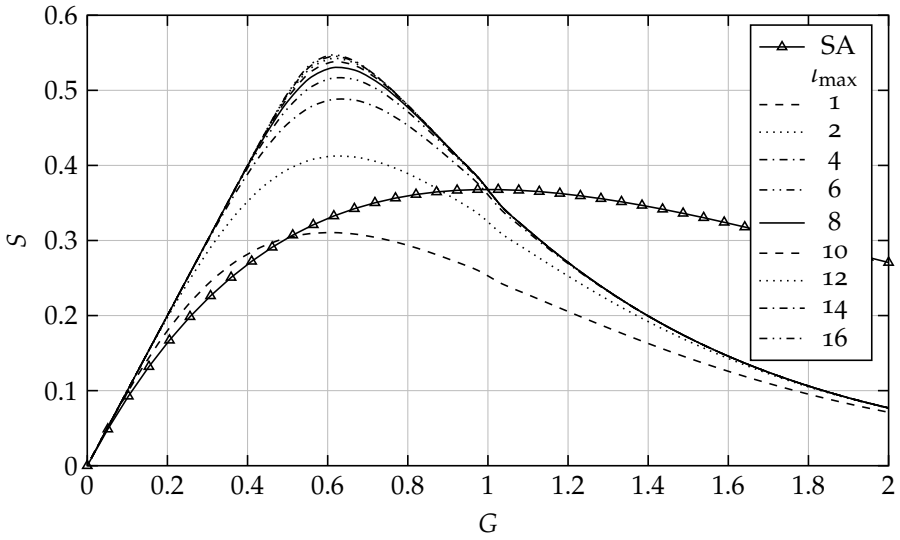

Figure 2.7: Throughput upper bound of CRDSA for different values of ι_{max}, compared with SA.

Equation (2.14) constitutes an upper bound to the throughput, because the assumed distribution of bursts in the RAF is such that every packet can be decoded, sooner or later, in the SIC process iterations. However, it may happen that two or more packets have overlapping replicas, in such a way that the SIC is not able to remove the interference, thus yielding a lower throughput.

CRDSA is currently adopted in the Digital Video Broadcasting - Return Channel Satellite 2 (DVB-RCS2) standard. Nowadays, satellite terminals are interactive and capable of transmission in the return channel. Considering the bursty nature of their traffic and the long propagation delay, adoption of CRDSA has proven to be an advance with respect to the previous state of the art [18].

2.4.5 CRDSA++

Contention Resolution Diversity Slotted Aloha++ (CRDSA++) is an improvement over CRDSA, given that repetition rates $r > 2$ are considered. Even though the collision probability increases due to the higher number of replicas injected in the RAF, this approach has proven to obtain a throughput up to $S \simeq 0.7$ [19]. CRDSA++ represents the generalization of RA protocols based on regular graphs. Further improvements are possible, as will be shown in the next section, by adopting irregular graphs.

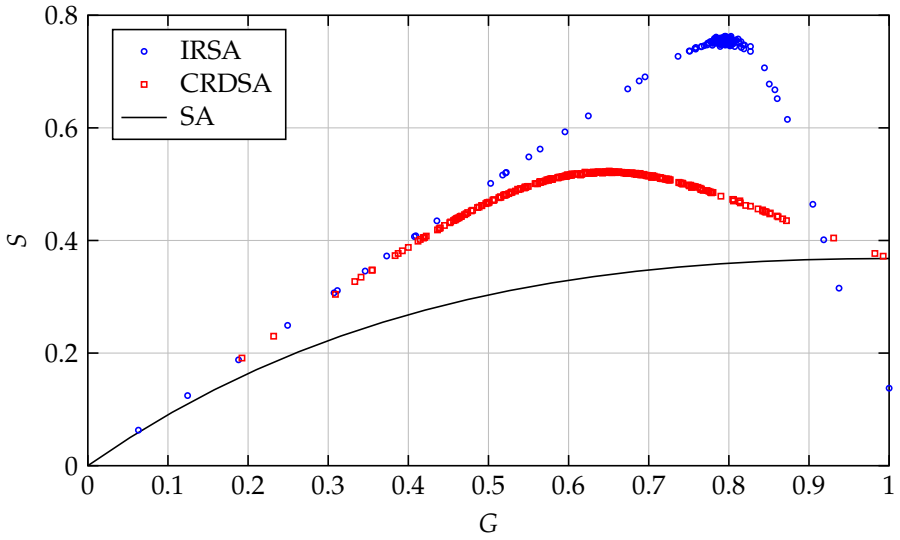

Figure 2.8: Comparison of SA, CRDSA and IRSA. For CRDSA and IRSA, results of Monte Carlo simulations are plotted.

2.4.6 Irregular Repetition Slotted Aloha

Irregular Repetition Slotted Aloha (IRSA) is a generalization of CRDSA and CRDSA++ that allows an irregular repetition rate. When transmitting a packet, a user chooses a repetition rate r according to a distribution $\{\Lambda_r\}$, which means that the probability of a user injecting r replicas into the RAF is Λ_r. The rates' distribution $\{\Lambda_r\}$ can be optimized (with the differential evolution technique) with respect to the maximum allowed repetition rate. Thanks to this approach, IRSA can achieve a throughput close to $S \simeq 0.8$ [12, 20]. Figure 2.8 compares IRSA performance to CRDSA and SA. Denoting with $\bar{r}$ the average number of replicas sent per user, the rate for the considered scheme can be defined as

$$R = \frac{1}{\bar{r}}. \tag{2.15}$$

Therefore, for repetition based schemes, $R \leqslant 1/2$.

2.5 Coded Slotted Aloha

Coded Slotted Aloha (CSA) is a generalization of IRSA in which users employ generic linear block codes, instead of repetition codes, and it is introduced as a solution to obtain rates greater than $R = 1/2$. In Figure 2.10 a comparison of CSA and IRSA schemes with the same rate R is shown.

2.5.0.1 Encoding procedure

In the CSA scheme, each packet is split into K_d data segments of the same length that are encoded to produce K segments still of the same length as the

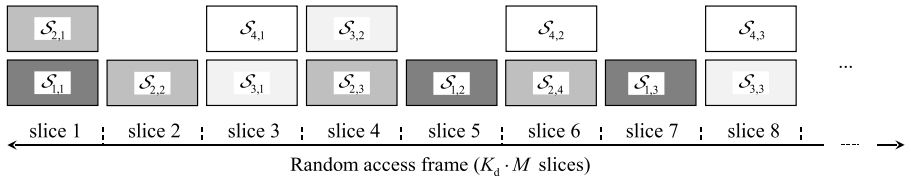

Figure 2.9: Frame structure for CSA.

data segments. At each transmission, the (K, K_d) code is randomly selected within a set $\mathtt{C}$ of possible codes according (also known by the receiver) to a given probability mass function $f_{\mathtt{C}}(K)$, which is the same for all users [20]. Besides, each slot is subdivided in K_d slices, each having the same duration of a segment.

With this approach, the rate of the scheme is

$$\mathtt{R} = \frac{K_d}{\bar{K}}, \tag{2.16}$$

where $\bar{K}$ is the expected length of the employed component code. If $\mathtt{C}$ contains only repetition codes ($K_d = 1$) then CSA reduces to the IRSA scheme.

2.5.0.2 Decoding procedure

The basic idea of CSA is to exploit the reception of at least K_d uncollided segments to decode the packet and cancel its remaining segments, thus enabling the reception of further packets whose segments were initially collided. An example of this mechanism for $K_d = 2$ is reported in Figure 2.9, where $\mathcal{S}_{n,k}$ identifies the k-th segment of the n-th packet. In this example, the Mobile Stations (MSs) 1, 3, 4 adopt a code $(3, 2)$, while the MS 2 adopts a code $(4, 2)$. According to the CSA decoding rules, packet 1 is received at the first iteration, since $\mathcal{S}_{1,2}$ and $\mathcal{S}_{1,3}$ are uncollided. Hence, $\mathcal{S}_{1,1}$ can be recovered and cancelled. This allows the reception of packet 2 at the second iteration from the segments $\mathcal{S}_{2,1}$ (cleaned) and $\mathcal{S}_{2,2}$ (uncollided), and the recovery and cancellation of $\mathcal{S}_{2,3}$ and $\mathcal{S}_{2,4}$. The remaining packets 3,4 cannot be received, since each of them has two collided segments.

2.6 Modern random access and 5G

The coming years will see the birth of the next-generation 5G network with the aim of overcoming the capacity limitations of current 3G/4G cellular systems. Within the wide set of proposals developed to achieve this objective, three enabling technologies, the so called *big three*, are expected to be surely adopted: mmWave transceivers, ultra-dense cell planning, and massive Multiple Input Multiple Output (MIMO) systems [4]. In particular, the interest in mmWaves finds its main reason in the considerable amount of bandwidth still not allocated in the range of frequencies between 30 and 300 GHz. The

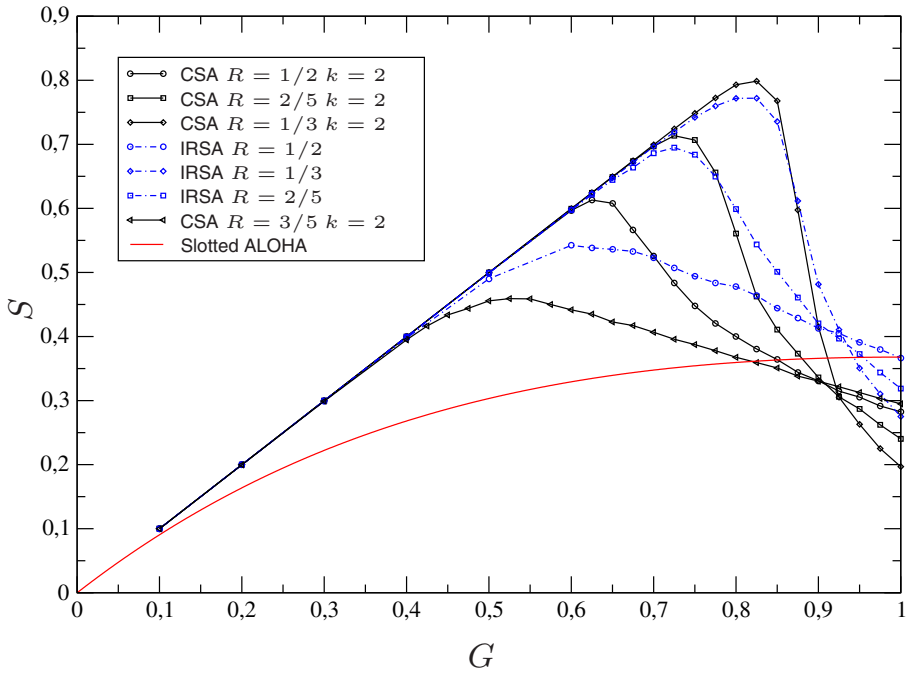

Figure 2.10: Comparisong of the throughput versus normalized offered traffic for IRSA and CSA [21].

exploitation of these currently unused resources has necessarily to deal with the considerable attenuations that characterize the mmWave channel, as compared to the conventional microwave one [22]. However, the proved usability of such frequencies through high-gain antennas [2, 23, 24], and the existence of already standardized medium access control protocols for 60 GHz wireless personal and local area networks [25, 26], have provided encouraging perspectives concerning the transition towards the mmWave portion of the radio spectrum. These advances in fact suggest the possibility of sustaining high data traffic in densely populated cells, finally making massive communication feasible.

In this scenario, a key role will be played by the multiple access protocols, which will have exactly to manage the massive access of several users. The most suitable access solution for 5G uplink/downlink operations has been identified in the Non-Orthogonal Multiple Access (NOMA) concept [27], which exploits the power diversity that necessarily occur when a station receives signals from devices located at different distances. This diversity, in fact, simplifies the application of SIC to iteratively extract the different waveforms from the received signal. To allow the communication of several users in each 5G cell, so as to give rise to a massive access scenario, the NOMA concept can be combined with the conventional Time Division Multiple Access (TDMA) approach. While, for downlink operations, a NOMA-TDMA scheme can rely on an access coordinated by the 5G Base Station (BS), the

uplink operations involving user's authentication or sporadic communication may be forced to rely on a contention-based strategy. So far, the random access procedure in cellular networks has been implemented by selecting the classic slotted Aloha protocol [28]. An Aloha-like approach is expected also for 5G networks, in which a CSMA scheme would be not applicable for the users' access because of the presence of obstacles and the lack of coordination among the mobile devices, which would make the carrier sensing mechanism unreliable [29]. However, even if the Aloha-based strategy is expected to be confirmed for 5G uplink random multiple access, novel functionalities, including NOMA, will be likely added to this scheme to improve its performance and make it capable of managing a massive access scenario. The recent advances in the implementation of SIC at the PHYsical (PHY) layer of modern receivers has in fact triggered the rethinking of Aloha-like random access methods [8]. The most significant paradigmatic change is that collisions among users' packets, previously seen as destructive events to be prevented, are now embraced in the design of a new class of access protocols based on collision-resolution [13, 12, 20]. This element, together with the considerable throughput improvements, invites to check the performance of the specific NOMA-TDMA approach represented by SIC-enabled Aloha-based schemes in ultra-dense mmWave 5G scenarios.

Chapter 3

Antenna technologies for small satellites in the mm-wave domain

It was 1957 when the first artificial satellite, the Sputnik I, was launched. This milestone in aerospace engineering has triggered the outbreak of satellites for military, scientific, commercial, and civil applications, initially driving the technology towards more and more sophisticated and, ad the same time, bigger spacecrafts. However, from later eighties, several scientists have focused their efforts towards the design of more compact equipments for cost and complexity reasons [30]. Accordingly, in the last decade, a growing number of small satellites has populated the LEO, specifically involving a recently developed novel class of devices, called CubeSats [31].

The structure of an n-unit (nU) CubeSat is made up of n cubic units, each having a volume of $1\,dm^3$, which contain the electronics and the scientific instrumentation necessary for a specific mission. The CubeSat concept was initially thought as a mean to provide hands-on experience in the field of spacecraft technology for educational and scientific purposes [32]. At this first stage, the amateur radio bands were considered sufficient for the support of the communications.

However, in a short time the real applications went well beyond the mere educational purposes. CubeSats started to attract conspicuous investments from military, government, and commercial organizations, thanks to the increased availability of off-the-shelf components and launches at reduced cost. As the design experience grew, larger and more capable CubeSats were developed to accomplish challenging missions in the fields of communication, imaging, and science [33]. In 2013 more CubeSats were launched than in all previous years [34], and, in 2014, commercial companies put into orbit more than two-thirds of the total launches [35] This has determined the need of supporting larger transfer rates, inviting the exploration of the Ka-band, beside the conventional S and X ones, to acquire the necessary bandwidth [36, 37, 38].

Previously used mainly for large satellites, mmWave, between 30 and

300 GHz, are now under consideration also for small devices in both the space and terrestrial contexts: they represent, together with densification and massive MIMO [29], the "big three" requirements to overcome the capacity limitations of current microwave cellular systems [4]. Accordingly, several research groups are developing antenna systems and transceivers for LEO satellites operating in the K-bands, with a specific interest on nanosatellites [39]. In the following sections, some guidelines for the design of antennas suitable for mmWave will be presented.

3.1 Microstrip antennas

Microstrip antennas consist of a very thin and conveniently shaped conductor[1] placed over a ground plane [40, 41, 42]. It is commonly referred to as patch, and its distance h to the ground plane is kept constant by means of a dielectric material usually named substrate. Patch antennas are usually designed so that the radiation pattern exhibits a broadside profile; this is obtained by properly choosing the mode to be excited underneath the radiating element. Nevertheless, end-fire radiation patterns can be obtained, too.

Radiation characteristics of a patch antenna depend mostly on three design parameters: the patch size, the substrate height (that is, the distance between the patch and the ground plane), and the dielectric constant of the substrate. The height, or thickness, of the substrate is generally chosen in the range

$$0.003\lambda_0 \leqslant h \leqslant 0.05\lambda_0. \tag{3.1}$$

The thicker the substrate, the more the power is radiated, the conductor loss is reduced, and the impedance bandwidth is improved. Under the same circumstances, however, dielectric loss, surface wave loss, and extraneous radiation from the probe feed become larger. The thickness has an upper limit: for example, a rectangular patch stops resonating for substrate thicknesses greater than $0.11\,\lambda_0$.

The substrate ε_r plays a role similar to that of substrate thickness: indeed, a decrease in its value yields the same effects in terms of antenna performance as does an increase in the substrate thickness. A low value of ε_r will increase the fringing field at the patch periphery, and thus the radiated power. Industrially available materials offer dielectric constants ranging from 2.1 to $13\,\mathrm{F\,m^{-1}}$ and those at the lower end of this range are preferred.

Thanks to their physical characteristics, patch antennas have a low profile and mass, and can be adapted to different kinds of surfaces; they are cost effective as well, thanks to the fact that they can be manufactured with regular printed circuit board technology. For the same reason they are easily integrated in devices produced with surface mount technology.

[1] The conductor, whose material can be chosen among those available in most manufacturing processes, can theoretically be of any shape, but simple ones like rectangles and circles are preferred in order to simplify the antenna analysis.

Even though they are a very versatile solution in terms of resonant frequency, polarization, radiation diagram and input impedance, they suffer from several limitations: low efficiency, low accepted power, low gain, low polarization purity, and high Q, which makes them very sensitive to frequency variations. Nonetheless, patch antennas are a good candidate for satellite applications, thanks to their low mass, profile and cost, ease of installation, and the fact that radiation properties – like gain – can be improved adopting an array configuration [41, 40].

3.1.1 Methods of analysis

The most common models for the study of microstrip antennas are the Transmission Line Model (TLM), which is the most simple but the less accurate[2], and the Full Wave Method (FWM), which integrates the finite elements and the finite differences methods (therefore, it is more accurate, but does not account for the physics of the radiation). Another method of widespread use is the Resonant Cavity Model (RCM), which considers the antenna as a resonant cavity, with radiation leaking from its ends [43, 44].

Patch antennas have been studied also with other techniques, as detailed in [42]. With the aperture model [41], together with the RCM [44], it has been shown that a microstrip patch antenna can be modeled by a couple of two slots of width W and height h, spaced by a distance d. The TLM explains the same situation with two slots connected by a low impedance transmission line of length d [44].

The rectangular microstrip patch is the most used configuration, and it is easy to analyze with both methods; the TLM will be used to obtain its basic design rules.

3.1.1.1 Fringing effect and radiation

Since the patch has finite length and width, the electric field lines going from the edges of the patch to the ground plane are subject to *fringing*; that is, they are not bounded in the substrate, but expand also in the surrounding region.Generally, this effect is depends on the d/h ratio, and shall be taken into account because it affects the resonant frequency. Since the field exists in a non-homogeneous medium, consisting of two different dielectrics, the main consequence of the fringing effect is to make the conductor on top of the substrate as electrically wider with respect to its real size.

Therefore, to account for this effect an *effective dielectric constant* $\varepsilon_{r\,\mathrm{eff}}$ is defined, characterizing a uniform dielectric material, so that a patch in this uniform material has the same electric characteristics as the actual one.

For a dielectric-air combination, the effective dielectric constant takes values in the interval $\varepsilon_0 \leqslant \varepsilon_{\mathrm{reff}} \leqslant \varepsilon_r$, often close to ε_r if $\varepsilon_r \gg 1$. If $W/h > 1$ the

[2]Besides this, it gives a satisfactory explanation of the radiation phenomenon.

effective dielectric constant is given by

$$\varepsilon_{r\,\mathrm{eff}} = \frac{\varepsilon_r + 1}{2} + \frac{\varepsilon_r - 1}{2}\left[1 + 12\frac{h}{W}\right]^{1/2} \tag{3.2}$$

3.1.1.2 Effective length and resonant frequency

Because of the fringing effect, the microstrip patch is electrically larger than its physical size. To account for that, the conductor needs to be extended along its length by an amount equal to Δd for each end. This correction is a function of $\varepsilon_{r\,\mathrm{eff}}$ and, when normalized to the height h, it is given by

$$\frac{\Delta d}{h} = 0.412\frac{(\varepsilon_{\mathrm{eff}} + 0.3)\left(\frac{W}{h} + 0.264\right)}{(\varepsilon_{\mathrm{eff}} - 0.258)\left(\frac{W}{h} + 0.8\right)}, \tag{3.3}$$

which is an approximate but well established relation.

Now, the resonant frequency for the dominant TM_{010} mode is a function of the patch length:

$$f_{r\,(010)} = \frac{1}{2d\sqrt{\varepsilon_r}\sqrt{\mu_0\varepsilon_0}}. \tag{3.4}$$

However, because of the fringing effect, the effective length to be considered for the resonant frequency determination is now

$$d_{\mathrm{eff}} = d + 2\Delta d. \tag{3.5}$$

Therefore, after the introduction of this correction factor, the effective resonant frequency is[3]

$$f_{r\,\mathrm{eff}\,(010)} = \frac{1}{2(d + 2\Delta d)\sqrt{\varepsilon_{r\,\mathrm{eff}}}\sqrt{\mu_0\varepsilon_0}} \tag{3.6}$$

The fringing effect is strictly related to the substrate thickness h: the thicker the substrate, the larger the fringing effect, which in turn implies a larger Δd and a lowering of the resonant frequency.

According to the available literature, different methods have been devised to find the best design for a rectangular microstrip antenna tuned at a given frequency [40, 41, 45, 46, 47].

3.1.2 Feeding techniques

Feeding methods of patch antennas can be classified in four main categories.

Microstrip The antenna is fed by a strip etched on the same substrate of the patch. To ensure impedance matching, the microstrip line is inset into the patch, realizing the so called *inset feed*.This type of feed is easy to design, but requires an accurate manufacturing. Furthermore, the level of spurious emissions increases together with the substrate thickness. An alternative to the inset feed is the quarter-wavelength adapter.

[3]From now on, when referring to the resonant frequency, the effective resonant frequency is intended, and it will be simply written as f_r for ease of notation.

Coaxial Together with microstrip, is one of the most used feeding techniques; it is easy to fabricate and to match, with low spurious emissions. The inner conductor of the coaxial cable passes through the ground plane and is attached to the patch, while the outer conductor is connected to the ground plane. However, it has a narrow bandwidth and is difficult to model for thick substrates.

Aperture coupling The drawback of inset and coaxial feed relies in the asymmetry of the feeding point, which generates higher order modes, resulting in undesired cross-polarization. The aperture coupling mitigates this problem. In this case, the antenna consists of two substrates separated by the ground plane. On the bottom face runs a microstrip line, whose fields are coupled to the patch by means of an aperture in the ground plane. In this way the patch and the feed can be dealt with separately, but the manufacturing is more complex.

Proximity coupling In this case, the final part of a microstrip line is covered by the substrate, where the patch is placed. This is the feeding that ensures the largest bandwidth [40].

3.1.2.1 Equivalent transmission line model

In order to introduce the quantities that will be later required for the feed point determination, it is now convenient to treat a microstrip antenna also according to the TLM. Each of the slots has an equivalent circuit given by an admittance Y given by the parallel connection of a conductance $\mathcal{G}$ and a susceptance B :

$$Y_1 = \mathcal{G}_1 + jB_1, \tag{3.7}$$

where for a finite width slot W it results[4]

$$\mathcal{G}_1 = \frac{W}{120\lambda_0}\left[1 - \frac{1}{24}\left(h\frac{2\pi}{\lambda_0}\right)^2\right] \tag{3.8}$$

$$B_1 = \frac{W}{120\lambda_0}\left[1 - 0.636\ln\left(h\frac{2\pi}{\lambda_0}\right)\right] \tag{3.9}$$

If coupling effects between the slots are neglected[5], using the admittance transformation equation for transmission lines the total resonant input admittance is given by

$$Y_{in} = Y_1 + Y_2 = 2\mathcal{G}_1, \tag{3.10}$$

and therefore –thanks to Equation (3.8)– is a real quantity. Consequently the input impedance is also real:

$$Z_{in} = \frac{1}{Y_{in}} = R_{in} = \frac{1}{2\mathcal{G}_1}. \tag{3.11}$$

[4]These relations hold good for $h/\lambda_0 < 1/10$.

[5]Indeed, the mutual conductance $\mathcal{G}_{12}$ is usually small compared to $\mathcal{G}_1$.

Equations 3.11 and 3.8 show that the input impedance depends more on W than on h; the substrate thickness is non influential at all for $\frac{2pih}{\lambda_0} \ll 1$. So, it appears that a way to control the input resistance is to properly chose W, as long as $W/d < 2$. It will be shown later that the input impedance can be effectively controlled with other techniques[6] [40, 41].

3.2 Design workflow for a rectangular patch antenna

A procedure to design a rectangular patch is described in this section; it assumes the knowledge of the dielectric constant of the substrate ε_r, its height h, and the resonant frequency f_r. The final results are the patch length d and width W.

3.2.1 Choice of the substrate

The first design step is to choose a suitable dielectric substrate of appropriate thickness h and loss tangent. A thicker substrate, besides being mechanically strong, will increase the radiated power, reduce the conductor loss, and improve impedance bandwidth. However, it will also increase the weight, dielectric loss, surface wave loss, and extraneous radiations from the probe feed. A rectangular patch antenna stops resonating for substrate thickness larger than $0.11\lambda_0$ ($\varepsilon_r = 2.55$) due to inductive reactance of the probe feed. A low value of ε_r for the substrate will increase the fringing field at the patch periphery, and thus the radiated power. Therefore, substrates with $\varepsilon_r \leqslant 2.5$ are preferred unless a smaller patch size is desired.

Substrate choice and evaluation are an essential part of the design procedure. Many of its properties needs to be considered: the dielectric constant and loss tangent and their variation with temperature and frequency, homogeneity, isotropicity, thermal coefficient and temperature range, dimensional stability with processing and temperature, humidity and aging, and thickness uniformity of the substrate are all of importance. The choice of a substrate for specific applications is eased by the large range of materials available: ceramic, semiconductor, ferromagnetic, synthetic, and composite. There is no ideal substrate; rather, the choice depends on the application. Substrate manufacturers have tried to combine the characteristics of various basic materials to obtain the desired electrical and mechanical properties. The resulting materials are called composite materials. By adding fiberglass, quartz, or ceramic in suitable proportion to the organic or synthetic materials, the mechanical properties are modified and the permittivity adjusted. A very wide variety of products is available with a permittivity range of 2.1 to 10, and $\tan\delta$ from 0.0005 to 0.002 at 10 GHz. All of these substrates are available in large sizes, with good mechanical properties allowing for machining, and antenna fabrication possible with standard printed circuit techniques.

[6] Other than the input resistance, patch width affects bandwidth, and, to a larger extent, cross-polarization.

Apart from the electrical and physical properties, a successful antenna design involves consideration of the properties critically involved in the antenna production process [41].

3.2.2 Determination of the patch length and width

The procedure, as proposed in [40], is as follows:

1. The width W is obtained from

$$W = \frac{1}{2f_r\sqrt{\mu_0\varepsilon_0}}\sqrt{\frac{2}{\varepsilon_r+1}}, \tag{3.12}$$

2. which – given that $W/h > 1$ – is used to calculate the effective dielectric constant $\varepsilon_{r\,\mathrm{eff}}$ of the microstrip antenna using

$$\varepsilon_{r\,\mathrm{eff}} = \frac{\varepsilon_r+1}{2} + \frac{\varepsilon_r-1}{2}\left[1+12\frac{h}{W}\right]^{-\frac{1}{2}}. \tag{3.13}$$

3. Now, using h, W, and $\varepsilon_{r\,\mathrm{eff}}$ the patch extended length Δd is given by

$$\Delta d = h\,0.412\frac{(\varepsilon_{r\,\mathrm{eff}}+0.3)\left(\frac{W}{h}+0.264\right)}{(\varepsilon_{r\,\mathrm{eff}}-0.258)\left(\frac{W}{h}+0.8\right)}, \tag{3.14}$$

4. and, finally, the patch length can be obtained from

$$d = \frac{1}{2f_r\sqrt{\varepsilon_{r\,\mathrm{eff}}}\sqrt{\mu_0\varepsilon_0}} - 2\Delta d. \tag{3.15}$$

3.2.3 Determination of feed point location for coaxial feeding

According to the TLM [40], the input resonant admittance is real and given by Equation (3.10). Therefore, the input resonant impedance of Equation (3.11) is also real. The mutual conductance (accounting for coupling effects between the slots) $\mathcal{G}_{12}$ can be neglected, being small with respect to the self conductance $\mathcal{G}_1$. The conductance $\mathcal{G}_1$ can be expressed as

$$\mathcal{G}_1 = \frac{\cos X + XS_i(X) + \operatorname{sinc} X}{120\pi^2}, \tag{3.16}$$

where

$$X = W\frac{2\pi}{\lambda_0}. \tag{3.17}$$

Using the modal-expansion analysis, the input resistance at a distance x_f from the edge, is given approximately by

$$R_{in}(x = x_f) = R_{in}(x = 0)\cos^2\left(\frac{\pi}{d}x_f\right). \tag{3.18}$$

Given the desired value of the input impedance $R_{in}(x = x_f)$ (usually $50\,\Omega$) and the antenna input impedance given by Equation (3.11), the the value of the feed inset is given by

$$x_f = \frac{d}{\pi} \arccos\left(\sqrt{\frac{R_{in}(x = x_f)}{R_{in}(x = 0)}}\right). \tag{3.19}$$

3.3 Techniques to achieve circular polarization

In general, an antenna will radiate an elliptical polarization, which is defined by three parameters: the axial ratio, the tilt angle, and the sense of rotation. The axial ratio is generally used to specify the quality of circularly polarized waves: a perfect Circular Polarization (CP) correspond to a unity axial ratio.

An antenna produces circularly polarized waves when two orthogonal field components with equal amplitude but in phase quadrature are radiated. A resonator-type antenna consists of a single patch antenna that is capable of simultaneously supporting two orthogonal modes in phase quadrature, or an array of linearly polarized resonating patches with proper orientations and phasings [41].

Microstrip patches are widely used for CP generation. Many shapes have been reported in the literature for the patch: square, circular, pentagonal, equilateral triangular, ring, and elliptical. However, square and circular patches are widely utilized in practice. A single patch antenna can radiate circular polarization if two orthogonal modes are simultaneously excited with equal amplitude and quadrature phase. This can be done with either a dual orthogonal feed (requiring an external power divider in the feeding network) or with a single feed (requiring a modification of the patch).

3.3.1 Singly fed circularly polarized patch

A single-point feed patch capable of producing CP radiation is very desirable in situations where it is difficult to accommodate dual orthogonal feeds with a power divider network. Because a patch with a single-point feed generally radiates linear polarization, in order to radiate CP, it is necessary to produce two orthogonal patch modes with equal amplitude and in-phase quadrature. This can be accomplished by slightly perturbing a patch at appropriate locations with respect to the feed.

Although various perturbation configurations for generating CP have been reported, they operate on the same principle of detuning degenerate modes of a symmetrical patch by perturbation segments. The fields of a singly fed patch can be resolved into two orthogonal degenerate modes, 1 and 2. The perturbation segments will detune the frequency response of mode 2 such that, at the operating frequency f_0, it is of the same amplitude but 90° out of phase with respect to mode 1. Hence, the two modes satisfy the required condition for CP radiation. As the frequency moves away from f_0, the axial

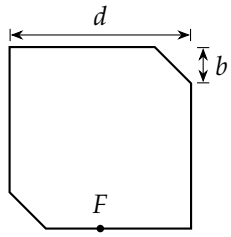

Figure 3.1: Geometry for circular polarization: a square patch with mitered corners; $d^2 = \mathtt{S}$ and $\mathtt{m}^2 = \Delta\mathtt{S}$.

ratio rapidly degrades while the input matching usually remains acceptable. The actual detuning occurs either for one or both modes depending on the placement of the perturbation segments [41].

3.4 Design of singly fed circularly polarized patch antennas

In this section, a method for designing a circularly polarized microstrip antenna with one point feed is given. The derivation is based on a variational method for the resonant frequency of a perturbed cavity as derived in [48]. The following derivation is applicable for different types of perturbations; the one chosen and considered hereinafter is reported in Figure 3.1. The squared patch is considered to be an electrically thin cavity with perfect magnetic walls at the boundaries. In the Figure 3.1, F is the feed point and $\Delta\mathtt{S} = \mathtt{m}^2$ represents the sum area of perturbation segments, and may consist of a single or multiple segments. The introduction of perturbation segments will affect the cavity modal field and its eigenvalue, which can be determined thanks to variational techniques.

If k is the eigenvalue corresponding to the fundamental mode of the unperturbed cavity (TM_{010}), the new eigenvalues k'_a and k'_b for the new fields are given by

$$k_a'^2 = k^2 \left(1 + 4\frac{\Delta\mathtt{S}}{\mathtt{S}}\right)^{-1} \tag{3.20}$$

$$k_b'^2 = k^2, \tag{3.21}$$

from which the new resonant frequencies of the degenerate modes are obtained. They are

$$f_a = f_{0r} + \Delta f'_a = f_{0r}\left(1 - \frac{\Delta\mathtt{S}}{\mathtt{S}}\right) \tag{3.22}$$

$$f_b = f_{0r} + \Delta f'_b = f_{0r}, \tag{3.23}$$

where f_{0r} is the resonant frequency of the square patch before perturbation, and $\Delta f'_a$ and $\Delta f'_b$ are the shifts in resonant frequencies for the two degenerate

modes after perturbation. The optimum frequency f_{0r} for the axial ratio is given by

$$f_0' = \frac{f_a + f_b}{2} = f_{0r}\left(1 - \frac{\Delta s}{2s}\right), \tag{3.24}$$

where $\Delta s/s < 0$ for negative perturbations.

It has been proved that the perturbation segment $\Delta s/s$ can be determined in terms of Q such that the CP radiation condition is satisfied. This is obtained by placing the feed F either on the x or y axis and by sizing the perturbation such that [48, 41]

$$\left|\frac{\Delta s}{s}\right| = \frac{1}{2Q}. \tag{3.25}$$

3.4.1 Design procedure

The general design procedure can be summarized as follows:

1. Determine the unloaded Q of the patch, which depends on dimensions d, substrate thickness h, and the substrate dielectric constant ε_r. For better accuracy on Q, it is recommended to ensure that the patch radiation efficiency is greater than 90%.
2. Determine the amount of perturbation $\Delta s/s$ from Equation (3.25).
3. The location of the feed on the axis can be selected to provide a good match; alternatively a quarter-wavelength transformer can be used for matching purpose.
4. Choose the desired sense of CP (right-hand or left-hand) by switching the feed accordingly.

Following this procedure, the resulting antenna is expected to have a good axial ratio.

3.5 Bandwidth widening

Usually, microstrip antennas are narrowband, meaning that the quality of polarization and impedance matching decreases rapidly as frequency changes from the resonant frequency. This has an impact on arrays employing them as basic elements. Nonetheless, it is possible to achieve good performance in terms of circular polarization over wide bandwidths. The axial ratio bandwidth of a CP patch is generally in the order of one-half percent, a sequential array, instead, allows to broaden the band where the polarization can be considered circular, thanks to the reduction of cross-polarization even at off-center frequencies, with an axial ratio bandwidth possibly greater than 10 % [49, 50]. The sequential rotation and phase shift is a renowned technique that enables the widening of circular polarization bandwidth of antenna arrays, formalized in [49], and it is formulated as follows.

Given an N-element planar array antenna composed of identical elements, the n-th element is located at an arbitrary position, and oriented along an angle

$$\phi_n = \frac{k(n-1)\pi}{N}, \tag{3.26}$$

where k is an integer and $1 \leqslant k \leqslant N-1$, respect to one of the elements, taken as reference. The angle ϕ_n also corresponds to the phase shift of the signal feeding the n-th element. Therefore, every element is subject to a sequential rotation and a sequential phase shift; so, the N element array is referred to as *sequential array*.

Assuming that the mutual coupling can be neglected, the polarization of the reference element in the boresight direction is considered elliptical and expressed by

$$E_1 = a\hat{u} + jb\hat{v}, \tag{3.27}$$

where $\hat{u}$, $\hat{v}$ are orthogonal unit vectors and a, b are the amplitude of the components. Then, the boresight field generated by the n-th element E_n can be expressed as

$$E_n = [(a\cos\phi_n - jb\sin\phi_n)\hat{u} + (a\sin\phi_n + jb\cos\phi_n)\hat{v}]e^{j\phi_n}, \tag{3.28}$$

and the total boresight field E radiated by the array is

$$E = \sum_{n=1}^{N} E_n = \frac{a+b}{2}N(\hat{u} + j\hat{v}). \tag{3.29}$$

This means that the sequential array radiates a perfectly circular polarized field in the boresight direction whatever the polarization of the single element.

3.6 Optimization of the design

A number of techniques to properly size and feed a rectangular microstrip patch have been proposed [40, 41, 42]. The majority of design formulas for patch antennas are based on approximate models or experimental results, they are highly sensitive with respect to the frequency, and therefore their accuracy is limited. A certain amount of error (ranging from 1 % to 2 %) should be taken into account. For this reason, an optimization technique, as proposed in [115], can be more helpful with respect to a trial-and-error process in achieving results that satisfy the project requirements. In this context, to *optimize* means to find the solution of a problem, which gives the best result with respect to certain decisional criteria (design specifications), varying a limited number of variables, and respecting certain design constraints [51].

For a patch antenna, the purpose of the optimization is to find the best values of the patch length d, width W, and feed position x_f, while evaluating the behavior of the resulting antenna. Illustrative design objectives for a patch antennas may be the resonant frequency f_r and return loss S_{11},

while the main lobe direction can be a design constraint (must be broadside). Specifically, the resonant frequency f_r should be as closer as possible to the operational center-band frequency f_0, and the reflected power (that is $|S_{11}|$), should be minimized. In the first case, the cost function is given by $|f_0 - f_r|$; in the second one, by the magnitude, expressed in dB, of $|S_{11}|$ itself. The main lobe direction is intended as a design constraint because, in the considered configuration, the patch antenna is expected to have the direction of maximum radiation along the broadside direction. If the main lobe direction is too offset from the broadside direction, the design and the corresponding set of parameters $\{d, W, x_f\}$ are considered unfeasible.

3.7 Antenna arrays

In situations where the characteristics of a single antenna are not sufficient to meet system requirements, arrays can be used. High gains or directional patterns can be obtained by a proper spatial arrangement of several radiating elements. In addition to the choice of the geometrical configuration, also the excitations of the elements can be synthesized to obtain a desired radiation pattern. Generally, for ease of analysis and design, the antenna elements are considered identical [52]. The basic principle behind the antenna array is that the field radiated from each elements interferes with those radiated from the other elements in a constructive or destructive way. The spacing or the excitations of the elements determine the directions where and how this superposition of fields occurs.

The parameters that allow control over the performance of a given array are [53, 40]:

1. the geometry that shapes the array (linear, planar, circular, ...),
2. the distance between elements,
3. the excitation amplitude of the single element,
4. the excitation phase of the single element,
5. the radiation pattern of the single element.

All of these elements contribute to the so-called Array Factor (AF). Indeed, if all the elements are identical, it is possible to analyze the array with the *pattern multiplication*, where the field radiated from the array can be seen as the product of two factors: the AF and the element factor, with respect to a given reference point:

$$\text{Total pattern} = \text{AF} \times \text{Element factor}. \tag{3.30}$$

3.7.1 Linear arrays

Linear arrays are made of radiating elements arranged along a straight line. If they are all identical, equally spaced, and have the same excitation, the

array is called uniform. For a uniform linear array with a broadside radiation pattern, the AF is given by [40]

$$\mathrm{AF} = \frac{1}{N} \frac{\sin\left[\frac{N}{2}\left(\frac{2\pi r}{\lambda_0}\cos\theta\right)\right]}{\sin\left[\frac{1}{2}\left(\frac{2\pi r}{\lambda_0}\cos\theta\right)\right]}, \tag{3.31}$$

where N is the number of elements, and r the interelement distance.

The main limitation of uniform linear arrays is that, whichever the number of elements N, the ratio between the main lobe and the first side lobe levels is limited to 13.5 dB. To overcome this issue, the assumption of uniformity may be relaxed, to introduce a proper change in the interelement distance, or the amplitude, or the phase of the excitations. Well known analytic techniques are the binomial and the Dolph–Chebyshev methods [53], and, more recently, stochastic approaches have proved to be successful, too. An example of the latter ones are genetic algorithms, that allow multi-objective optimization over multiple parameters at the same time [54].

3.7.2 Planar arrays

If the degree of freedom for placing radiating elements is increased from one to two dimensions, planar arrays can be created. So, by extending the concept of a uniform linear array, a rectangular uniform array can be obtained by placing radiating elements according to a rectangular grid. The additional degrees of freedom allow to obtain greater control over the resulting radiation pattern of the array: the level of the side lobes can be decreased, the pattern can have better symmetry with respect to a linear array, and the main beam can be pointed toward any point in space [40]. The AF of a uniform planar array is given by

$$\mathrm{AF}(\theta,\phi) = \left[\frac{1}{N_x}\frac{\sin\left(\frac{N_x}{2}\psi_x\right)}{\sin\left(\frac{\psi_x}{2}\right)}\right]\left[\frac{1}{N_y}\frac{\sin\left(\frac{N_y}{2}\psi_y\right)}{\sin\left(\frac{\psi_y}{2}\right)}\right] \tag{3.32}$$

where

$$\psi_x = \frac{2\pi r_x}{\lambda}\sin\theta\cos\phi + \beta_x \tag{3.33}$$

$$\psi_y = \frac{2\pi r_y}{\lambda}\sin\theta\sin\phi + \beta_y, \tag{3.34}$$

being r_x, r_y the spacing between elements, and β_x, β_y the progressive phase shifts along the x and y directions [40].

Again, by letting the phase of the excitation of each element to be externally controlled, the radiation pattern can be significantly changed according to a set of design requirements. This can be achieved by integrating in the array feeding network fixed or variable (analog or digital) phase shifters, one for every element. In case the phase shift is electronically controlled, the array is called phased array. Phased arrays can be used for fast scanning (compared to mechanical systems) or beam-forming [44, 55].

3.8 Reflectarrays

The microstrip reflectarray is a fairly new antenna concept. It consists of a very thin, flat reflecting surface and an illuminating feed. On the reflecting surface, there is an array of isolated microstrip patch elements [56]. The feed antenna illuminates these elements, which are individually designed to scatter the incident filed with the phase needed to form a constant aperture phase. This operation is similar in concept to the use of a parabolic reflector, which naturally forms a planar aperture phase when a feed is placed at its focus.

With this concept, the best features of a conventional parabolic reflector and of a microstrip array are merged together. For example, phase shifters can be used to scan the main beam in certain directions. The convenience of having a flat reflecting support is that the antenna can be either surface-mounted on an existing structure or easily deployed on a spacecraft to form a large aperture with a relatively small stowage volume. Having a single feed, the insertion loss of this antenna is comparable to that of a parabolic reflector [56].

To achieve the desired aperture, the reflected field from each patch must have a reflection phase such that it compensates for the differences in path length from the feed to each element in the array. Three techniques can be used to achieve this objective. The first one uses identical patches, and at each one of them a variable length open-circuit terminated transmission line stub is attached. The length of the stubs are designed to compensate for the path length differences. The second technique does not require stubs, as it uses patches of different sizes, since this changes the resonant frequency of the element, and hence its reflection phase. Patches with different sizes have different radiation impedances, and thus can be used to compensate for the path length differences. The third, for circular polarization only, can uses all identical elements. But the patches are designed with different angular rotations. This in turn changes the phase of the reflected field in a proportional way. Thus, the element angular rotations in a reflectarray can be designed to compensate for the path-length differences [56].

3.8.1 Comparison of arrays and reflectarrays for CubeSat applications

The applicability of phased-arrays to Ka-band CubeSats may be further deepened by considering the competing antenna technology based on reflectarrays [57]. In this field, the most advanced solution is the Integrated Solar Array and Reflectarray Antenna (ISARA) proposal, for which, even if the project is still under development, some preliminary numerical results are already available [39]. A comparative description of these two systems may be useful to better outline benefits and drawbacks of each technology in terms of mechanics, losses, versatility, and space available for the solar cells.

From a mechanical point of view, both antenna systems do not occupy space inside the CubeSat before the launch (except for the small packaged feed of ISARA), thus leaving more volume available to the other subsystems. ISARA requires the mechanical deployment of the panels and of the feed, which might represent a critical phase of the mission that may suffer from vibrations, heat variations, or other possible mechanical setbacks due to the launch or the space environment. Conversely, the array solution is ready to be operated as it is integrated on the spacecraft, without requiring any further intervention to be serviceable.

From the point of view of the losses, arrays are not subject to spillover (anyway minimized in the ISARA design), feed package loss, and aperture blockage, which, according to the currently available design, may instead partly affect ISARA because the feed and part of the CubeSat envelope may be not completely outside of the reflectarray aperture [39, Fig. 1]. However, these three factors, even combined, have in general an impact lower than that of the losses, due to the feeding network and the patch substrates, that characterize antenna arrays. This difference provides large benefits to ISARA, which achieves a gain of 33 dB with a 3U CubeSat. A fair comparison should anyway consider that the presented phased-array relies on a 1U CubeSat to provide a basic module, which might be replicated on more faces of an NU spacecraft to increase the gain.

From the versatility point of view, phased-arrays may be employed to support multi-task missions by pattern reconfigurability. A possibility exploited in the presented design, but not even considered in the ISARA proposal.

Finally, from the point of view of the space available for the solar cells, one may observe that the solar panels printed on the back of the ISARA reflectarray cover an area equivalent to nine 1U CubeSat faces, while five 1U CubeSat faces are available for solar panels in the proposed design. However, a scaling of the developed phase-array to a 3U CubeSat, reveals that, even considering three faces covered by three replicas of the array, eleven faces would remain accessible to solar cells. Therefore, the compactness and the conformability of the phased-array do not imply limitations for the energy supply of the CubeSat system.

Part II

Original Results

Chapter 4

Random multiple access uplink in 5G millimeter-wave cellular networks

In this chapter, a new receiver operation model is proposed for the uplink random multiple access of 5G mmWave cellular networks based on Framed Slotted Aloha (FSA) systems. The novel receiver, called Iterative Decoding and Interference Cancellation (IDIC), exploits the capture effect alongside the successive IC process to resolve collisions within each frame. The proposed system is compared with the widely adopted CRDSA scheme, which has been recently included in the DVB-S2 standard, by considering a 5G propagation scenario that is modeled in agreement with recent mmWave channel measurements and includes noise, path-loss, shadowing, and fading. This comparison reveals that a significant throughput gain is achieved by IDIC when elements of practical relevance, like imperfect cancellation and receive power diversity, are taken into account. The impact of packet and power diversity is also investigated to derive the preferable uplink random access strategy that maximizes the system throughput according to the offered channel load[1].

4.1 Introduction

As presented in Section 2.4, recent advances in the implementation of SIC have enabled a shift towards a new paradigm of Aloha-like access methods [8]. The most significant paradigmatic change is that the collision event, previously seen as something to mitigate and –possibly– to avoid, is now accepted in a renewed fashion, thanks specifically to the possibilities opened by the introduction of SIC in modern receivers. Modern random access protocols are in fact based on a collision-resolution working principle.

[1]This chapter is based on F. Babich, M. Comisso, A. Cuttin, and F. Ricciato, "Exploiting capture and interference cancellation for uplink random multiple access in 5g millimeter-wave cellular networks", *IET Communications, Special Issue on Recent Advances on 5G Communications*, under review.

According to the literature review of Section 2.4.1, the usually assumed operating conditions for a repetition-based scheme are:

1. a packet can be successfully decoded only if no other packets are present in the same slot, and

2. all copies of a successfully decoded packet can be perfectly cancelled.

Both these assumptions are restrictive for many real-world wireless systems, where the reception power variability may enable packet capture, which can occur in all radio receivers when the Signal to Interference plus Noise Ratio (SINR) of the strongest packet is sufficiently high. CRDSA is in fact suitable for satellite systems with perfect power control [58], where neglecting capture justifies the packet diversity strategy. In wide-area terrestrial systems (like, for example, LoRa® [59]), instead, power diversity is actually present, thus capture and also residual interference cannot be ignored. It is hence worthwhile to check if the by now established repetition strategy of CRDSA remains preferable when the actual SINR of the packet is taken into account, so as to infer which SIC-enabled Aloha-based scheme results preferable for implementation in 5G mmWave networks.

To address this issue, the suitability of CRDSA-like solutions for 5G systems with no (or imperfect) power control is in this work critically reconsidered by showing that, in the presence of cancellation residuals and capture, *the preferable strategy is in general hybrid and consists in sending, in each frame, only a single packet copy for high channel loads and two copies for low channel loads*. Besides, a novel receiver algorithm, called IDIC, which leverages capture alongside nonideal SIC, is proposed, and hence results suitable for implementation in 5G BS receivers for uplink random access.

To match this objective in a reliable way, it is anyway necessary to examine the system in a realistic mmWave environment, both in terms of channel model and operating conditions. By means of simulations carried out adopting a mmWave channel model adherent to the recent measurements at 28 GHz and including path-loss, shadowing, fading, and noise, we show that IDIC is more efficient than CRDSA when a realistic receiver model is considered. Most importantly, the achieved performance gain comes without any additional implementation complexity at the receiver side, since capture is a natural occurrence for any receiver.

The chapter is organized as follows. Section 4.2 introduces the system and channel models. Section 4.3 presents the IDIC receiver. Section 4.4 discusses the numerical results. Finally, Section 4.5 summarizes the main conclusions.

4.2 System and channel models

Consider M transmitting sources uniformly distributed over a 5G cell identified by a disk $\mathrm{D}(O, \rho)$ of center O and radius ρ, and a receiving BS located in

O, according to the probability density function (pdf)

$$f_{D_m,\Theta_m}(d_m,\theta_m) = \frac{1}{\pi\rho^2}\cdot\begin{cases} d_m & 0\leqslant d_m\leqslant\rho,\ 0\leqslant\theta\leqslant 2\pi \\ 0 & \text{otherwise}\end{cases}. \tag{4.1}$$

The sources send their bursts, which are generated according to a Poisson arrival process of rate λ, with an equal power P_{T} on a shared channel organized in RAFs of m slots. All sources are assumed frame- and slot-synchronous, and the burst transmission time coincides with the slot duration. Each source can send $\mathtt{r}$ copies of its burst in $\mathtt{r}$ different slots of each RAF. Successfully decoded bursts (that is, bursts whose at least one copy is correctly received) are acknowledged on a separate reliable feedback channel, while unsuccessful bursts are retransmitted in the subsequent RAF. According to the mmWave channel model [2], the power received from the generic user m ($m = 1,\dots,n$) lying at distance d_m from the BS is evaluated as:

$$p_m = \frac{P_{\mathrm{T}}G_{\mathrm{T}}G_{\mathrm{R}}\phi_m\psi_m}{1+\alpha {d_m}^{\beta}}, \tag{4.2}$$

where G_{T} and G_{R} are the transmitting and receiving antenna power gains, respectively, ϕ_m and ψ_m are the realizations of two random variables (r.v.s) Φ_m and Ψ_m modeling the mid- and small-scale fading, respectively, while α and β are the path-loss parameters. In particular, in (4.2), d_m denotes the realization of a r.v. D_m having probability density function (pdf) given by the marginal with respect to the distance of a uniform distribution in the 5G cell $\mathrm{D}(O,\rho)$ as [60]:

$$f_{D_m} = \frac{2d_m}{\rho^2}\cdot\mathbb{1}_{[0,\rho]}(d_m), \tag{4.3}$$

where $\mathbb{1}_{\mathbf{X}}(y)$ is the indicator function, that is,

$$\mathbb{1}_{\mathbf{X}}(y) = \begin{cases} 1, & y\in\mathbf{X} \\ 0, & y\notin\mathbf{X}\end{cases}. \tag{4.4}$$

The realization p_m of the r.v. P_m is evaluated using the recently introduced bounded path-loss model [61], which enables to overcome some limitations of the classic unbounded path-loss model when a user may be arbitrarily close to the BS and/or path-loss measures are not available below a certain communication range. In fact, in (4.2), the experimentally available estimations at 28 and 73 GHz of the parameters α and β [2], which represent the floating intercept and the average path-loss exponent, hold just over a certain distance from the BS.

The mid-scale fading, which is one of the most relevant propagation phenomena in mmWave communications, is assumed to follow a log-normal distribution, thus the pdf of Φ_m is given by [22]:

$$f_{\Phi_m}(\phi_m) = \frac{1}{\sqrt{2\pi}\tilde{\sigma}\phi_m}\exp\left(-\frac{\log^2\phi_m}{2\tilde{\sigma}^2}\right)\cdot\mathbb{1}_{(0,+\infty)}(\phi_m), \tag{4.5}$$

where $\tilde{\sigma}$ is the shadowing standard deviation. Besides, the small-scale fading is assumed Nakagami distributed, thus the pdf of Ψ_m is modeled by a gamma density with unit mean as:

$$f_{\Psi_m}(\psi_m) = \frac{\eta^\eta}{\Gamma(\eta)} \psi_m^{\eta-1} e^{-\eta\psi_m} \cdot \mathbb{1}_{[0,+\infty)}(\psi_m), \tag{4.6}$$

where η ($\geq 1/2$) is the Nakagami parameter and $\Gamma(.)$ is the gamma function. Observe that all the considered statistics are selected in agreement with the recent measurements carried out in the mmWave domain [2]. In particular, concerning small-scale fading, the experimental channel parameters are derived in [23] assuming a Rice distribution. However, (4.6) may be adopted [62], by recalling the relationship between the Rice factor and the Nakagami parameter [63]. According to the above described mmWave channel, each burst is subject to path-loss, shadowing, and fading, which give rise to power diversity among the different packets.

At the receiver side, the 5G BS has to manage the decoding of multiple bursts subject to random mmWave attenuations and interference, which results from the contention-based access mechanism. To manage this situation according to the CRDSA rules, at the BS side each RAF is iteratively processed up to a maximum number $\iota_{\max}$ of allowed SIC iterations. For a given RAF, denote by $\mathbb{B}_n$ the set of bursts transmitted in the generic slot n ($n = 1, \ldots, N$), and by $\mathcal{A}^\iota$ the set of bursts acknowledged until iteration ι ($\iota = 1, \ldots, \iota_{\max}$). The Signal of Interest (SoI) in slot n and iteration ι is identified by the burst received with the highest power among those remaining in that slot. If the SoI is correctly received, all of its copies are cancelled from the RAF. To successfully accomplish such cancellation, the condition required in [13, Section C.2] is the ideal estimation of the followings:

1. received signal amplitude,
2. received carrier frequency offset, and
3. burst timing.

These estimations, in turn, allow an accurate reproduction of the signal to be subtracted from the corresponding slot, but, unfortunately, estimation uncertainties occur in practical implementations. This leads to imperfect cancellation and hence residual interference, usually assumed proportional to the received power by a factor $0 < \gamma < 1$ [11]. With reference to slot n, identifying as $\mathcal{C}_n^\iota$ the set of bursts cancelled until iteration ι, one may determine the set of bursts remaining at iteration ι and containing the SoI as:

$$\mathcal{R}_n^\iota = \mathbb{B}_n \setminus \left(\mathcal{A}^{\iota-1} \cup \mathcal{C}_n^{\iota-1} \right), \tag{4.7}$$

where, in the case $\iota = 1$, $\mathcal{A}^0 = \mathcal{C}_n^0 = \emptyset$. Accordingly, the SINR of the corresponding SoI may be expressed as [64]:

$$\mathrm{SINR}_n^\iota = \max_{m \in \mathcal{R}_n^\iota} \frac{P_m}{U_{m,n}^\iota}, \tag{4.8}$$

in which the undesired power is given by:

$$u_{m,n}^{\iota} = \chi_{m,n}^{\iota} + r_n^{\iota} + w = \sum_{j \in \mathcal{R}_n^{\iota} \setminus \{m\}} p_j + \gamma \sum_{j \in \mathcal{C}_n^{\iota-1}} p_j + w, \tag{4.9}$$

where $\chi_{m,n}^{\iota}$ and r_n^{ι} represent, respectively, the interference due to the remaining (not cancelled) bursts and the residual interference due to the cancelled ones, both referred to slot n and iteration ι, while w denotes the noise power at the receiving BS. This latter quantity is evaluated as [22]:

$$w = \varrho \cdot B_{\mathrm{W}} \cdot \mathcal{F}, \tag{4.10}$$

where $\varrho \cong 3.98 \times 10^{-18}\,\mathrm{W\,Hz^{-1}}$ is the noise spectral density, B_{W} is the transmission bandwidth, and $\mathcal{F}$ is the receiver's noise figure.

Once (4.8) is evaluated, the SoI is successfully decoded, i.e., captured, if the condition:

$$\mathrm{SINR}_n^{\iota} \geqslant \xi, \tag{4.11}$$

is satisfied for a given SINR threshold ξ. This formulation provides a sufficiently general modeling of the SIC-enabled receiving system that is able to include both ideal and nonideal operation modes. In fact, by properly selecting the parameters γ and ξ, we can model both the ideal ($\gamma = 0$) and the nonideal ($\gamma > 0$) interference cancellation, as well as the absence ($\xi = \infty$) and the presence ($\xi < \infty$) of capture. The case $\xi = \infty$ indeed corresponds to the requirement of no undesired power for a correct decoding [13].

4.3 IDIC receiver

According to the system model introduced in the previous section, the IDIC receiver is explicitly designed to work in realistic operational conditions characterized by the possibility of capturing an interfered burst and the presence of imperfect cancellation. The IDIC implementation for a 5G receiving BS is summarized in Algorithm 1. The input quantities are the parameters ξ (SINR threshold), γ (fraction of residual interference), $\iota_{\max}$ (maximum number of SIC iterations), and $\mathcal{B}_n$ for $n = 1, \ldots, N$ (set of bursts present in each of the m slots of the RAF). At each iteration ι, two main operations are performed: the checking of the capture event, and the SIC of the possible copies of each captured burst. The first operation is carried out for each slot by using Equations (4.7) to (4.11) to verify if the SoI in the presence of uncancelled and residual interference can be decoded, and hence the corresponding burst $\hat{m}$ can be added to the set $\mathcal{D}$ of the bursts successfully received at that iteration. This set is then used to update the set $\mathcal{A}^{\iota}$ of the bursts decoded until iteration ι, and to perform the SIC operation, involving the update of the set $\mathcal{C}_n^{\iota}$ of the bursts cancelled in slot n until ι. The RAF processing is iterated until there are no more bursts that can be decoded or the maximum number of iterations is reached. Observe that the order of the two operations involved in the IDIC receiver, that is, capture and SIC, is not due to a choice, but to the

Algorithm 1: IDIC receiver

Input: ξ; γ; $\iota_{\max}$; W; $\mathcal{B}_n$, $n = 1, \ldots, N$
initialize: $\iota \leftarrow 1$; $\mathcal{A}^0 \leftarrow \emptyset$; $\mathcal{C}_n^0 \leftarrow \emptyset$, $n = 1, \ldots, N$;
repeat
  initialize: $\mathcal{D} \leftarrow \emptyset$;
  Capture;
  for $n = 1, \ldots, N$ **do**
    evaluate: $\mathcal{R}_n^\iota$ by (4.7);
    if $\sum_{m \in \mathcal{R}_n^\iota} P_m > 0$ **then**
      evaluate: SINR_n^ι by (4.8) and (4.9);
      if $SINR_n^\iota \geqslant \xi$ **then**
        evaluate: $\hat{m} \leftarrow \mathrm{argmax}_{m \in \mathcal{R}_n^\iota} P_m / U_{m,n}^\iota$;
        update: $\mathcal{D} \leftarrow \mathcal{D} \cup \{\hat{m}\}$;
  update: $\mathcal{A}^\iota \leftarrow \mathcal{A}^{\iota-1} \cup \mathcal{D}$;
  SIC;
  for $n = 1, \ldots, N$ **do**
    update: $\mathcal{C}_n^\iota \leftarrow \mathcal{C}_n^{\iota-1}$;
    foreach $\hat{m} \in \mathcal{D}$ **do**
      if $\hat{m} \in \mathcal{R}_n^\iota$ **then**
        update: $\mathcal{C}_n^\iota \leftarrow \mathcal{C}_n^\iota \cup \{\hat{m}\}$;
  $\iota \leftarrow \iota + 1$;
until $\mathcal{D} \neq \emptyset \wedge \iota \leqslant \iota_{max}$;
Output: $\mathcal{A}^\iota$

natural evolution of the receiving process. In fact, the capture event, when occurs, is spontaneous and cannot be driven to occur before other implemented operations. In this sense, the IDIC receiver takes note of a beneficial, yet unavoidable, random occurrence.

The IDIC scheme is a kind of message passing algorithm similar to that proposed in [65], but focused on intra-frame cancellation. Moreover, it is sufficiently general to operate also when multiple packet replicas are generated, that is, when packet diversity is implemented. Thus, in the following, IDIC-$\mathtt{r}$ will be used to denote an IDIC receiver operating when each 5G user can send $\mathtt{r}$ burst copies in each RAF to the receiving BS. This capability makes interesting a comparison, in the mmWave context, with the widely adopted CRDSA scheme, which is characterized by the usage of $\mathtt{r} = 2$ replicas of each packet in the RAF [13]. To this aim, we consider for IDIC-$\mathtt{r}$ the cases $\mathtt{r} = 1$ and $\mathtt{r} = 2$, and we select $\gamma = 0.1$ [11], and $\xi = 3\,\mathrm{dB}$ as operating values. Observe that, when CRDSA or IDIC-2 are employed, both packet copies are cancelled if at least one of them is successfully decoded, with the difference that IDIC-2 operates in the presence of radio capture, as well as nonideal SIC. Concerning this latter aspect, we consider the CRDSA performance with perfect and imperfect cancellation to have a touchstone in both

Table 4.1: IDIC and compared schemes settings

Scheme	γ	ξ (dB)	r
IDIC-1	0.1	3	1
IDIC-2	0.1	3	2
CRDSA-ideal SIC	0	∞	2
CRDSA-nonideal SIC	0.1	∞	2

Table 4.2: Adopted parameters

Parameter	**Value**
M	400
ρ	50 m [2]
P_{T}	20 dBm [2]
m	100
G_{T}	30 dB [2]
G_{R}	3 dB
α	69.8 dB (LOS), 82.7 dB (Non–Line Of Sight (NLOS)) [2]
β	2.0 dB (LOS), 2.7 dB (NLOS) [2]
$\tilde{\sigma}$	5.8 dB (LOS), 7.7 dB (NLOS) [2]
η	3 [23]
B_{W}	1 GHz [22]
$\mathcal{F}$	10 dB [22]

ideal and practical scenarios. The settings for the four compared solutions are summarized in Table 4.1.

The IDIC receiver and the CRDSA scheme are implemented in Matlab. Their performance is obtained by Monte Carlo simulations using the parameters in Table 4.2, which are inferred from the recent measurements obtained for the 28 GHz channel in both Line Of Sight (LOS) and NLOS conditions [2, 23]. In particular, the value of the Nakagami parameter η has been calculated from the Rice parameter estimated in [23], by using the conversion formula in [63, Sec. 2.1.2]. Besides, the directional transmitting antenna power gain (in dB)

$$G_{\mathrm{T}} = 10 \log_{10}(N^2) \tag{4.12}$$

derives from the usage of an array with $N = 32$ radiating elements [2]. The reception is assumed omnidirectional with a receiving power gain of 3 dB. This represents a conservative choice for G_{R} (omnidirectional antennas operating in the mmWave band with higher gains are commercially available [66]), that is specifically made to check the IDIC capabilities in ordinary

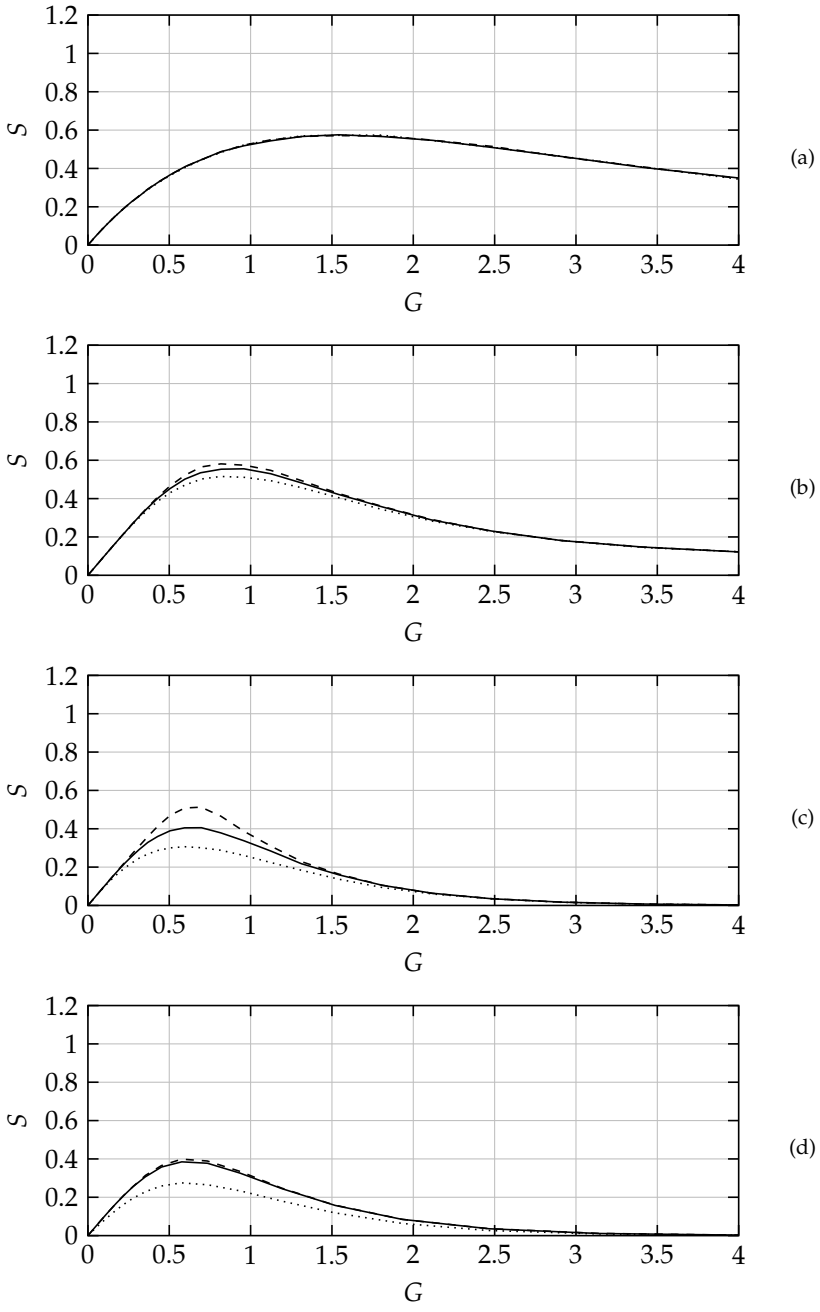

Figure 4.1: Throughput vs. input load at different iterations: (a) IDIC-1, (b) IDIC-2, (c) CRDSA-ideal SIC, (d) CRDSA-nonideal SIC. ····· $\iota_{\max} = 1$, —— $\iota_{\max} = 2$, - - - $\iota_{\max} = 10$.

conditions, namely, without using high-end components. Furthermore, the directional transmission-omnidirectional reception context is consistent with the modeled 5G uplink random access scenario, in which M contending users steer the main lobe of their radiation pattern towards the 5G BS that must be capable of simultaneously receiving all the transmitted bursts, subsequently beginning the processing of the RAF to establish which bursts have been captured and hence which replicas can be cancelled.

4.4 Numerical Results

Results are derived by averaging the simulations over $\mathcal{Q} = 100$ randomly generated network topologies.

4.4.1 Equivalence of simulation approaches

Before discussing the results, a justification in favor of the aforementioned approach, that is, the averaging over different topologies, will be given. The reason is twofold: on one side, for the sake of generality, the IDIC algorithm shall not be tested only on one topology; on the other, taking into consideration a large number of topologies may result in an excessively time consuming process. Therefore, the two following approaches are compared:

- a single Monte Carlo simulation in which the network topology is changed at every RAF, and
- a Monte Carlo simulation for every topology considered.

The purpose of this section is to provide evidence that these two different simulation approaches yield equivalent results. The benefit of this equivalence consists in the fact that a faster simulation can be carried out, without loss of representativeness for the given scenario.

To this aim, a paired Student's t-test is used. This test is generally used to indicate that data observed in a certain group under different circumstances are linked in some way. Specifically, if X is the observation of the first experiment and Y is the observation of the second one, the paired-sample t-test returns a test decision for the null hypothesis that the data in $X - Y$ comes from a normal distribution with mean equal to zero and unknown variance. So, for the purposes of the present assessment, the null hypothesis to be tested can be rephrased in the following terms: *the difference of the throughput values of the two samples is caused only by random effects*.

Therefore, the null hypothesis is expected to be accepted, instead of being rejected. That is: the difference of the throughput values is not caused by the variations of the network topology, but only by the different outcomes of the random experiments for the packet generation and the random placement of the bursts in the RAF, and the subsequent decoding. Should the null hypothesis be rejected, the conclusion would be that the difference would

Table 4.3: Results of the paired-sample Student's t-test to evaluate the equivalence between simulation with fixed and variable topology.

Number of load points	Null hypothesis rejected
45	no
5	yes

have been caused by the different spatial distribution of the sources, since it is the only deterministic variation that has been introduced in the simulations.

This is also heuristically explained by the fact that the performance of the network in the considered scenario shall not be dependent on the topology; otherwise, the random access method should be devised keeping in consideration the topology in the first place, which is something unrealistic, given the random nature of nodes distribution inside a given area.

To perform the Student's t-test, the following data groups have been generated:

1. a set of 100 simulations of the network, each one of them consisting of 50 load points, with the nodes' topology changing every RAF (the topology is chosen between 100 possible ones)

2. a set of 100 simulations of the network, each one of them consisting of 50 load points, with a persistent nodes' topology (that is: the topology does not change for the entire duration of the simulation, but changes amongst different simulations), each one of the topologies is different from the others, and is never used twice

The set of topologies has been generated in advance, and the code of the simulation recalls the topology values (namely, d_m and θ_m) from this set. The significance level used id $o = 0.05$ (that is, 5%). The results of the Student's t-test for the paired samples 1 and 2 are given in Table 4.3. The tests are carried out grouping together the results for the same load point, therefore 50 tests are performed.

As it can be seen in Table 4.3, the null hypothesis is to be rejected only in 5 cases out of 50; therefore the simplified approach can be considered trustworthy.

4.4.2 Impact of packet diversity

The first set of results shows the throughput S as a function of the input load $G = M\lambda$ [13, 20], for IDIC-1 (Figure 4.1(a)), IDIC-2 (Figure 4.1(b)), CRDSA with ideal (Figure 4.1(c)) and nonideal (Figure 4.1(d)) SIC. Both S and G are normalized to the slot duration, and each subfigure reports the curves for three values of the maximum number of iterations $\iota_{\max} \in \{1, 2, 10\}$. Each plotted curve is derived by averaging the simulations over $Q = 100$ randomly

generated users' topologies within the disk $\mathrm{D}(O, \rho)$. The figure is obtained considering the presence of the sole path-loss attenuation in LOS conditions.

A first comparison between Figures 4.1(a) and 4.1(b) and Figures 4.1(c) and 4.1(d) shows the performance improvement provided by the IDIC receiver with respect to the CRDSA-based solutions. This improvement involves not only S, but, also and significantly, the input load corresponding to the maximum throughput, which is approximately equal to 1.5 for IDIC-1 and to 0.9 for IDIC-2. Furthermore, unlike CRDSA, the IDIC approach ensures that the network is still operational even under heavy load conditions. In fact, while the throughput of CRDSA quickly degrades after its maximum, that of IDIC remains acceptable. According to [13], a direct view of Figures 4.1(c) and 4.1(d) confirms that an imperfect cancellation influences the CRDSA throughput, but does not have a significant impact on the input load corresponding to the maximum, which remains substantially unmodified in the two cases.

A focused comparison between IDIC-1 and IDIC-2, which adopt the same receiver operation, but differ in the number of transmitted copies, reveals two interesting aspects. Firstly, IDIC-1 and IDIC-2 achieve a really similar maximum throughput, but at different G values. This indicates that, when the receiver exploits the capture effect, notwithstanding the non-zero cancellation residual, sending two packet copies in each RAF (as in CRDSA), is useful for low channel loads. Conversely, sending a single packet copy in each RAF becomes advantageous for higher channel loads. Thus, packet diversity may be not always preferable, and the optimal strategy is hybrid. The second aspect that may be noticed is that, in all cases characterized by a non-ideal cancellation, thus also including CRDSA with imperfect SIC, few iterations ($\iota_{\max} = 1, 2$), are sufficient to achieve a throughput very close to the maximum one ($\iota_{\max} = 10$). This aspect, which provides significant benefits in terms of decoding delay, is taken to the extremes by IDIC-1, in which the curves corresponding to the three maximum iterations are almost superimposed. A further observation may be formulated by noticing that IDIC-2 outperforms CRDSA with ideal SIC, which reveals that the benefit of exploiting capture dominates over the penalty of having a cancellation residual.

We remark that the IDIC improvements are achieved without introducing any additional complexity at the receiver side with respect to CRDSA, since the capture effect is naturally present in any receiver, while the cancellation procedure is already required by CRDSA. A further specific advantage of IDIC is that of providing similar maximum throughput values regardless of the adoption or not of packet diversity. Hence, if a system designer wanted to select IDIC-1 for a 5G BS receiver, it may benefit of a significant advantage over repetition-based schemes, consisting in the easier adoption of IDIC-1 in legacy FSA systems, where the user's transmitter is programmed to send one burst copy per RAF. In fact, the introduction of CRDSA requires changing or reprogramming all sources to enable the transmission of burst copies, while IDIC-1 does not imply sources' modifications and may be hence immediately

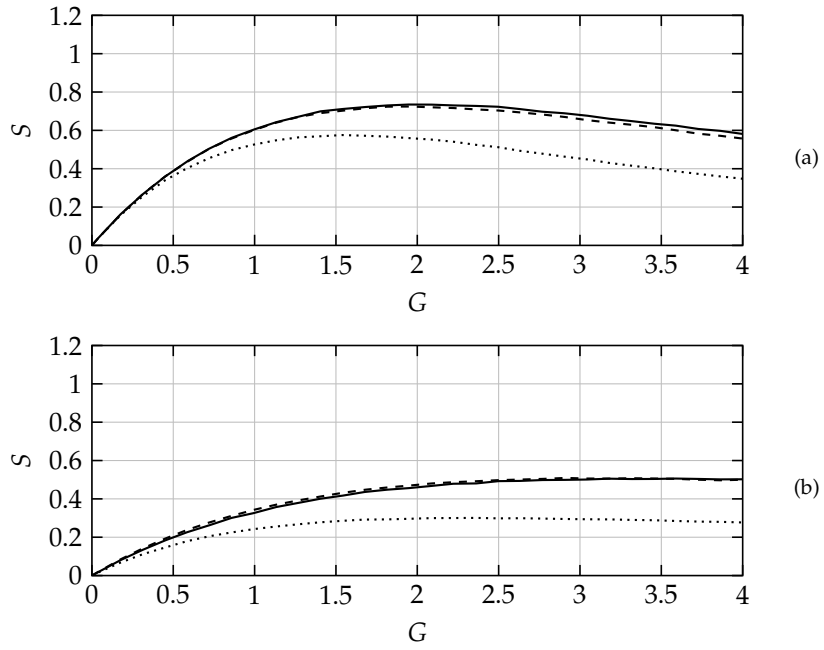

Figure 4.2: Throughput vs. input load for IDIC-1 with $\iota_{\max} = 10$ in different channel conditions: (a) LOS, (b) NLOS. ····· Path Loss - - - Path-loss and shadowing —— Path-loss, shadowing and fading.

implemented.

4.4.3 Impact of power diversity

The second set of results, obtained adopting $\iota_{\max} = 10$, shows the throughput as a function of the input load for IDIC-1 in LOS (Figure 4.2(a)) and NLOS (Figure 4.2(b)) conditions, and for IDIC-2 in LOS and slow (Figure 4.3(a)), NLOS and slow (Figure 4.3(b)), LOS and fast (Figure 4.3(c)), NLOS and fast (Figure 4.3(d)) fading conditions. Notice that, for IDIC-2, it is worth to distinguish between slow and fast (mid- and small-scale) fading scenarios. More precisely, in a slow fading scenario, the two copies of a burst are subject to the same shadowing and fading (when present) obtained by using the same realization of the corresponding r.v.. Instead, in a fast fading scenario, the two copies are subject to two independent realizations of each of the respective r.v.s.. Each of the six plots reports three curves, corresponding to the presence of sole path-loss attenuations, the presence of both path-loss and shadowing, and, finally, the presence of path-loss, shadowing, and fading.

The first observation that can be formulated from this second set of figures concerns the benefits generally introduced by any added form of power diversity. This result is also consistent with several studies developed for the conventional microwave channel [67]. In the here investigated mmWave context, the presence of shadowing considerably increases the throughput

with respect to the case of sole path-loss, while the additional presence of small-scale fading usually provides a further slight improvement. Hence, the IDIC scheme properly operates in the propagation context that characterizes the mmWave environment, since it is not damaged by the substantially unavoidable mid- and small-scale fading effects, but, according to the NOMA concept, constructively exploits them as further sources of power diversity. Notice that, in the IDIC-2 cases, this consideration holds also when slow and fast fading scenarios are compared, since the second one, being characterized by the generation of independent shadowing and fading for the two packet copies, introduces an additional power diversity effect among them that is not present in the slow fading scenario.

Concerning the usage of packet diversity, the optimality of the hybrid approach consisting in the adoption of IDIC-2 for low G values and of IDIC-1 for the higher G ones is confirmed by these results, which include all the main propagation phenomena that may be found in the mmWave channel. Interestingly, except for very high channel loads, the LOS scenario results always preferable than the NLOS one. This, intuitively, might seem an expected behaviour, but, on a closer inspection, suggests a deeper consideration. Since all the investigated LOS (NLOS) scenarios are homogeneous, in the sense that all users (SoI and interferers) experience the same LOS (NLOS) conditions, the higher throughput in the LOS cases reveals that having a SoI directly visible is preferable to having all the interferers partially obstructed. This behaviour confirms one of the differences between mmWave and microwave communications [68], where usually the reduction of the interference represents the main concern [63].

4.4.4 Impact of the SINR threshold

The final set of results, still obtained adopting $\iota_{\max} = 10$, shows the impact of the SINR threshold on the throughput for IDIC-1 in LOS (Figure 4.4(a)) and NLOS (Figure 4.4(b)) conditions, and for IDIC-2 in LOS and fast (Figure 4.4(c)), and NLOS and fast (Figure 4.4(d)) fading conditions. Each plot considers five thresholds $\xi \in \{0, 1, 3, 5, 10\}$ (dB) and is derived including all the modeled mmWave propagation phenomena: path-loss, shadowing, and fading.

These results confirm that the adoption of a lower SINR threshold provides a higher throughput, thanks to the increase of the capture probability due to the relaxation of the reception requirement. However, since the threshold is also related to the modulation and the coding rate of the channel encoder implemented at the PHY layer, it is not sure that a higher throughput efficiency directly implies a higher aggregate data rate. What instead may be reliably predicted is that, adopting a lower ξ value, a higher number of communications will become sustainable. Therefore, if the objective is to improve the fairness within the 5G cell, the usage of a low threshold may help to guarantee the connectivity to more users. The importance of the parameter

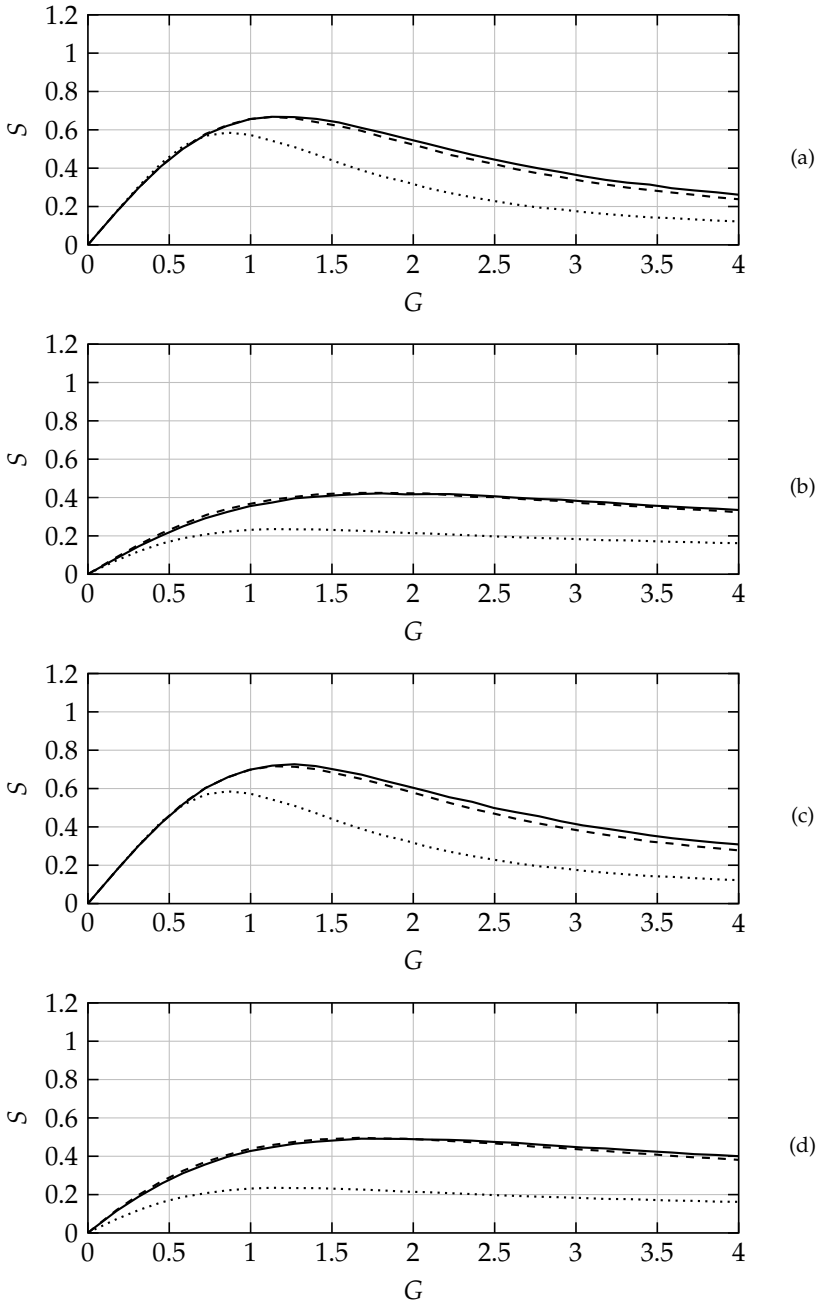

Figure 4.3: Throughput vs. input load for IDIC-2 with $\iota_{\max} = 10$ in different channel conditions: (a) LOS and slow fading scenario, (b) NLOS and slow fading scenario, (c) LOS and fast fading scenario, (d) NLOS and fast fading scenario. ····· Path Loss - - - Path-loss and shadowing —— Path-loss, shadowing and fading.

ξ in the mmWave context may be emphasized recalling the space limitations reserved to the antenna system on a user's device. These limitations may be assumed similar to those on a microwave device in terms of absolute dimensions, but, being the single mmWave radiating element much smaller, many antennas can be deployed on a 5G device in agreement with the massive MIMO paradigm. However, typically, no more than $K = 32$ elements are considered deployable on a Ka- or V-band transceiver [2]. This limits the maximum transmitting antenna power gain that can be reached to compensate the mmWave channel attenuations. To maintain an acceptable coverage within the 5G cell when these attenuations become consistent and no more compensated by the gains of the transmitting/receiving antennas, the basic element on which the system designer can still act is the SINR threshold ξ, namely, in practice, the code-modulation pair.

A final observation that may be formulated regarding Figure 4.4 concerns the appearing of some differences in the maximum throughput between IDIC-1 and IDIC-2 for the lower ξ values when LOS conditions are considered (Figure 4.4(a) and Figure 4.4(c)). This might represent a possible reason for preferring IDIC-1, which presents the higher maximum S values, and hence results more versatile in exploiting the code-modulation pair adopted at the PHY layer. This motivation may be considered beside the other previously discussed one, regarding the simpler implementation of IDIC-1, which, similarly to conventional FSA, does not require the introduction of packet diversity. However, in general, from the reported results referred to the mmWave domain, the preferable solution for the receiver of a 5G BS in an uplink contention-based context seems to remain an adaptive IDIC-r approach in which the number of burst copies r is selected according to the offered load G and the SINR threshold ξ.

4.5 Summary

In this chapter, IDIC-r, a novel receiver operation model for uplink random access at 5G BSs based on iterative decoding and interference cancellation has been introduced. It is capable of exploiting power and packet diversity through radio capture. The IDIC-r performance, properly obtained considering imperfect cancellation and realistic mmWave channel conditions adherent to recent measurements at 28 GHz, has shown improvements when compared to the widely adopted CRDSA scheme with ideal and noideal SIC. Beside the improved throughput, the specific IDIC-1 receiver, which operates in the presence of a unique burst copy and results more versatile in adapting to the physical layer components, yields the advantage of being backward compatible with legacy SIC-enabled FSA systems. In fact, since both FSA and IDIC-1 rely on one burst copy, no changes are needed at the transmitter side, while just interference cancellation capabilities, already assumed by CRDSA, are required at the receiver side.

The results have however put into evidence that, in general, the preferable

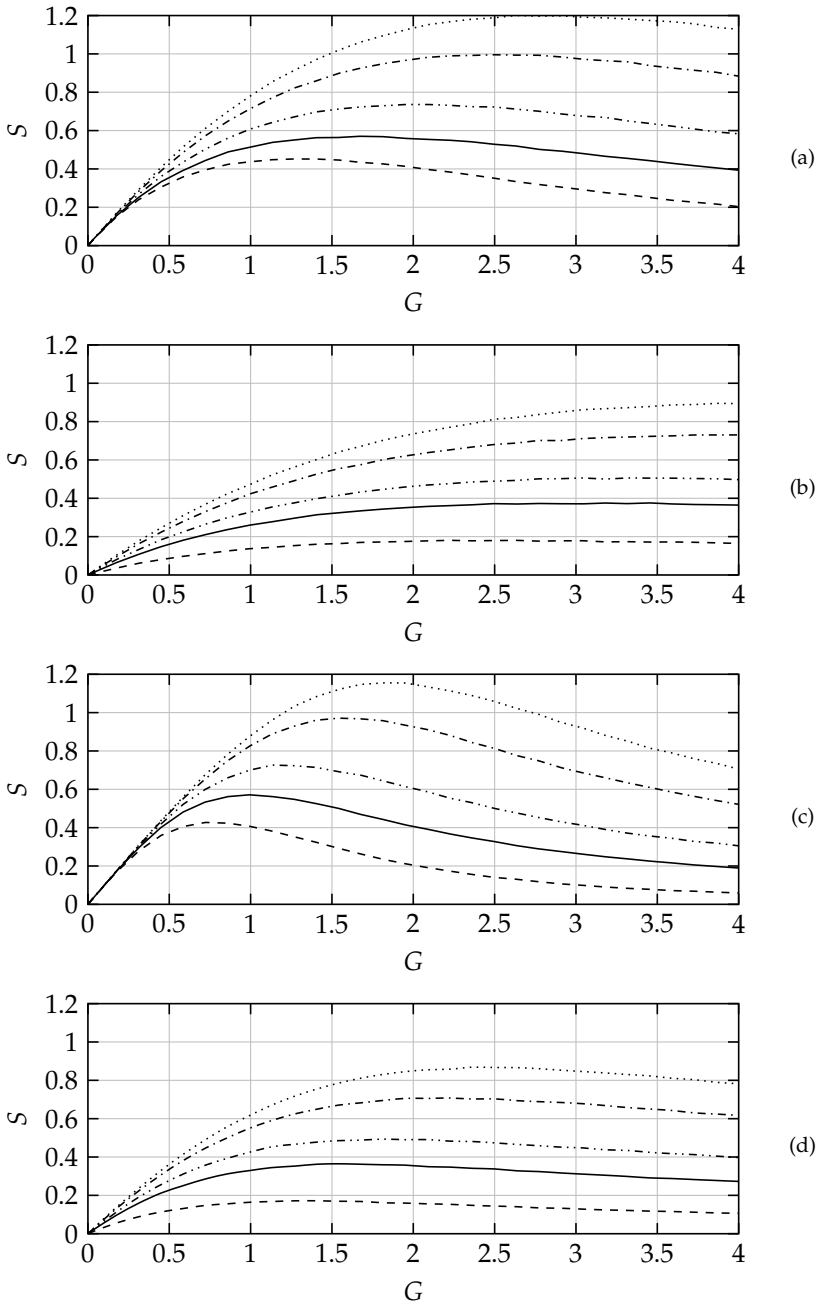

Figure 4.4: Throughput vs. input load in the presence of path-loss, shadowing, and fading for $\iota_{\max} = 10$ and different SINR thresholds: (a) IDIC-1 in LOS conditions, (b) IDIC-1 in NLOS conditions, (d) IDIC-2 in LOS and fast fading conditions, (b) IDIC-2 in NLOS and fast fading conditions. ····· $\xi = 0\,\mathrm{dB}$, -·-·- $\xi = 1\,\mathrm{dB}$, -·-· $\xi = 3\,\mathrm{dB}$, —— $\xi = 5\,\mathrm{dB}$, - - - $\xi = 10\,\mathrm{dB}$.

strategy in terms of packet diversity is to adapt the number of transmitted burst copies to the channel load and to the adopted code-modulation-pair, thus implementing a hybrid IDIC-1/IDIC-2 approach so as to maximize the throughput in each occurring scenario. From a conceptual point of view, the here proposed study suggests that the opportunity of sending multiple burst copies, as done by repetition-based schemes, may be tightly connected to the combined assumptions of perfect interference cancellation and equal receive power (i.e., no capture). An intuitive interpretation of this relation may be formulated in terms of distortion of the cost/benefit balance that is assumed when packet diversity is applied neglecting the SINR conditions. In fact, on one hand, the cost of the increased channel load due to the additional packet copies may be under-estimated by the assumption of very low power residual after cancellation. On the other hand, the benefit of transmitting additional copies to increase the probability of successful decoding may result amplified by the absence of capture. When these assumptions are relaxed, the traditional strategy of sending a single packet copy per frame may become again preferable in some scenarios, depending on the traffic that must be sustained in the 5G cell and on the PHY layer capabilities of the mmWave communicating devices.

Chapter 5

Phased Array Design for Extending CubeSat Operations to Ka-band

Started as educational tools, CubeSats have immediately encountered the favor of the scientific community, subsequently becoming viable platforms for commercial applications. To enable this second usage, the operative frequencies had to shift from amateur radio bands towards commercial bands, so as to ensure competitive data transfer rates. This has led some pioneers to explore the adoption of the Ka-frequencies for small satellite missions, thus establishing novel challenging objectives to antenna designers. To address this issue, this study proposes a phased-array design for CubeSat downlink operations in the Ka-band. The conceived array structure provides 1.5 GHz bandwidth at 37 GHz and consists of 64 circularly polarized subarrays of microstrip patches arranged on an 8×8 square grid filling one face of a single CubeSat unit. The array excitations are synthesized by a low-complexity phase-only control algorithm based on the method of successive projections, with the aim to provide circular polarization and reconfigurability remaining adherent to the cost-effective CubeSat paradigm[1].

5.1 Introduction

As presented in Chapters 1 and 3, a growing number of small satellites has populated the LEO, specifically involving a recently developed class of spacecrafts: the CubeSats [69]. From a technological point of view, the initial constraints faced by small satellite designers were mainly related to power availability and aperture requirements for supporting environmental monitoring missions [70]. For these activities, the bands assigned to the amateur radio service were considered sufficient to support the radio communications. This allocation method remained however satisfactory as long as the objectives

[1]This chapter is based on G. Buttazzoni, M. Comisso, A. Cuttin, M. Fragiacomo, R. Vescovo, and R. Vincenti Gatti, "Reconfigurable phased antenna array for extending cubesat operations to Ka-band: Design and feasibility", *Acta Astronautica*, vol. 137, pp. 114–121, 2017, ISSN: 00945765.

of the missions were educational. In fact, the improved sensor resolution, and the entrance of military and commercial subjects, have determined the need of larger transfer rates to support the increased amount of flowing data. Hence, at present, the throughput demand is fostering the spacecraft systems' developers to explore higher practical transmission frequencies, thus moving towards the mmWave bands, which may guarantee higher reuse factors and larger bandwidth [70]. In addition, radio transceivers satisfying CubeSat power/size constraints and providing rates in the order of hundred of megabits are nowadays available on the market [71]. The exploitation of these opportunities is unfortunately restrained by the propagation characteristics of mmWaves, which are subject to strong attenuation and noise. The compensation of these phenomena requires the adoption of high-gain circularly polarized antennas in combination with reliable Attitude Determination and Control Subsystems (ADCSs) for regulating the orientation of the spacecraft. However, while this second issue is not a prohibitive concern, since high-accuracy, 3-axis stabilized ADCSs for small satellites currently exist [70], the design of high-performance mmWave antenna systems for CubeSats remains a hot topic.

In this context, some proposals have been formulated. The Jet Propulsion Laboratory has recently developed an attractive high-gain Ka-band parabolic antenna, realized adopting 30 ribs stowed within a space of 1.5U that unfold to deploy the antenna in a Cassegrain configuration [72]. In [73], a conical horn has been embedded onto the 1U envelope of the transmitter. A cutting-edge reflectarray antenna operating at 26 GHz and printed on the back of three deployable solar panels has been designed within the ISARA mission, sponsored by the NASA Small Satellite Technology Program [39].

Beside these projects under development, further interesting solutions may derive from antenna array technology, which has however received less consideration, even if, nowadays, reflectors and arrays compete in many types of systems [57]. Several motivations invite to essay this possibility: compactness, no aperture blockages, and avoidance of deployment phases, since an array of microstrip patches may be directly embedded on a CubeSat face. Flexibility can also be guaranteed by implementing a suitable beamforming algorithm able account for multiple requirements, including high-gain and CP: two features that are in practice mandatory to limit the strong signal attenuation and the polarization mismatch. Other functionalities, such as phase-only control and pattern reconfigurability, may be introduced to simplify the actual realization of the feeding network and to support possible multi-task missions. Forthcoming missions, in fact, will not be limited to conventional LEO orbiting, requiring high-gain narrow-beam antenna patterns, but are also expected to involve constellations of CubeSats [74, 75], requiring patterns with wider main lobes to enable the identification of other nearby CubeSats for intersatellite communication purposes.

In light of these considerations, this chapter presents the design of a Ka-band phased antenna array providing CP and pattern reconfigurability to

support downlink and intersatellite CubeSat missions. Preliminary experimental and numerical results combined with illustrative link budgets are also reported to discuss the applicability of the array technology to next generation Ka-band CubeSats.

5.2 Array structure

Since the design of spacecraft subsystems is strictly dependent on the mission objectives, a broadside configuration, which can be suitably adapted to different tasks, is considered as a baseline for the development of the array structure,. With this choice, in this section, the array structure is designed first, by accounting for the operational frequency and the size constraints, while, in Section 5.3, the required radiation patterns by accounting for the mission purposes is synthesized.

The array structure consists of a planar array that fits to one face of a 1U CubeSat [77], so as to make the proposed antenna system suitable for missions adopting any of the allowed form factors from 1U up to 27U. A mechanical prototype built at PicoSaTs s.r.l. [76], displays the face chosen to accommodate the array (Figure 5.1), which consists of N subarrays, each formed by four microstrip patches. The design of the subarray with the corresponding parameters is reported in Figure 5.2(a,b). The single patch, realized to operate in the Ka-band at the frequency of 37 GHz, corresponding to a wavelength $\lambda_0 = 8.108$ mm, is developed using the mitering method [78], to obtain Right Hand CP (RHCP) [79]. The geometry selected to obtain the circularly polarized patch antenna consists of a square patch of side d with mitered corners (two opposite corners are truncated in the shape of an isosceles triangle with the shortest side of length m). This specific shape is selected because it has only two parameters to deal with (lengths d and m) and it is believed to be the easiest to manufacture. For manufacturing reasons and to reduce the coupling effects with the feeding line due to the high operational frequency, a three-layer design is considered, with two DiClad 880 substrates and a mid prepreg I-TERA MT solding substrate. To better match the RHCP constraint, minimize Left Hand CP (LHCP), and to increase the bandwidth, the subarray building block is developed using the sequential phase-rotation technique by sequentially arranging the four patches in orientation and phase at 0°, 90°, 180°, and 270° [80, 81].

With such a system, not only is the feed complexity reduced[2], but also the bandwidth performance is improved. This is because most of the radiation impurity (due to higher order modes generating in the substrate) from the 0° element cancel out with that from the 180° element, and likewise for the 90° and 270° elements. While this holds true for the principal planes, it is not the same for other plane cuts (like $\phi = 45°$), where higher levels of cross polarization should be expected (basically because of the lack of simmetry). This

[2]In a conventional array, four feeds might be needed for each sub-array, while in this case only one is requested.

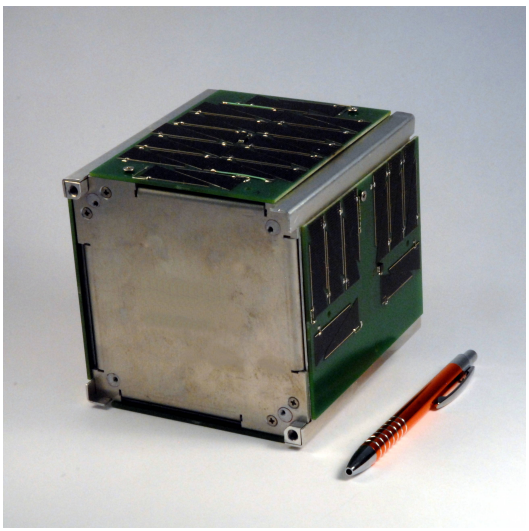

Figure 5.1: Mechanical mock-up of a 1U CubeSat: the exposed face of the frame (i.e., the one without solar panels) is selected to accommodate the developed antenna array. Picture courtesy of PicoSaTs s.r.l. [76].

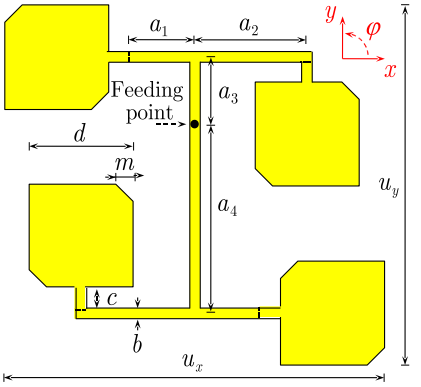

Parameter	Value [mm]
d	2.512
m	0.675
c	0.500
b	0.250
a_1	1.500
a_2	2.904
a_3	1.516
a_4	4.324
u_x	9.024
u_y	8.352

(a)

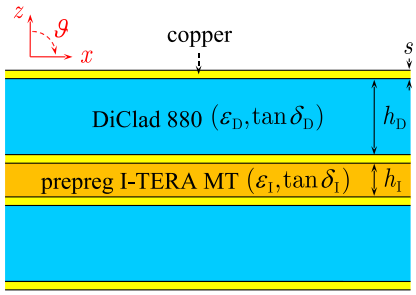

Parameter	Value
s	0.035 mm
h_D	0.254 mm
ε_D	2.20
tanδ_D	0.0009
h_I	0.065 mm
ε_I	3.45
tanδ_I	0.0031

(b)

Figure 5.2: Subarray building block: (a) front-view design, (b) side-view design.

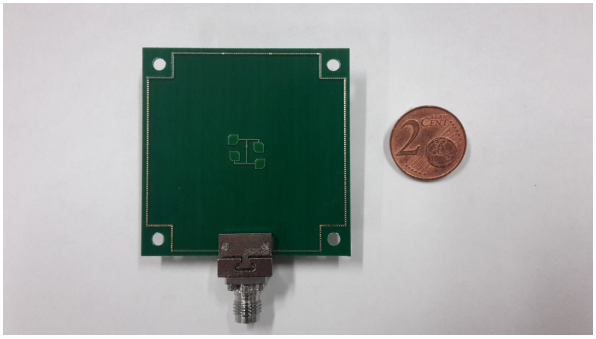

Figure 5.3: Subarray building block: fabricated prototype.

can be overcome in a larger array, where the amplitude and phase imbalances average each other out. Another advantage achieved thanks to this configuration is that the mutual coupling effect is significantly reduced from that of a conventional array. Since an element is orthogonally oriented respect to the other neighboring four, the coupling is very small [50].

The sequential phases are achieved by quarter-wavelength delay lines and optimizing the feeding network by CST Microwave Studio to minimize the losses. In particular, the lengths $a_1, \ldots, a_4$ in Figure 5.2(a) are evaluated to ensure that the relationships

$$a_2 + a_4 - \frac{\lambda_g}{4} = a_1 + a_4 = a_2 + a_3 + \frac{\lambda_g}{4} = a_1 + a_3 + \frac{\lambda_g}{2} \tag{5.1}$$

be satisfied for the guided wavelength $\lambda_g = 5.616\,\text{mm}$.

The simulated and experimental performance obtained from a fabricated prototype (Figure 5.3), shows that the subarray provides a 10 dB-bandwidth larger than 1.5 GHz (Figure 5.4(a)), thus matching the high-bandwidth requirement, and a maximum gain of 11.54 dB with an RHCP/LHCP isolation of 12.51 dB (Figures 5.4(b) and 5.4(c)). A satisfactory level of polarization purity is also obtained, since both the simulated and measured Axial Ratio (AR) remain within 3 dB in the mainlobe. Except for few discrepancies in the $\varphi = -90^\circ$ half-plane (Figure 5.4(c)) due to a partially unshielded cable connector on the back of the prototype, a good agreement between simulations and measurements may be observed.

For the design of the full array, the surface that can be actually occupied at the net of the mandatory CubeSat rails [69], is a square of edge $R = 85\,\text{mm}$. Since the maximum size of a subarray is $u_x = 9.024\,\text{mm}$ (Figure 5.2(a)), an array of $N = 8 \times 8 = 64$ elements may be fitted on the available surface by selecting a distance $r = 10.625\,\text{mm}$ between the feeding points of two adjacent subarrays, in order to maintain a distance of at least $\lambda_0/5$ between their sides (Figure 5.5). To account for the mutual coupling due to the closeness between the elements, the ϑ-(zenith) and φ-(azimuth) components $E_n^\vartheta(\Omega)$ and $E_n^\varphi(\Omega)$ of the electric far-field of the n-th subarray ($n = 1, \ldots, N$) in the direction $\Omega = (\vartheta, \varphi)$ are calculated accounting for the presence of the other

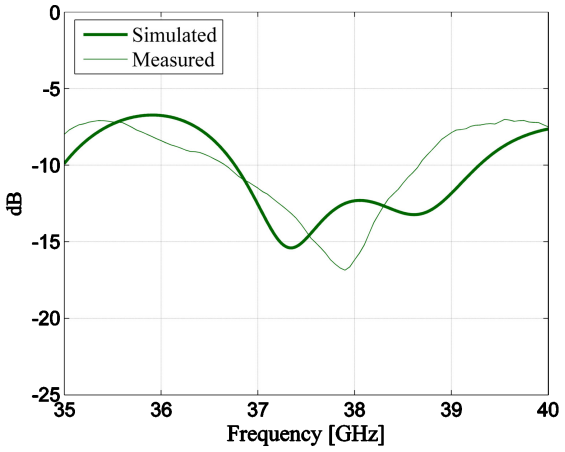

(a)

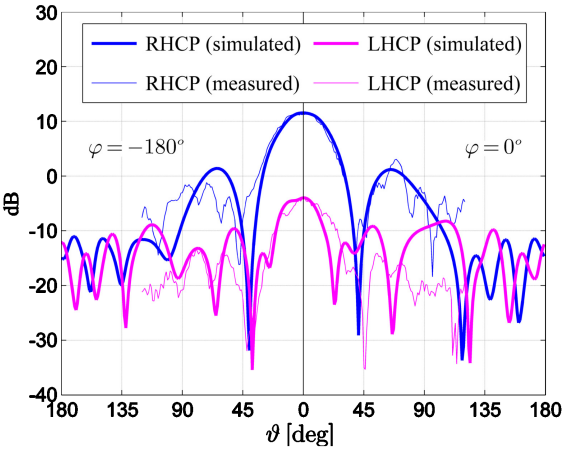

(b)

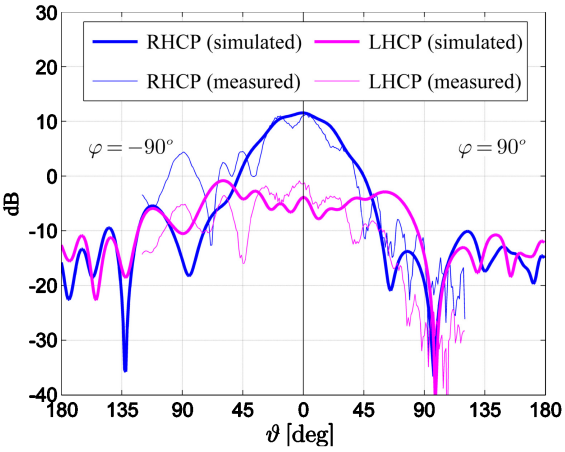

(c)

Figure 5.4: Subarray performance: (a) return loss, (b) 2D gain pattern cuts in the $x-z$ plane, (c) 2D gain pattern cuts in the $y-z$ plane.

adjacent subarrays by using the method in [82]. This method exploits the linear relationship between the array and the element patterns to estimate $E_n^{\vartheta}(\Omega)$ and $E_n^{\varphi}(\Omega)$ by a suitable electromagnetic software (in our case CST Microwave Studio) using a unity-voltage zero-phase feed for the n-th element and a zero-voltage feed for the remaining $N-1$ elements. Besides, to obtain a compact formulation, $E_n^{\vartheta}(\Omega)$ and $E_n^{\varphi}(\Omega)$ include also the phase shift due to the position inside the array. Hence, denoting as j the imaginary unit and as $\boldsymbol{\alpha} = [\alpha_1, \ldots, \alpha_N]$ the vector of the complex excitations of the array elements, the RHCP component $E_1(\boldsymbol{\alpha}; \Omega)$ and the LHCP component $E_2(\boldsymbol{\alpha}; \Omega)$ are jointly expressed, for $i = 1, 2$, as:

$$E_i(\boldsymbol{\alpha}; \Omega) = \frac{1}{\sqrt{2}} \sum_{n=1}^{N} \alpha_n \left[E_n^{\vartheta}(\Omega) - j(-1)^i E_n^{\varphi}(\Omega) \right], \tag{5.2}$$

which analytically describes the RHCP/LHCP patterns provided by the array structure for a given excitation vector $\boldsymbol{\alpha}$.

5.3 Pattern synthesis

Once the array structure is designed, the excitations of the N subarrays are synthesized to generate two different patterns for supporting a dual-task mission. Next-generation CubeSats are in fact expected to perform not only LEO orbiting, but also internetworking operations, where constellations of small satellites exchange scientific or commercial data. Accordingly, a task $t = 1$ consists in communicating with the ground station by a pattern with a narrow, high-gain beam. A task $t = 2$ consists in realizing an intersatellite link, which takes advantage of a pattern with a broader beam and a lower gain to properly search the neighboring CubeSats. The aim is to satisfy the generic task t by simply orienting the CubeSat face containing the array towards the appropriate region of space (i.e., towards the ground station for $t = 1$, or towards the satellites' constellation for $t = 2$) by means of the on-board ADCSs, and then selecting the proper excitation vector $\boldsymbol{\alpha}_t = [\alpha_{1,t}, \ldots, \alpha_{N,t}]$. Thus, two sets of excitations, $\boldsymbol{\alpha}_1$ and $\boldsymbol{\alpha}_2$, must be synthesized to enable the reconfigurability of the pattern according to the selected task. For each task, the LHCP field represents the undesired radiation, so its amplitude is kept below a given threshold ζ_t. Furthermore, the amplitude $|\alpha_{n,t}|$ and the phase $\arg(\alpha_{n,t})$ of the n-th element during the task t are properly constrained to reduce the complexity of the feeding network. More precisely, $|\alpha_{n,t}|$ is forced to belong to the set $\{0, 1\}$ (on/off condition), thus, all the actually active elements have an identical amplitude, and the synthesis is hence carried out by phase-only control.

In summary, the formulated dual-task problem consists in finding, for

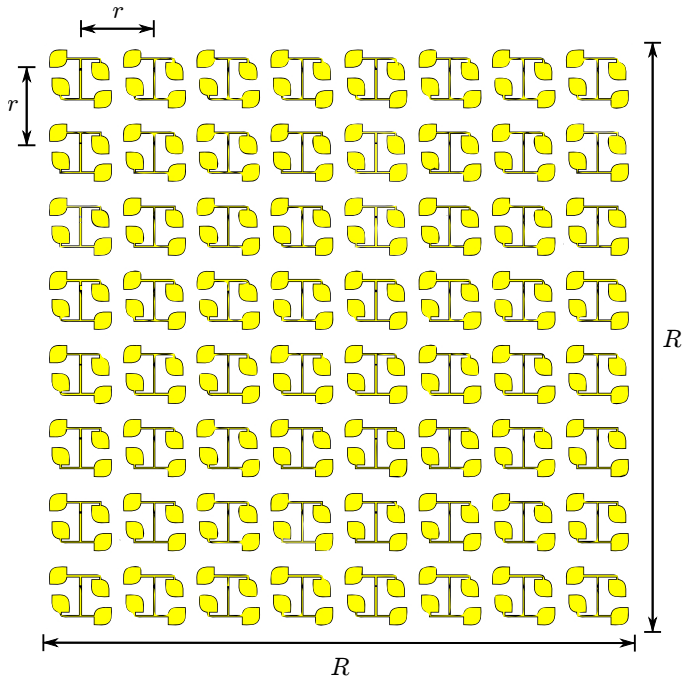

Figure 5.5: Array structure: front view.

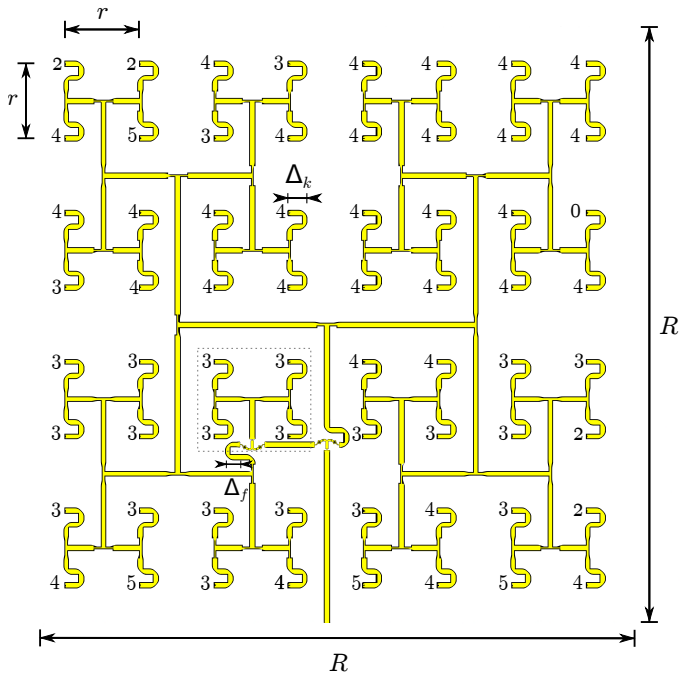

Figure 5.6: Array structure: back view (feeding network).

each $t = 1, 2$ value, an excitation vector $\boldsymbol{\alpha}_t$ satisfying the constraints:

$$|E_1(\boldsymbol{\alpha}_t; \Omega)| \in M^t, \tag{5.3a}$$
$$|E_2(\boldsymbol{\alpha}_t; \Omega)| \leq \zeta_t, \tag{5.3b}$$
$$|\alpha_{n,t}| \in \{0, 1\},\ n = 1, \ldots, N, \tag{5.3c}$$

where M^t is the RHCP pattern mask that imposes the desired maximum gain $\mathcal{G}_t$, side-lobe level (SLL) ρ_t, and Half-Power BeamWidth (HPBW) ω_t for the task t. In particular, the imposed values are $\mathcal{G}_1 = 25\,\text{dB}$, $\rho_1 = \zeta_1 = 15$ dB, $\omega_1 = 4^\circ$, (task 1, narrow beam and high gain), $\mathcal{G}_2 = 15$ dB, $\rho_2 = \zeta_2 = 5$ dB, $\omega_2 = 20^\circ$ (task 2, wider beam and lower gain). This problem is solved by first identifying two sets: a set U, whose elements satisfy conditions (5.3a)-(5.3c), and a set V, whose elements account for the array structure by (5.2). Then, the algorithm in [83] is applied to perform an iterative sequence of alternate projections onto U and V to find the $\boldsymbol{\alpha}_1$ and $\boldsymbol{\alpha}_2$ vectors that minimize the distance between the two sets. The synthesized excitation phases are realized by the feeding network in Figure 5.6. The integer k near each subarray feeding point identifies the derived phase shift $\chi_k = k\pi/8$ (quantized to a multiple of $\pi/8$ to simplify the actual realization), which has been implemented by a stripline of length $\Delta_k = \chi_k/(2\beta_\text{g}) = k\lambda_\text{g}/32$, being $\beta_\text{g} = 2\pi/\lambda_\text{g}$ the wave number referred to the guided wavelength. Two switches are also inserted to enable pattern reconfigurability, since all elements are active for $t = 1$, while just the four ones inside the dashed square are active for $t = 2$. To maintain the phasing of the feeding network for $t = 1$, the second switch is provided with a properly designed delay line of length Δ_f.

Figure 5.7 reports the simulated performance of the full structure (array and feeding network). In particular, Figure 5.7(a) shows that the reconfigurable array maintains a satisfactory return loss, providing, for $t = 1$ (Figure 5.7(b)), a maximum gain of 24.04 dB, an HPBW of 4°, an LHCP/RHCP isolation of 13.47 dB, an AR of 3.75 dB, and, for $t = 2$ (Figure 5.7(c)), a maximum gain of 13.28 dB, an HPBW of 20°, an LHCP/RHCP isolation of 13.33 dB, an AR of 3.80 dB. Thus, it guarantees, beside the gain, a satisfactory polarization purity also for the second task, characterized by a wider main-lobe. These results confirm that a reconfigurable antenna array embedded on a CubeSat face may be able to satisfy the pattern requirements of forthcoming dual-task missions.

5.4 Feasibility aspects

To get a clearer view of the actual applicability of the designed reconfigurable Ka-band array in CubeSat scenarios, some specific implementation aspects relative to the link budgets and the competing reflectarray technology deserve to be investigated in more detail.

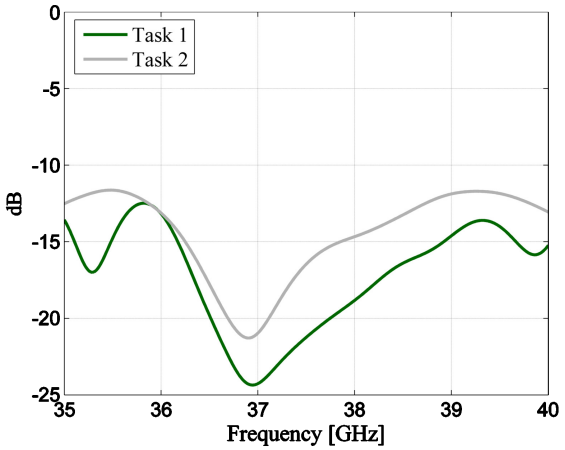

(a)

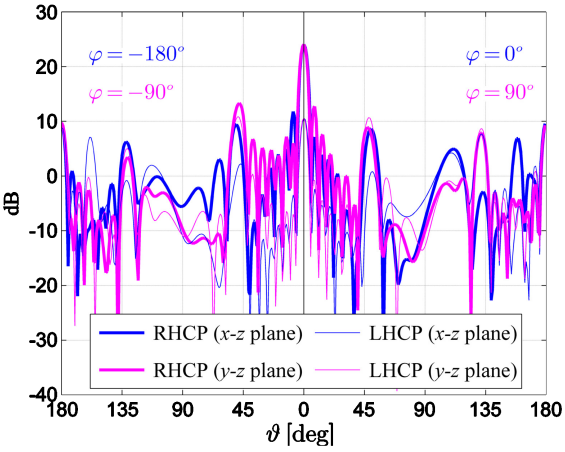

(b)

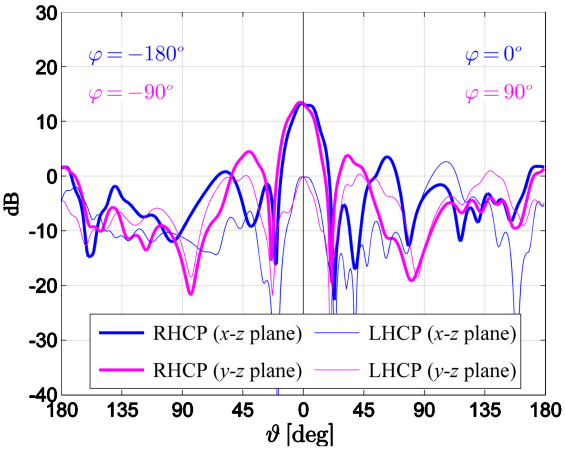

(c)

Figure 5.7: Reconfigurable array performance: (a) return loss, (b) 2D gain pattern cuts for task 1, (c) 2D gain pattern cuts for task 2.

5.4.1 Link budgets

The discussion moves from two illustrative link budgets, which are developed for the two considered tasks: the CubeSat-ground station downlink (Table 5.1) and the intersatellite communication (Table 5.2). Even though the two tasks have some common parameters and the corresponding budgets may look similar at a first glance, they exhibit significant differences when it comes to the evaluation of the propagation losses and receivers' features.

Once the input power and the transmitting antenna parameter (that is, the gain in the presence of the feeding network, the HPBW, and the polarization losses), are established for each task, a detailed link budget at the spacecraft side has to account for the pointing accuracy. Since the antenna is conceived to fit on a face of the spacecraft, its pointing is expected to be provided by the ADCS. Commercially available ADCSs typically provide a pointing accuracy of 0.5° or better [84], thus the impact of the pointing losses on the Effective Isotropic Radiated Power (EIRP) is limited for both tasks.

The propagation path is the major responsible for the losses, which shall be compensated by the transmitting and receiving subsystems. Whereas, in the intersatellite link, it is safe to assume that the overall path losses are given mainly by the Free Space Path Loss (FSPL), this is not the case for the downlink from space to Earth, where additional attenuations come into play because of the presence of the Earth's atmosphere. Moreover, given the LEO, the performance of the link during the access is not uniform, because the slant range between the ground station and the spacecraft varies from 400 km at the zenith to over 2000 km at the horizon, therefore yielding a significant variation of the FSPL during the in-view period. To take this into account, the budget for task 1 presents as a reference the average value of the FSPL corresponding to the average distance, meaning that the margin will improve when the satellite approaches the zenith, and will worsen when the satellite is closest to the horizon. Also, it may be noticed that the additional atmospheric attenuations in Table 5.1 relative to rain and clouds hold in pessimistic faded scenarios, while, in clear sky conditions, these attenuations are considerably reduced, thus increasing the available margin.

At the receiving end, in the task 1, the antenna is considered to be a parabolic reflector with a 70 % efficiency and a pointing accuracy of 0.1° [85], while, in the task 2, it is considered as an antenna system identical to the transmitting one. Distinct environmental conditions, referred to the Earth surface (task 1) and to the exosphere (task 2), are experienced by the two receiver sides, thus considerably differentiating the corresponding system noise temperatures even in the presence of an identical receiver. For both tasks, the selected receiver exploits one of the novel MODulation-CODe (MODCOD) configurations offered by the recently released Digital Video Broadcasting (DVB)-S2X extension [86]. This amendment extends the SNR working conditions with respect to the original DVB-S2 standard, until -10 dB, thus allowing the connectivity in the presence of significant atmospheric absorptions, which may sometimes arise during Ka-band communications. In par-

ticular, the receiver sides of the developed link budgets rely on the newly available configuration consisting of a quadrature phase-shift keying modulation in combination with a low density parity check/Bose Chaudhuri Hocquenghem joint encoder of rate 2/9, which ensures a reliable communication at 100 Mbps [87]. This choice, considered in conjunction with the available SNR resulting from the designed antenna system, leaves a satisfactory link margin for both tasks. To this purpose, it should also be noted that the selected communication protocol supports the adaptive coding and modulation, thus potentially allowing the full exploitation of the excess link margin by activating higher throughput MODCODs that require higher $(E_b/N_0)^r$ values. From a technological point of view, the premises to adopt a Ka-band communication link with the DVB-S2X standard are already in place. One proposal for a Ka-band CubeSat transceiver is presented in [88], and consists in mixing an intermediate-frequency signal at 1 GHz with the second harmonic generated by a local oscillator operating at half of the desired radio-frequency. Exploiting this approach, the presence on the market of components operating at frequencies beyond 15 GHz enables the achievement of frequencies above 30 GHz [89]. A second proposal, offering a range of operating frequencies between 17 and 40 GHz, relies on a software defined radio platform [90], thus allowing the upgrade to the advanced MODCODs specified in the DVB-S2X standard. In this context, an antenna array seems hence perfectly suited for enabling the support of dual-task missions in next generation Ka-band nanosatellites.

5.5 Summary

A reconfigurable antenna array for Ka-band CubeSats has been presented. The proposed structure provides interesting benefits in terms of bandwidth, polarization purity, and versatility, which suggest promising possibilities for the array technology in forthcoming Ka-band nanosatellites. The obtained encouraging results may be strengthened observing that the elements put beside the designed antenna system and adopted to develop the link budgets for a dual-task mission are not high-end components. Hence, low-cost arrays may certainly cooperate with the currently available off-the-shelf devices, thus maintaining the cost-effective requirement of the CubeSat communication system.

Further in-depth analyses might be inferred after the investigation of the impact of the manufacturing tolerances on a physical device, whose realization may be however trustfully carried out on the basis on the here discussed feasibility study and of the fabricated subarray prototype. In conclusion, the flexibility of arrays in providing advanced functionalities combined with the recent innovations in the other related CubeSat technologies, such as ADCSs and miniaturized Ka-band transponders, may represent a really inviting opportunity to accomplish multi-task missions at reasonable costs and reduced deployment risks.

Table 5.1: Link budget for task 1 (CubeSat-ground station downlink).

Spacecraft and transmitting (designed) antenna	
Input power: P	0.00 dBW
Line losses: L^{l}	0.10 dB
Maximum antenna gain: $G_{t,1}$	24.04 dB
Antenna HPBW: $\Omega_{t,1}$	4.00°
Antenna polarization losses: $L^{x}_{t,1}$ [91]	0.19 dB
Pointing accuracy: e_t [84]	0.50°
Pointing losses: $L^{p}_{t,1} = 12(e_t/\Omega_{t,1})^2$ [92]	0.19 dB
Antenna effective gain: $G^{e}_{t,1} = G_{t,1} - L^{x}_{t,1} - L^{p}_{t,1}$	23.66 dB
$\text{EIRP}_1 = P - L^{l} + G^{e}_{t,1}$	23.56 dBW
Downlink path	
Average distance: D_1	1200.00 km
$\text{FSPL}_1 = 20\log_{10}(4\pi D_1/\lambda_0)$ [93]	185.40 dB
Atmospheric gases attenuation: L^{g} [93]	5.00 dB
Rain attenuation: L^{w} [93]	2.00 dB
Cloud attenuation: L^{c} [93]	2.00 dB
Scintillation: L^{k} [93]	2.00 dB
Total path attenuation: $L^{a}_1 = \text{FSPL}_1 + L^{g} + \sqrt{L^{w} + L^{c} + L^{k^2}}$ [93]	193.22 dB
Ground station and receiving reflector antenna	
Antenna diameter: ξ	1.00 m
Antenna efficiency: η	0.70
Maximum antenna gain: $G_{r,1} = 10\log_{10}[\eta(\pi\xi/\lambda_0)^2]$ [92]	50.22 dB
Antenna HPBW: $\Omega_{r,1} = 70\lambda_0/\xi$ [92]	0.57°
Antenna polarization losses: $L^{x}_{r,1}$ [91]	0.35 dB
Antenna pointing accuracy: $e_{r,1}$ [85]	0.10°
Pointing losses: $L^{p}_{r,1} = 12(e_{r,1}/\Omega_{r,1})^2$ [92]	0.37 dB
Antenna effective gain: $G^{e}_{r,1} = G_{r,1} - L^{x}_{r,1} - L^{p}_{r,1}$	49.50 dB
System noise temperature: $T_{s,1}$	381.58 K
Required data rate: ϱ [87]	100.00 Mbps
Required signal-to-noise ratio per bit: $(E_b/N_0)^{r}$ [87]	-2.85 dB
Available signal-to-noise ratio per bit:	
$(E_b/N_0)^{a}_1 = \text{EIRP}_1 - L^{a}_1 + G^{e}_{r,1} + 228.60 - 10\log_{10} T_{s,1} - 10\log_{10}\varrho$	2.62 dB
Implementation losses: L^{i} [87]	1.35 dB
System Margin: $\text{SM}_1 = (E_b/N_0)^{a}_1 - (E_b/N_0)^{r} - L^{i}$	4.12 dB

Table 5.2: Link budget for task 2 (intersatellite communication).

Spacecraft and transmitting (designed) antenna	
Input power: P	0.00 dBW
Line losses: L^{l}	0.10 dB
Maximum antenna gain: $G_{\mathrm{t},2}$	13.28 dB
Antenna HPBW: $\Omega_{\mathrm{t},2}$	20.00°
Antenna polarization losses: $L^{\mathrm{x}}_{\mathrm{t},2}$ [91]	0.20 dB
Pointing accuracy: e_{t} [84]	0.50°
Pointing losses: $L^{\mathrm{p}}_{\mathrm{t},2} = 12(e_{\mathrm{t}}/\Omega_{\mathrm{t},2})^2$ [92]	0.01 dB
Antenna effective gain: $G^{\mathrm{e}}_{\mathrm{t},2} = G_{\mathrm{t},2} - L^{\mathrm{x}}_{\mathrm{t},2} - L^{\mathrm{p}}_{\mathrm{t},2}$	13.07 dB
$\mathrm{EIRP}_2 = P - L^{\mathrm{l}} + G^{\mathrm{e}}_{\mathrm{t},2}$	12.97 dBW
Intersatellite path	
Average distance: D_2	15.00 km
$\mathrm{FSPL}_2 = 20\log_{10}(4\pi D_2/\lambda_0)$ [93]	147.33 dB
Total path attenuation: $L^{\mathrm{a}}_2 = \mathrm{FSPL}_2$	147.33 dB
Spacecraft and receiving (designed) antenna	
Maximum antenna gain: $G_{\mathrm{r},2}$	13.28 dB
Antenna HPBW: $\Omega_{\mathrm{r},2}$	20.00°
Antenna polarization losses: $L^{\mathrm{x}}_{\mathrm{r},2}$ [91]	0.20 dB
Pointing accuracy: $e_{\mathrm{r},2}$ [84]	0.50°
Pointing losses: $L^{\mathrm{p}}_{\mathrm{r},2} = 12(e_{\mathrm{r},2}/\Omega_{\mathrm{r},2})^2$ [92]	0.01 dB
Antenna effective gain: $G^{\mathrm{e}}_{\mathrm{r},2} = G_{\mathrm{r},2} - L^{\mathrm{x}}_{\mathrm{r},2} - L^{\mathrm{p}}_{\mathrm{r},2}$	13.07 dB
System noise temperature: $T_{\mathrm{s},2}$	109.98 K
Required data rate: ϱ [87]	100.00 Mbps
Required signal-to-noise ratio per bit: $(E_{\mathrm{b}}/N_0)^{\mathrm{r}}$ [87]	-2.85 dB
Available signal-to-noise ratio per bit:	
$(E_{\mathrm{b}}/N_0)^{\mathrm{a}}_2 = \mathrm{EIRP}_2 - L^{\mathrm{a}}_2 + G^{\mathrm{e}}_{\mathrm{r},2} + 228.60 - 10\log_{10} T_{\mathrm{s},2} - 10\log_{10}\varrho$	6.90 dB
Implementation losses: L^{i} [87]	1.35 dB
System Margin: $\mathrm{SM}_2 = (E_{\mathrm{b}}/N_0)^{\mathrm{a}}_2 - (E_{\mathrm{b}}/N_0)^{\mathrm{r}} - L^{\mathrm{i}}$	8.40 dB

Chapter 6

Nanosatellite–5G networks integration in the millimeter wave domain

This chapter presents the contribution to the proposal of a novel network architecture for a hybrid nanosatellite (nSAT)-5G system operating in the millimeter-wave (mmWave) domain. The architecture is realized adopting a DTN approach, but allowing end users to use standard devices without any software or hardware modifications. A buffer aware contact graph routing algorithm is designed to account for the buffer occupancy of the nSATs and for the possibility of planning the connections according to the visibility periods of the satellites. At the terrestrial uplink, the DTN architecture is combined with a coded random access to enable a high-capacity interface for the typically irregular traffic of the 5G users, while, at the satellite uplink, the contention resolution diversity slotted Aloha protocol is implemented to match the recent update of the DVB-RCS2 standard. To achieve a reliable testing of the functionalities introduced at the upper layers, an accurate analysis of the statistic of the signal to interference-plus-noise ratio and of the capture effect at each mmWave link is carried out by accounting for the impact of interference, shadowing, fading, and noise. An application of the designed mmWave nSAT-5G system is finally proposed, together with an estimation of the corresponding performance, which is evaluated by a discrete-time discrete-event platform based on Matlab and Network Simulator 3 (NS3)[1].

6.1 Introduction

In Section 2.6 an outline of the integration of modern random access techniques in the 5G architecture has been given. The 5G densification strategy relies on the deployment of a huge number of base stations (BSs), whose installation can be highly remunerative in the urban areas, but may result not

[1]This chapter is based on F. Babich, M. Comisso, A. Cuttin, M. Marchese, and F. Patrone, "Nanosatellite-5G integration in the millimiter wave domain: A full top-down approach", *IEEE Transactions on Communications*, under review.

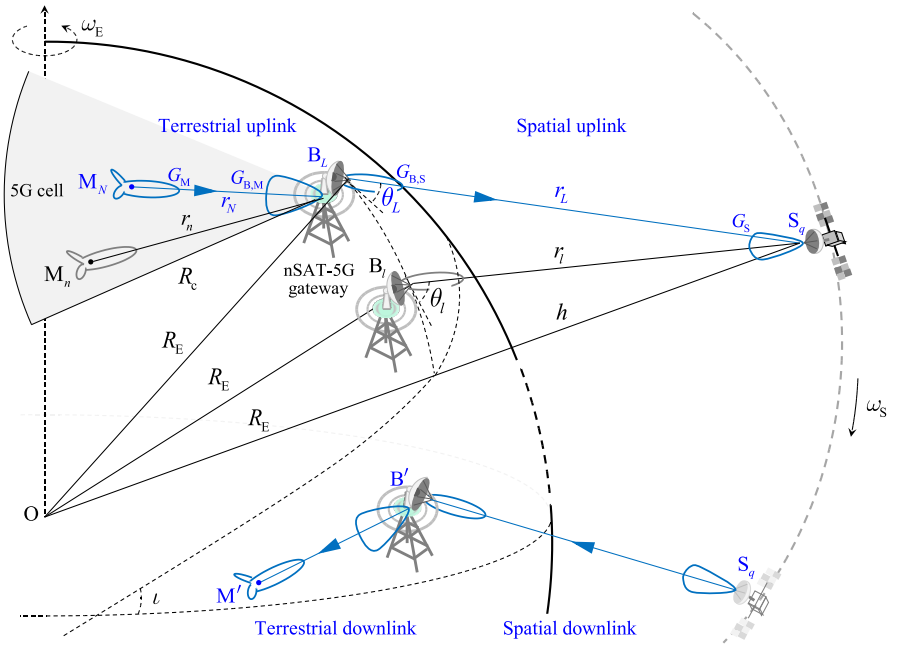

Figure 6.1: End-to-end communication scenario.

profitable in the remote ones. In this second situation, a fundamental support to the communications between far 5G BSs may be provided by nSAT constellations, thus suggesting the development of a hybrid nSAT-5G network.

The problem of integrating nSAT and 5G technologies for mobile broadband coverage has already attracted the attention of the satellite research community [94, 95, 96, 97]. In particular, the application of cognitive radio to a hybrid nSAT-5G communication has been addressed in [94], where a software-defined radio platform has been developed to investigate the access and frequency allocation issues. A dynamic hybrid terrestrial-satellite backhaul network has been proposed in [95], by considering the functionalities that must be introduced at the physical (PHY), medium access control (MAC), and network (NET) layers to enable the reconfiguration of the terrestrial topology. An end-to-end hybrid satellite-terrestrial network is also presented in [96], which provides a detailed theoretical analysis of the coverage probability, and of the spectral and energy efficiencies for different node densities. The co-channel interference at 28 and 70 GHz between 5G systems and mmWave fixed satellite services (FSSs) has been studied in [97], showing that protection mechanisms may be introduced in the 5G devices to mitigate the interference towards the FSS without significantly affecting the performance of the 5G network. Also, as presented in Section 2.4, outstanding results have been achieved on random multiple access for cellular and satellite networks, where the need of managing inhomogeneous traffic conditions and

the impossibility of using carrier sensing mechanisms have determined since several years the adoption of slotted-Aloha protocols. The introduction of SIC has indeed enabled the design of the CRDSA [13], a high-capacity iterative repetition-based algorithm recently included in the DVB-RCS2 standard [58], and of the CSA protocol [20], a more evolved energy-efficient iterative solution presently under consideration for forthcoming 5G systems [98]. From the point of view of an integrated nSAT-5G system, it may be really fruitful to use these novel algorithms to complement a DTN architecture [99, 100], which has been already successfully applied to challenging LEO satellite scenarios for data exchange purposes [101]. The DTN architecture, which operates through a store and forward mechanism, is based on the introduction of an overlay above the transport or the other lower layer protocols. Nodes with such an overlay are able to handle delays and disruptions by storing the application data inside their buffer until the next hop becomes available [102]. Simultaneous end-to-end connectivity is hence not required, thus making the DTN solution specifically suited for a hybrid nSAT-5G network.

In light of these considerations, this chapter addresses a complete top-down network architecture for an integrated nSAT-5G system operating in the mmWave domain. Specifically, the contribution presented, that complements in a novel fashion the DTN network architecture, is the revisiting of the performance of the CSA and CRDSA random access schemes in the presence of capture by adopting reception criteria adherent to the estimated SINR distributions.

This revisitation benefits from a detailed PHY analysis that provides the distribution of the SINR at each mmWave link in a propagation environment characterized by shadowing, fading, interference, and noise. It has been implemented in a Matlab function to be integrated in a Matlab-NS3 discrete-time discrete-event platform, with the aim to investigate the use of the conceived network architecture for non-delay-sensitive data transport applications.

On the other hand, the NS3 module implements a novel buffer Buffer Aware Contact Graph Routing (CGR) (BA-CGR) algorithm for the DTN layer and the definition of an extension block of the Bundle Protocol (BP). Its aim is to deal with the presence of heterogeneous areas between sources and destinations, so as to forward and exploit information about the storing capabilities of the intermediate nodes and the amount of data that can be exchanged during each contact. The definition and description of the BA-CGR algorithm and of the BP is not within the scope of this chapter, but for the sake of completeness it can be found in Appendix D.

6.2 Scenario

Consider a 5G cell shared by N MSs that operate as data sources, where M_n ($n = 1, \ldots, N$) denotes the generic source, as in Figure 6.1. This cell is covered by a target BS B_L belonging to a set of L BSs that can also establish

a connection with a generic nanosatellite S_q ($q = 1, \ldots, Q$), which is part of a constellation of Q nSATs. Within this constellation, just one nSAT at a time is visible to the L BSs. To establish the connection, the generic BS B_l ($l = 1, \ldots, L$) is equipped with two mmWave radio interfaces, a terrestrial 5G one and a satellite one, thus it may operate as a nSAT-5G gateway. When a target MS M_N has to communicate with a destination M', lying in a cell managed by a 5G BS B' covered by the orbit of S_q, S_q acts as relay. In particular, S_q uploads the data from B_L during the $B_L - S_q$ visibility period and downloads them to B' during the $S_q - B'$ visibility period. Hence, the $M_N - M'$ end-to-end connection involves four links: the terrestrial uplink (TU) $M_N - B_L$, the space uplink (SU) $B_L - S_q$, the space downlink (SD) $S_q - B'$, and the terrestrial downlink (TD) $B' - M'$.

Even if the depicted scenario represents a common application for an integrated terrestrial-satellite network, it is characterized by some specific features that require a careful design of the network architecture. In fact, since the LEO satellites move on subsynchronous orbits, their footprints are not the same during all the orbit time, thus, in most cases, B_L and B' are not covered by the same satellite at the same time. Also in these cases the end-to-end connection remains mandatory for a lot of transport protocols used in classical networks. Besides, the technology that must be managed is necessarily heterogeneous, since 5G and satellite devices are involved, and the end-to-end connection is composed by a concatenation of time-disjoint transient links. The terrestrial links between MSs and BSs may be, in fact, generally assumed active except for unpredictable and temporary faults, while the satellite links between BSs and nSATs may be unavailable for extended periods of time and may be subject to time-varying propagation delays. Thus, storage constraints exist both at BSs and nSATs, since the packets have to be forwarded through the satellite link just during the visibility period. Moreover, while the downlinks may be reasonably assumed to rely on a reserved access, the uplinks have to implement random access mechanisms to cope with the unpredictability of the sources activity. Finally, concerning the PHY layer aspects, it is necessary to consider that the mmWave links suffer from strong attenuations, whose effects may be further exacerbated by the disruptions due to the satellite movement and by the large delays due to the high distances between nSATs and BSs.

6.2.1 Architecture

To deal with the above discussed issues, this study presents a novel network architecture obtained combining the DTN paradigm with coded random access (Figure 6.2). In particular, for the satellite links, the DTN architecture is implemented by the Bundle Layer (BL) [103], where the term bundle refers to a message consisting of a payload containing the application data and of a header containing the additional information necessary for the end-to-end delivery. The BL is directly interfaced with the MAC layer used in satellite

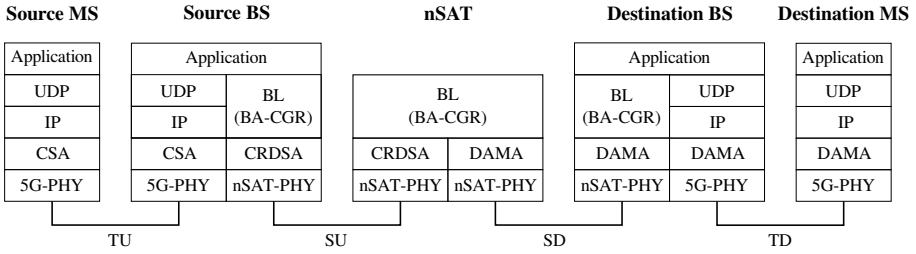

Figure 6.2: Network architecture.

links. The main functionalities of the NET and transport layers, such as routing, are managed at the BL. In this way, the architecture becomes lighter and the computational effort for the headers encapsulation and de-encapsulation is reduced, thus resulting attractive for on-board nSAT implementation. The BSs have hence a User Datagram Protocol (UDP)/Internet Protocol (IP) interface towards the MSs and a DTN satellite interface to upload/download data to/from the nSATs. The BSs, acting as DTN gateways, have also the application layer needed to perform the bundle encapsulation/de-encapsulation procedures, while the nSATs are just DTN relays with a satellite interface, thus they do not need the application layer. This type of DTN architecture is hence composed of heterogeneous areas where intermediate nodes (BSs and nSATs) are DTN-based, while the MSs are UDP/IP-based and do not implement the BL.

The BP relies on the BA-CGR algorithm, which enables the correct packet forwarding to the destination through the complete knowledge of the future contacts [104]. The BA-CGR solution accounts for the nSAT buffer occupancy, which is more critical than that of the BS, since nSATs have to satisfy more stringent size and weight constraints. The aim is to avoid nSAT buffer overflows and routing path calculations towards future contacts without enough remaining space. Below the BL, the multiple access algorithms are selected in agreement with current 5G and nSAT proposals. Accordingly, the MAC layer for the downlinks relies on DAMA, while that for the uplinks relies on a contention basis to manage the typical irregular traffic of terrestrial users. More precisely, the CSA scheme is selected for the random access at the TU to provide a high-capacity interface [20, 98], while the CRDSA protocol is selected for the random access at the SU to match the recent upgrade of the DVB-RCS2 standard [13, 58]. Both schemes combine IC with proper retransmission (CRDSA) and coding (CSA) policies to increase the MAC layer throughput.

In summary, the data packets generated by the application layer of M_N are sent through a UDP/IP interface to B_L by the CSA random access protocol. The BS B_L encapsulates the received packets in data bundles, which are stored in its buffer, and uploads them on the nSAT selected by the BA-CGR algorithm through the CRDSA random access protocol. The chosen

nSAT keeps the received bundles stored in its buffer until it enters in contact with B′, which de-encapsulates them and sends the corresponding packets to M′. In this way, we get a transparent bidirectional communication between each pair of MSs avoiding the use of ad-hoc devices or the implementation of software modifications. It is important to remark the relay action of the BL, which allows not only the information storage at intermediate nodes, but also the implementation of dedicated protocol stacks for single network portions. A more exhaustive and detailed characterization of the developed architecture is presented in the next sections. This characterization follows a bottom-up description by starting with the analysis of the mmWave PHY layer (Section 6.3), and then moving to the presentation of the protocols implemented at the MAC (Section 6.4), NET and higher (Section 6.5) OSI layers.

6.3 PHY layer

From a PHY layer point of view, each link of the $M_N - M'$ end-to-end connection is characterized by a specific SINR statistic requiring a distinct estimation. To deal with this problem, some reasonable assumptions are introduced to limit the complexity of the analysis and avoid cumbersome notations.

Firstly, during a contact, a nSAT follows a circular orbit, thus its angular velocity in an Earth-centered Earth-fixed (ECEF) coordinate system is constant and given by [105]:

$$\omega \cong \sqrt{\frac{\mu_E}{(R_E + h)^3}} - \omega_E \cos \iota = \omega_S - \omega_E \cos \iota, \tag{6.1}$$

where μ_E is the geocentric gravitational constant, R_E is the Earth radius, h is the orbit altitude, ω_E is the angular velocity of the Earth rotation, $\iota \in [0°, 90°]$ is the inclination angle, and $\omega_S = \sqrt{\mu_E/(R_E + h)^3}$ is the angular velocity of the nSAT in an Earth-centered inertial (ECI) coordinate system. Besides, a BS B_l sees the nSAT from an elevation angle θ_l lying between a minimum value $\bar{\theta}_1$ and a maximum one $\bar{\theta}_2$, with $0° \leqslant \bar{\theta}_1 \leqslant \bar{\theta}_2 \leqslant 90°$. In these conditions, the visibility period is [105]:

$$v = 2\zeta/\omega, \tag{6.2}$$

where $\zeta = \arccos(\bar{\eta}_1/\bar{\eta}_2)$, $\bar{\eta}_i = \cos[\gamma(\bar{\theta}_i)]$ for $i = 1, 2$, and:

$$\gamma(x) = \arccos\left(\frac{R_E}{R_E + h}\cos x\right) - x. \tag{6.3}$$

Secondly, all nodes (MSs, BSs, nSATs) employ an identical transmission power P_t, and use receivers characterized by the same noise figure $\mathcal{F}$ and bandwidth B_W. Therefore, denoting as χ_B the Boltzmann constant, the noise powers at a terrestrial and satellite receiver may be evaluated, respectively, as [106]:

$$\rho_E = \chi_B T_E B_W \mathcal{F}, \tag{6.4a}$$

$$\rho_S = \chi_B T_S B_W \mathcal{F}, \tag{6.4b}$$

where T_E and T_S are the terrestrial and satellite antenna temperatures, respectively.

Thirdly, all channels are symmetric. To enable a compact analytical treatise, a Friis transmission model is adopted for the path-loss, thus considering a path-loss exponent equal to 2 on all links. This hypothesis is consistent with recent measurements in 5G line-of-sight (LOS) scenarios [2]. The space links are also subject to fast-fading and additional atmospheric attenuations [106], while the terrestrial links to mid-scale fading, which has been proved to be significant in 5G communications [2]. Each uplink is further affected by interference due to the contention process during the data upload, but not to the traffic on the other uplink, since non-overlapping frequency bands are assumed for the TU and SU.

According to these hypotheses, the following subsections provide estimations for the SINR distributions on the four links, with the purpose of getting a reliable physical basis for the application of the functionalities introduced at the upper MAC and DTN layers.

6.3.1 Terrestrial links

As discussed above, the 5G TU is subject to path-loss, shadowing, interference, and noise. The first two phenomena directly influence the power p_n received by the target BS from the generic MS M_n. This quantity may be hence expressed as:

$$p_n = \frac{P_t G_M G_{B,M}}{\alpha {r_n}^2} \xi = \frac{\chi_E}{{r_n}^2} \xi, \quad n = 1, \ldots, N \tag{6.5}$$

where G_M and $G_{B,M}$ are the maximum antenna power gains of a MS, and of a BS at its terrestrial radio interface, respectively, the distance r_n is the realization of a random variable (r.v.) derived from a uniform distribution (u.d.) inside a disk of radius R_c (Figure 6.1), α is the floating intercept of the path-loss functional model [2], ξ is the realization of a log-normally distributed r.v., and $\chi_E = P_t G_M G_{B,M}/\alpha$. Since the N MSs contend for channel access, the SINR at the TU $M_N - B_L$ is:

$$s = \frac{p_N}{\sum_{n=1}^{N-1} p_n + \rho_E}. \tag{6.6}$$

A proper mathematical analysis of this scenario allows one to formulate the following proposition.

Proposition 1. *The complementary cumulative distribution function (ccdf) of the SINR for the TU when N contending MSs are present may be estimated as:*

$$\bar{F}_S^{TU}(s; N) \cong \frac{1}{2^N} \int_{s\rho_E}^{+\infty} \frac{I_1(p_N)}{p_N} \left[I_0\left(\frac{p_N - s\rho_E}{sH_{N-1}} \right) - I_1\left(\frac{p_N - s\rho_E}{sH_{N-1}} \right) \right]^{N-1} \mathrm{d}p_N, \tag{6.7}$$

Table 6.1: PHY layer parameters [2, 107].

$\mu_{\mathrm{E}} \cong 398600\ \mathrm{km}^3/\mathrm{s}^2$	$T_{\mathrm{E}} = 270$ K	$\iota = 50^\circ$
$R_{\mathrm{E}} \cong 6371$ km	$R_{\mathrm{c}} = 100$ m	$\bar{\theta}_1 = 10^\circ$
$\omega_{\mathrm{E}} \cong 7.29 \cdot 10^{-5}$ rad/s	$G_{\mathrm{M}} = 24$ dB	$\bar{\theta}_2 = 90^\circ$
$\chi_{\mathrm{B}} \cong 1.38 \cdot 10^{-23}$ J/K	$G_{\mathrm{B,M}} = 24$ dB	$G_{\mathrm{B,S}} = 50$ dB
$c \cong 3.00 \cdot 10^8$ m/s	$\alpha = 61.4$ dB	$G_{\mathrm{S}} = 30$ dB
$B_{\mathrm{W}} = 450$ MHz	$\sigma = 5.8$ dB	$\nu = 27.2$ GHz
$\mathcal{F} = 10$ dB	$T_{\mathrm{S}} = 100$ K	$A = 4$ dB
$P_{\mathrm{t}} = 1$ W	$h = 400$ km	$m = 2$

where $H_\kappa = \sum_{\kappa'=1}^{\max(\kappa,1)} \frac{1}{\kappa'}$ *coincides with the harmonic number of order* κ *when* $\kappa \in \mathbb{N}^+$, *and:*

$$I_j(x) = \left(\frac{\chi_{\mathrm{E}}}{R_{\mathrm{c}}^2 x}\right)^j e^{j\frac{\sigma^2}{2}} \operatorname{erfc}\left\{\frac{1}{\sqrt{2}}\left[\frac{1}{\sigma}\log\left(\frac{\chi_{\mathrm{E}}}{R_{\mathrm{c}}^2 x}\right) + j\sigma\right]\right\}, \tag{6.8}$$

for $j = 0, 1$, *in which* σ *is the shadowing standard deviation and* $\operatorname{erfc}(\cdot)$ *is the complementary error function.*

Proof. See Appendix A □

This proposition includes also the TD case. In fact, the conditions of channel symmetry and antenna reciprocity, combined with the absence of interference due to the usage of the DAMA protocol for the downlink communications, imply that the ccdf of the SINR for the TD may be directly obtained from (6.7) as:

$$\bar{F}_S^{\mathrm{TD}}(s) = \bar{F}_S^{\mathrm{TU}}(s; 1). \tag{6.9}$$

6.3.2 Space links

The mmWave SU is subject to path-loss and atmospheric attenuations, fast-fading, interference, and noise. In this case, the distance r_l between the nSAT and the BS B_l (slant range), may be evaluated from geometrical considerations (Figure 6.1), as:

$$r_l = \sqrt{h^2 + 2hR_{\mathrm{E}} + R_{\mathrm{E}}^2 \sin^2\theta_l} - R_{\mathrm{E}} \sin\theta_l. \tag{6.10}$$

Given this relationship, the power p_l received by the nSAT from B_l can be calculated as:

$$p_l = \frac{P_{\mathrm{t}} G_{\mathrm{B,S}} G_{\mathrm{S}}}{A}\left(\frac{c}{4\pi\nu r_l}\right)^2 \psi = \frac{\chi_{\mathrm{S}}}{r_l^2}\psi, \quad l = 1, \ldots, L \tag{6.11}$$

where $G_{\mathrm{B,S}}$ is the maximum antenna power gain of B_l at its space radio interface, G_{S} is the maximum antenna power gain of the nSAT, A is the additional

attenuation due to atmospheric phenomena (rain, clouds, scintillation,...), c is the speed of light in vacuum, ν is the carrier frequency, ψ is the realization of a gamma distributed r.v. accounting for Nakagami-m fading, and

$$\chi_{\mathrm{S}} = \frac{P_{\mathrm{t}} G_{\mathrm{B,S}} G_{\mathrm{S}} c^2}{16 A \pi^2 \nu^2}. \tag{6.12}$$

Similarly to the TU, the SU relies on a contention access mechanism, thus the target communication at the SU experiences a SINR:

$$s = \frac{p_L}{\sum_{l=1}^{L-1} p_l + \rho_{\mathrm{S}}}. \tag{6.13}$$

A manageable estimation of SINR distribution in this scenario may be derived for the values $m = 1, 2$ of the Nakagami parameter. This allows the formulation of the following proposition.

Proposition 2. *The ccdf of the SINR for the SU when L contending BSs are present may be estimated, for $m = 1, 2$, as:*

$$\bar{F}_S^{\mathrm{SU}}(s; L) \cong \int_{s\rho_{\mathrm{S}}}^{+\infty} V_1(p_L) \left[V_0\left(\frac{p_L - s\rho_{\mathrm{S}}}{s H_{L-1}} \right) + 1 \right]^{L-1} \mathrm{d}x, \tag{6.14}$$

where:

$$\begin{aligned} V_j(x) = \frac{(-1)^j}{2^{2m+j-1}\zeta x^j} \sqrt{\frac{\chi'_{\mathrm{S}}}{x}} \sum_{i=1}^{2} (-1)^i \Bigg\{ \sqrt{\pi} \left[(2\varepsilon x + 1)^{m+j-1} + 2(m-1) \right] e^{-\varepsilon x} \cdot \\ \cdot \operatorname{erf}\left[\sqrt{(\bar{\varsigma}_i - \varepsilon) x} \right] + 2 \Big[(m-1) \cdot (4\bar{\varsigma}_i^2 x^2 + 2\varepsilon x + 1)^j + \\ + 2(m - mj + 2j - 1)\bar{\varsigma}_i x + m \Big] \cdot e^{-\bar{\varsigma}_i x} \sqrt{(\bar{\varsigma}_i - \varepsilon) x} \Bigg\} + \\ - (-1)^j \left[\bar{\varsigma}_1^j (\bar{\varsigma}_1 x)^{m-1} - (m-1)(j-1) \right] e^{-\bar{\varsigma}_1 x}, \end{aligned} \tag{6.15}$$

for $j = 1, 2$, in which

$$\chi'_{\mathrm{S}} = \frac{m \chi_{\mathrm{S}}}{\bar{\eta}_2 R_{\mathrm{E}} (R_{\mathrm{E}} + h)}, \tag{6.16}$$

$$\varepsilon = \frac{m[h^2 + 2R_{\mathrm{E}}(1 - \bar{\eta}_2)(R_{\mathrm{E}} + h)]}{\chi_{\mathrm{S}}}, \tag{6.17}$$

$$\bar{\varsigma}_i = \frac{m[\bar{\eta}_i (R_{\mathrm{E}} + h) - R_{\mathrm{E}}]^2}{(\chi_{\mathrm{S}} \sin^2 \bar{\theta}_i)} \tag{6.18}$$

for $i = 1, 2$, and $\operatorname{erf}(\cdot)$ is the error function.

Proof. See Appendix B □

Also in this case, one may infer the SINR distribution for the SD from Proposition 2. In fact, the absence of interference due to the adoption of the DAMA protocol and the terrestrial location of the BS receiver imply that the ccdf of the SINR for the SD may be evaluated replacing ρ_S by ρ_E in (6.14) for $L = 1$, thus obtaining after integration:

$$\bar{F}_S^{SD}(s) \cong -V_0(s\rho_E). \tag{6.19}$$

To clarify the results provided by Propositions 1 and 2, two sets of SINR ccdfs are presented by adopting the PHY layer parameters in Table 6.1. These values, which will be used as the reference set, are selected according to recent channel measurements at 28 GHz for the 5G links [2], and to operative frequency plans of LEO satellites working in the K-band for the mmWave space links [107].

The first set of results is referred to the TD and the TU for different N values (Figure 6.3 (a)), while the second set is referred to the SD and the SU for different L values (Figure 6.3 (b)). All theoretical curves (lines) are validated by independent Monte Carlo simulations (markers) to check the accuracy of the developed analysis. From the reported figures, one may notice that the interference results the sole responsible for the SINR reduction at the terrestrial links. This is due, on one hand, to the limited radius of the 5G cells (not larger than few hundreds of meters), which implies short communication distances, and, on the other hand, to the assumed LOS conditions, which imply that the received power is always higher than the noise. Both interference and noise instead affect the space links, since the communication distances become necessarily longer. As expected, the noise has a stronger impact on the SD, since the antenna temperature at a BS is larger than that at a nanosatellite.

As a final remark, it is interesting to observe that, even if Equations (6.7) to (6.9) and Equations (6.14) to (6.19) may seem formally elaborated, they have the considerable advantage of providing the statistical distribution of the SINR in the presence of several physical phenomena by a unique numerical integration. This computationally cheap approach allows not only the investigation of the PHY layer performance of an integrated nSAT-5G system, but also a realistic modeling of the evolution of the access schemes implemented at the MAC layer, whose description is the aim of the next section.

6.4 MAC layer

From a MAC layer perspective, the use of the DAMA protocol for the downlink communications implies that the reception at the TD and SD directly depends on the propagation conditions. The usage of CRDSA at the SU and of CSA at the TU, which adopt IC to constructively exploit the collisions, requires instead to jointly consider propagation and interference for establishing the result of a transmission [20, 13]. For both schemes, the conventional

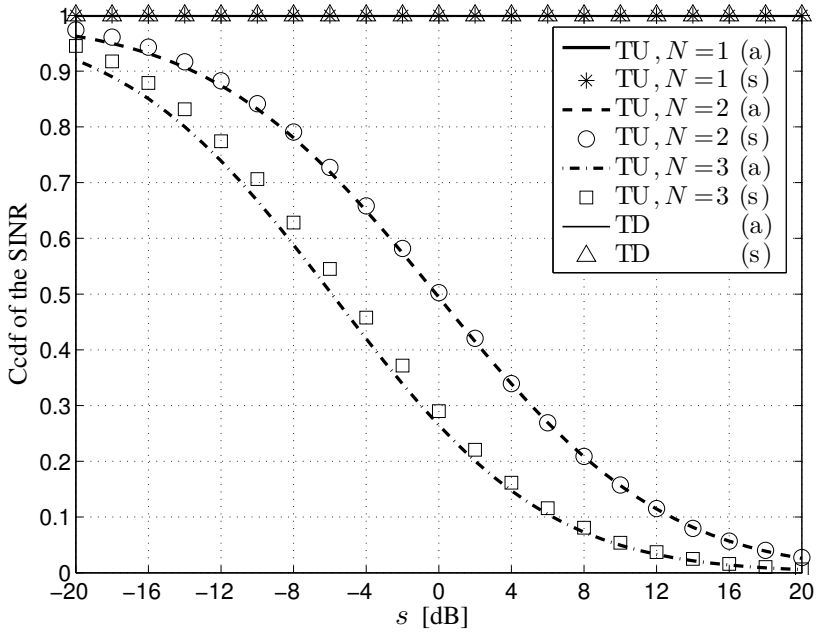

(a)

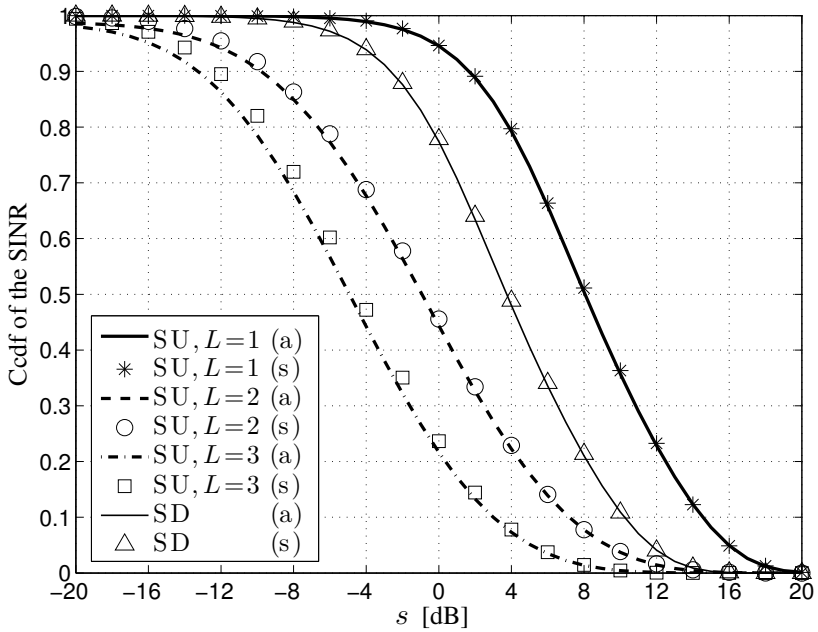

(b)

Figure 6.3: Ccdfs of the SINR: (a) terrestrial links, (b) space links (a: analysis, s: simulation).

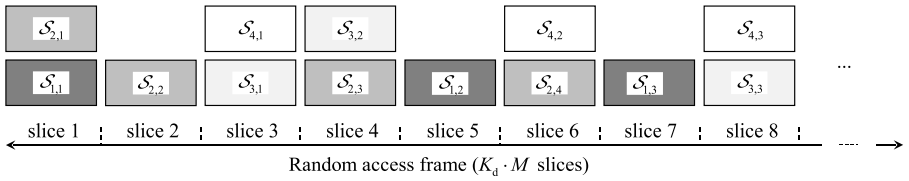

Figure 6.4: TU MAC frame.

performance estimation relies on the assumptions that an uncollided transmission is received and that the collided ones do not provide any information unless they are successively cleaned by IC. In practice, instead, the combined effect of noise and signal fluctuation might determine the failure of an uncollided transmission, while the capture effect might enable the reception of some transmissions even if they remain collided. Therefore, a reliable evaluation of the MAC layer performance has necessarily to account for the capture event, whose occurrence, also, does not require the implementation of novel functionalities, since the possibility to capture a not too interfered transmission is an intrinsic capability of any receiver. Accordingly, the evolution of CSA and CRDSA may be reconsidered by jointly accounting for capture and IC. To this aim, some preliminary assumptions are adopted.

Firstly, even if CSA and CRDSA may be applied to a multi-frequency time division multiple access context, the discussion is here developed focusing on a single carrier for simplicity [13]. Secondly, both for the TU and SU, the timeline is subdivided in frames of M slots, where each slot has a duration equal to the transmission time of a packet/bundle. A contending source (MS or BS), which is assumed frame- and slot-synchronous, attempts the transmission of at most one packet/bundle in the respective frame [13, 20]. Thirdly, IC is assumed ideal, since the residual interference after IC does not significantly affect the CSA and CRDSA performance [13, 20]. The success probability for a transmission is established adopting a threshold that accounts for the modulation and the channel coding rate. More precisely, for CRDSA and for the downlink communications, the threshold is established considering the required SINR s. Since (6.9) and (6.19) exactly represent the probabilities that the SINR be larger than s, this latter assumption implies that the success probabilities at the TD and SD, which rely on a demand assignment, are immediately given by $C^{\mathrm{TD}}(s) = \bar{F}_S^{\mathrm{TD}}(s)$ and $C^{\mathrm{SD}}(s) = \bar{F}_S^{\mathrm{SD}}(s)$, respectively. Instead, for CSA, which involves packet correcting codes, the threshold is established adopting the sustainable information rate [29]. According to these assumptions, the next subsections revisit the evolution of CSA and CRDSA by considering the combined effect of capture and IC, in order to clarify their implementation in the designed DTN architecture.

6.4.1 Terrestrial uplink

CSA, as presented in Section 2.5, is based on the erasure channel, in which just two events are possible for a segment: success (all of its information available) and loss (none of its information available). The presence of capture completely changes this perspective. In an actual receiver, in fact, on one hand the propagation conditions might deteriorate an uncollided transmission, and, on the other hand, a segment involved in an unresolved collision might anyway provide a residual information. This situation can be modeled by the average rate [29], which considers, for each packet, the SINRs $s_1, ..., s_K$ experienced by its K segments. To this aim, rather than using the ideal, and hence optimistic, Shannon bound, which might require the introduction of upper limits on the SINR to avoid possible overestimations of the performance [108], one may more realistically consider a Quadrature Phase Shift Keying (QPSK) modulation, for which a reliable capacity expression exists [109]. Accordingly, defining the coefficients $a_1 \cong -1.29$, $a_2 \cong 0.93$, $a_3 \cong 0.01$, and a margin $b = 2.5$ dB to account for the non-ideality of the code, the average rate λ may be derived by first evaluating the sequence of limiting rates as [109]:

$$\lambda_k = \lambda_k(s_k) \cong 2\left[1 - e^{a_1\left(\frac{s_k}{2b}\right)^{a_2}+a_3}\right], \quad k = 1, ..., K \tag{6.20}$$

and subsequently keeping their average value [29]:

$$\lambda = \frac{1}{K}\sum_{k=1}^{K}\lambda_k. \tag{6.21}$$

Since a modulation of order $\varsigma = 4$ is employed (QPSK), in the presence of a code rate K_d/K, the correct packet reception occurs if

$$\lambda \geq \bar{\lambda} = \frac{K_\mathrm{d}\log_2\varsigma}{K} = \frac{2K_\mathrm{d}}{K}. \tag{6.22}$$

This concept may be combined with the SINR analysis in Section 6.3.1 to formulate the following proposition.

Proposition 3. *The packet success probability at a TU using CSA with ideal IC and QPSK modulation when $\bar{\lambda}$ information bits per symbol are required may be estimated by:*

$$C^{\mathrm{TU}}(\bar{\lambda}; N_1, \ldots, N_K) \cong \int_0^{+\infty}\!\!\cdots\int_0^{+\infty} \bar{F}_S^{\mathrm{TU}}\left\{\left[\frac{1}{a_1'}\log\left(2 - K\bar{\lambda} - \sum_{k=1}^{K-1}\lambda_k(s_k)\right) + - a_3'\right]^{\frac{1}{a_2}}; N_K\right\} \cdot \prod_{k=1}^{K-1} f_S^{\mathrm{TU}}(s_k; N_k)\mathrm{d}s_1 \ldots \mathrm{d}s_{K-1}, \tag{6.23}$$

where

$$a_1' = \frac{a_1}{(2b)^{a_2}}, \tag{6.24}$$

$$a_3' = \frac{a_3 + \log 2}{a_1'}, \tag{6.25}$$

N_k is the number of MSs that transmit in the slice containing the k-th segment of the packet, and the SINR probability density function (pdf) is:

$$f_S^{\mathrm{TU}}(s;N) \cong \frac{1}{2^{N_S}} \left\{ \delta_{N,1} I_1(s\rho_{\mathrm{E}}) + (N-1) \cdot \int_0^{+\infty} \frac{I_1(x) I_1\left[s(H_{N-1}x + \rho_{\mathrm{E}})\right]}{x\left[I_0(x) - I_1(x)\right]^{2-N}} \mathrm{d}x \right\}, \tag{6.26}$$

in which $\delta_{N,1}$ is the Kronecker delta

$$\delta_{N,1} = \begin{cases} 1 & N = 1 \\ 0 & \textit{otherwise} \end{cases}. \tag{6.27}$$

Proof. See Appendix C □

Exploiting this proposition, the evolution of CSA in the presence of capture may be revisited. Consider again Figure 6.4, now applying (6.23) with $\varsigma = 8$ and starting the processing of a packet when the last of its segments is arrived. At the first iteration, the first processed packet is packet 1, for which $C^{\mathrm{TU}}(4/3;2,1,1) \cong 0.92$. This leads, for packet 2, to $C^{\mathrm{TU}}(1;1,1,2,2) \cong 0.90$, if packet 1 is captured (that is, $\mathcal{S}_{1,1}$ is cancelled), or to $C^{\mathrm{TU}}(1;2,1,2,2) \cong 0.64$, if packet 1 is not captured. This result, in turn, influences the reception of packet 3, for which we have $C^{\mathrm{TU}}(4/3;2,1,2) \cong 0.51$, if packet 2 is captured (that is, $\mathcal{S}_{2,3}$ is cancelled), or $C^{\mathrm{TU}}(4/3;2,2,2) \cong 0.24$, if packet 2 is not captured. If at least one among packets 1,2,3 is captured, a second iteration is carried out to check if other captures can occur. Otherwise, a second iteration is not necessary since no modifications of the random access frame have occurred with respect to the first iteration. In general, in the receiver implementation, the capture experiment for a packet is repeated just if its success probability changes because of one or more cancellations at the previous iteration. Besides, to avoid possible unrealistic overestimations of the number of successes, a maximum of two capture experiments is allowed for each packet.

6.4.2 Space uplink

Differently from CSA, CRDSA adopts a repetition approach by transmitting two copies of a bundle in two different slots [13]. If one copy is successful, the receiver recovers and cancels the other, thus allowing the possible recovery of further initially collided bundles. For example, in the case reported in Figure 6.5, where $\mathcal{B}_{l,k}$ identifies the k-th copy of the l-th bundle,

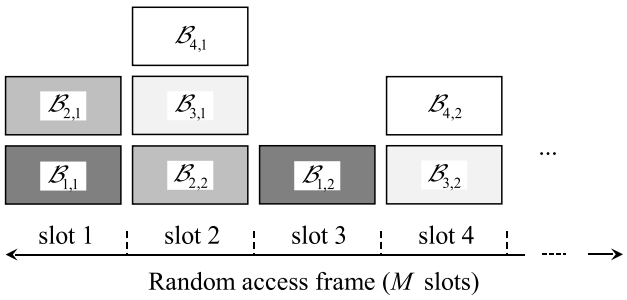

Figure 6.5: SU MAC frame.

$\mathcal{B}_{1,2}$ is uncollided, thus, at the first iteration, bundle 1 is received and $\mathcal{B}_{1,1}$ is cancelled. This enables to clean $\mathcal{B}_{2,1}$, and hence to receive, at the second iteration, bundle 2 and cancel $\mathcal{B}_{2,2}$. Bundles 3,4 are not received, since their copies are involved in unresolved collisions. Also in this case, the capture event may modify this evolution. Since in CRDSA no packet correcting codes are adopted, the success probability for a copy transmitted in a slot is directly given by (6.14), thus $C^{\mathrm{SU}}(s;L) = \bar{F}_S^{\mathrm{SU}}(s;L)$, where s is the SINR threshold and L is the number of BSs that have transmitted in that slot. Consider again Figure 6.5 with $s = 2.23$ dB ($\cong 5/3$) [110, Tab. 13], for which the corresponding success probabilities can be directly inferred from Figure 6.3(b) as $C^{\mathrm{SU}}(5/3;1) \cong 0.88$, $C^{\mathrm{SU}}(5/3;2) \cong 0.31$, $C^{\mathrm{SU}}(5/3;3) \cong 0.13$. At each iteration, the receiver performs at most one capture experiment per slot by sequentially moving from the first one. Thus, at the first iteration, $\mathcal{B}_{1,1}$ is received with a 31% probability, $\mathcal{B}_{2,2}$ with a 13% probability, $\mathcal{B}_{1,2}$ with an 88% probability, and $\mathcal{B}_{3,2}$ with a 31% probability. Depending on the results of the capture experiments, the copies of the successful bundles may be cancelled or not, and, at the second iteration, further capture experiments are carried out for the sole copies experiencing a variation of the success probability with respect to the previous iteration, with a maximum of two overall experiments per copy, consistently with the approach previously described for CSA.

To clarify the impact of the success probability on the decoding procedure, Figure 6.6 compares the throughput of the CSA and CRDSA schemes with and without capture using the parameters in Table 6.2, which will be also adopted for the rest of the chapter. To obtain a fair comparison, no limits have been imposed on the number of iterations in the absence of capture.

Table 6.2: MAC layer parameters.

$s = 2.23$ dB [110, Tab. 13]
$\varsigma = 4$ bits/symbol
$K_{\mathrm{d}} = 2$
$f_{\mathcal{C}}(K=3) = 2/3$, $f_{\mathcal{C}}(K=4) = 1/3$ [20, Tab. II]]

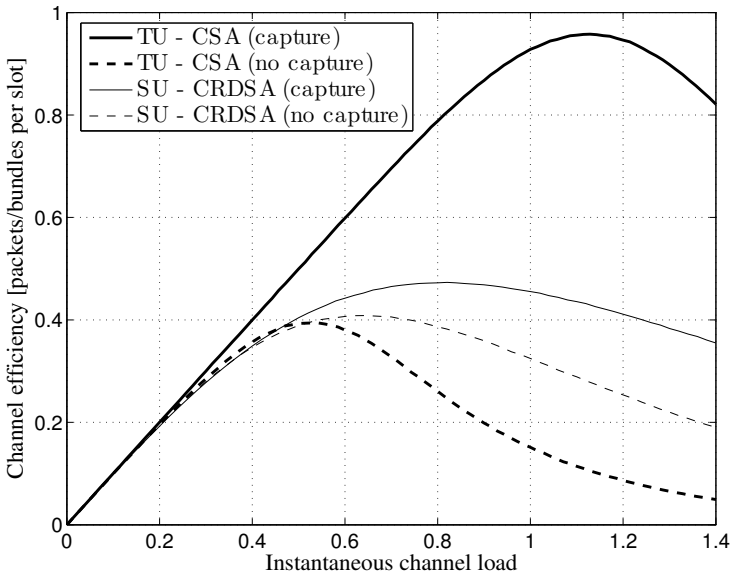

Figure 6.6: Channel efficiency as a function of the instantaneous offered load for the CSA and CRDSA schemes in the presence and in the absence of capture.

Observe that both the threshold on each information rate at the TU and that on the SINR at the SU are coherent with the selection of a QPSK modulation and a rate 3/5, which represents the rate of the scheme for CSA [20], and the rate of the encoder for CRDSA [110, Tab. 13]. In particular, for CSA, the two possible thresholds on the information rate are $\bar{\lambda} = 4/3$ and $\bar{\lambda} = 1$ information bits per symbol when $K = 3$ and $K = 4$ encoded segments are respectively generated.

The figure, which is obtained for $N = L = 50$ and $M = 35$, reveals that in general the capture effect provides considerable improvements for both schemes. In particular, the throughput increase in the presence of capture for CRDSA is not strictly due to an increase of the successful receptions with respect to the absence of capture, but to a positive balance between unsuccessful receptions due to the noise and successful receptions due to the captured collided replicas. This effect is also experienced by the different segments when CSA is applied in the presence of capture. However, in this case, the throughput benefits are mainly due to a combination of coded random access and SINR fluctuations, which generates a beneficial phenomenon of interference diversity among the slices containing different segments.

6.5 NET and higher layers

Once the access rules are established, the subsequent functionality that must be addressed concerns the routing of the packets/bundles from the source to the destination. In the presented network architecture, the routing process

is split into three portions (Figs. 6.1 and 6.2): the IP routing from M_N to the terrestrial interface of B_L, the DTN routing from the satellite interface of B_L to the satellite interface of B' (DTN portion of the network), and the IP routing from the terrestrial interface of B' to M'. This splitting means that, in the terrestrial links, the routing functionality lies at the NET layer and is carried out by the IP protocol, while, in the satellite links, it lies at the DTN layer and is carried out by the BP. In details, in the first portion, M_N sends its data packets to B_L, which acts as the default nSAT-5G gateway for M_N. In the second portion, B_L encapsulates the received data packets in data bundles adding the standard primary bundle header [103], and a properly defined bundle extension block (BEB), containing two further fields: the Destination IP address (4 octets) and the Type (1 octet). This latter field is inserted to discriminate between data bundles, which contain the application data, and status bundles, which contain the nSAT buffer occupancy information. In the third portion, B' de-encapsulates the received data bundles, reads the Destination IP address stored in the BEB, and sends the extracted data packets to M'. Within the DTN portion of the network, the Type field allows a BS to perform the routing decision considering also the number of bundles present in the nSAT buffer. To enable this capability, an extension of the widely adopted CGR algorithm, called BA-CGR, is described in Appendix D[2].

6.6 Application

6.6.1 Simulation platform

To properly estimate the performance of the complete designed architecture, a Matlab-NS3 simulation platform has been developed by adopting a hybrid discrete-time discrete-event approach. The simulator consists of four main modules.

The first module is the scenario module (NS3 code), which identifies the configuration parameters, such as the simulation duration τ_{sim}, the nominal bit rate β, the number N of MSs per cell, the number L of BSs visible to a nSAT, the number Q of nSATs, the number Q_o of orbital planes, the latitude, longitude, altitude (LLA) coordinates of each BS, the orbital parameters of each nSAT and its buffer size B_{size}. To compute and update the nSAT positions, the widely used orbital model NORAD SGP4 is used [111]. This model takes as input the current time and the standard two-line orbital element set of each satellite to give as output its ECI position and velocity in agreement with the geodesic parameters of the Earth. In the simulated scenario, all nSATs are uniformly distributed among circular orbits and equally spaced within each orbit. Both nSAT ECI and BS LLA positions are converted in ECEF coordinates to compute the CP for the BA-CGR algorithm.

[2]Since the overall work presented in this chapter is the result of a collaboration, the contribution not directly provided by the candidate, which concerns the BA-CGR algorithm, is included for the completeness of the tratise, but its extensive explanation is reported the appendix.

Table 6.3: Application parameters.

$\tau_{sim} = 24$ hrs	$\beta = 535$ Mb/s	$Q = 60$
$Q_o = 4$	$\varrho_B = 1000$	$\varrho_P = 1250$ bytes
$\tau_B = 1$ hr	$M = 10$	$\varpi = 4$

Table 6.4: Performance as a function of the number of MSs per cell and BSs visible to a nSAT.

		Throughput [Mb/s]		Access delay [s]		Loss rate [%]		
N	L	TU	SU	TU	SU	TU	SU	Buffer
5	5	133.06	126.09	0.01	0.06	0.00	0.00	0.00
10	5	258.88	126.23	0.01	0.12	0.00	0.00	0.00
15	5	355.62	126.31	0.01	0.19	0.00	0.00	0.00
20	5	389.72	126.25	0.01	0.26	0.41	0.05	0.00
5	10	133.00	224.99	0.01	0.07	0.00	0.05	0.00
5	15	133.03	275.27	0.01	0.09	0.00	0.91	0.00
5	20	133.03	280.43	0.01	0.11	0.00	4.94	0.00

The second module is the traffic module (NS3 code), which allows to define the number of traffic flows and their characteristics. To properly check the introduced functionalities, the considered end-to-end communications involve MS pairs located in cells not simultaneously visible to the same nSAT. In each 5G cell, a single MS generates a burst of ϱ_B packets, each having ϱ_P bytes, with an interarrival time τ_B.

The third module is the discrete-time MAC/PHY module (Matlab code), which implements the DAMA, CSA and CRDSA access schemes described in Section 6.4 in the presence of capture by using the SINR statistics derived in Section 6.3. The time-based approach has been adopted to jointly consider IC and capture during the analysis of the received random access frame of M slots. Besides, a retry limit ϖ has been introduced to improve the reliability of the access procedures. Thus, if a packet/bundle is not correctly received, retransmission is allowed in the subsequent random access frame, for a maximum of ϖ times.

The fourth module is the discrete-event DTN module (NS3 code), which implements the DTN architecture including the BA-CGR algorithm with the BEB presented in Section 6.5. This latter module calls the MAC/PHY one through a specific script once the links between source BS and chosen nSAT and between chosen nSAT and destination BS are active, i.e., when the nSAT becomes visible to the L BSs.

6.6.2 Numerical results

The designed nSAT-5G mmWave architecture is applied to a data transport scenario requiring the delivery, among far devices located in different remote areas, of non-delay-sensitive information (environmental measurements, software updates, ...). Table 6.3 reports the application parameters, which, together with those already set in Tables 6.1 and 6.2, identify the simulated scenario. The nominal bit rate has been selected according to the adopted code-modulation pair, which provides $\beta = \beta_e B_W \cong 535$ Mbits/s, where $\beta_e \cong 1.19$ bits/(s·Hz) denotes the spectral efficiency [110, Tab. 13].

The first set of simulations investigates the impact of N and L for $B_{size} = 1$ Gbyte. The average performance has been evaluated in terms of throughput, delay, and loss rate. Table 6.4 reports the results involving the terrestrial and space uplinks. Furthermore, in the table, the losses due to the channel and the access procedure, are distinguished from those due to the possible overflow of the nSAT buffer. From these results, one may notice that, for a fixed number of BSs (MSs), the increase of N (L) leads to the increase of the throughput at the TU (SU). Besides, as N or L becomes larger, just the SU results affected by a higher delay, while the loss rate at the SU is more sensitive to the increase of the number of BSs. It is interesting to observe that, if the objective is to support a given number of terrestrial traffic flows, that is, to operate with a fixed $N \times L$ product, the selection of a lower L value and a higher N one results preferable in terms of reliability, as it may be noticed by comparing, for example, the overall loss rate at both the TU and SU for the cases 20×5 and 5×20. The opposite choice should be instead made when the objective becomes the reduction of the access delay, which hence represents, for an integrated 5G-nSAT network, one of the benefits provided by the 5G BS densification strategy.

The second set of simulations compares the CGR and BA-CGR algorithms for $N = L = 20$ and different values of the nSAT buffer size (Table 6.5). In this case, to outline the effects of B_{size}, the table reports the sum of the delays due to the medium access, the delay due to the waiting time at the source BS for a nSAT with enough buffer space, the loss rate due to the medium access, and the loss rate due to the nSAT buffer overflow. The results show that, using the BA-CGR algorithm, no buffer losses occur, regardless of the value of B_{size}. Conversely, the usage of the conventional CGR approach leads to not negligible loss rates when the size of the nSAT buffer is reduced, until the achievement of values unacceptable for a non-delay-sensitive application, which is expected to require a certain degree of reliability. The reduced loss rate provided by the BA-CGR is obtained at the expense of a higher waiting time at the BS. However, concerning this issue, two observations may be formulated. Firstly, for non-delay-sensitive services, a reduction of the losses is considerably more important than the strict maintenance of a given delivery time. Secondly, the main impact to the end-to-end delivery time is due to the time required by the satellite to reach the destination, which, on average, is in the order of one hour for the adopted nSAT constellation. A reduction

of this latter quantity, and also, indirectly, of the waiting time inside the BS buffer, would require the introduction of intersatellite communication. This, in turn, would lead to the presence of more contact links, with further potential channel losses and a more elaborated network planning. In this sense, the proposed DTN-based nSAT-5G architecture may represent a useful trade off between reliability and complexity for exploiting the frequency resources of the mmWave band.

6.7 Summary

A complete network architecture for an integrated nSAT-5G mmWave system has been presented. The architecture, which combines the DTN paradigm with the advanced CSA and CRDSA random access schemes, has been specifically studied to manage scenarios characterized by heterogeneity and time-disjoint transient links. The behavior of the system has been carefully evaluated by theoretically estimating the SINR distribution at each mmWave link to properly account for the capture effect during the medium access procedure. Furthermore, a buffer aware CGR algorithm has been developed to jointly consider buffer occupancy constraints and connection planning during the BS-nSAT contact periods. The designed architecture has been applied to a non-delay-sensitive data transport service, whose performance has been evaluated by a properly developed hybrid discrete-time discrete-event Matlab-NS3 simulation platform.

The numerical results have shown that an accurate modeling of the SINR distribution for interfered mmWave terrestrial and satellite links may be obtained by relying on mathematical formulations of limited complexity. Moving from these statistics, the actual behavior of modern random access methods exploiting IC has been investigated in detail, revealing that a proper consideration of the capture event, which intrinsically characterizes any practical receiver, may drastically increase the estimated performance as compared to that evaluated using the classic erasure channel. The simulation of the complete designed DTN architecture, combining coded and repetition-based random access with a novel CGR algorithm avoiding nSAT buffer overflow, has shown that the 5G BS densification strategy may provide benefits in terms of reliability also to heterogeneous mmWave cellular-LEO satellite networks. This aspect, together with the overlapping advances in antenna development and receivers' design, further suggests the possible technological convergence between forthcoming 5G devices and expected Ka-band nanosatellites.

Table 6.5: Performance as a function of the nSAT buffer size.

	Delay [s]				Loss rate [%]			
	Access		BS		Access		Buffer	
B_{size} [Mbytes]	CGR	BA-CGR	CGR	BA-CGR	CGR	BA-CGR	CGR	BA-CGR
1000	0.35	0.35	0.00	0.00	7.09	7.09	0.00	0.00
500	0.35	0.35	0.00	0.00	7.09	7.09	0.00	0.00
250	0.19	0.21	0.00	417.24	6.16	7.07	45.75	0.00
125	0.10	0.21	0.00	834.13	5.80	7.08	70.17	0.00

Chapter 7

Conclusions

This thesis has addressed aspects that are key enablers for future developments in satellite technologies in the millimiter wave domain.

In Chapter 4, a novel receiver operation model based on iterative decoding and interference cancellation, which exploits power diversity through radio capture, named IDIC, has been introduced. Its performance, properly obtained considering imperfect cancellation, have shown improvements up to 31% when compared to CRDSA with ideal SIC. The study suggests that the opportunity of sending multiple burst copies, as done by repetition-based schemes, may be tightly connected to the combined assumptions of perfect interference cancellation and perfect power control. Beside the improved throughput, the specific IDIC-1 receiver, which operates in the presence of a unique burst copy, yields the advantage of being backward compatible with legacy SIC-enabled FSA systems.

Chapter 5 has concerned the implementation of a reconfigurable antenna array operating in the Ka-band suitable for CubeSats. The obtained results confirm the suitability of this kind of technology for the considered platform, and support the conclusion that the flexibility of arrays in providing advanced functionalities combined with the recent innovations in the other related CubeSat technologies, such as ADCSs and miniaturized Ka-band transponders, may represent a really inviting opportunity to accomplish multi-task missions at reasonable costs and reduced deployment risks.

In Chapter 6, a complete network architecture integrating nanosatellites and 5G systems has been presented. It combines the DTN paradigm with the advanced CSA and CRDSA random access schemes, and has been specifically studied to manage scenarios characterized by heterogeneity and time-disjoint transient links. The behavior of the system has been carefully evaluated by theoretically estimating the SINR distribution at each mmWave link to properly account for the capture effect during the medium access procedure. Numerical results show that an accurate modeling of the SINR distribution for interfered mmWave terrestrial and satellite links may be obtained by relying on mathematical formulations of limited complexity. The simulation of

the complete designed DTN architecture has been carried out with a hybrid discrete-time discrete-event Matlab-NS3 simulation platform, showing that the 5G BS densification strategy may provide benefits in terms of reliability also to heterogeneous mmWave cellular-LEO satellite networks.

The three addressed topics are expected to have a growing importance in forthcoming generations of telecommunications in the millimiter wave domain, suggesting the possible technological convergence between forthcoming 5G devices and expected Ka-band nanosatellites.

Appendix A

Proof of Proposition 1

As a first step, consider the r.v. P_n, describing the power received by B_L from M_n. According to (6.5), P_n may be expressed as a product between r.v.s:

$$P_n = W_n \cdot \Xi, \tag{A.1}$$

where $W_n = \chi_\mathrm{E}/R_n^2$ accounts for the random $\mathrm{M}_n - \mathrm{B}_L$ distance R_n, and Ξ has pdf [2]:

$$f_\Xi(\xi) = \frac{1}{\sqrt{2\pi}\sigma\xi} e^{-\frac{\log^2 \xi}{2\sigma^2}} \mathbb{1}_{\mathbb{R}^+}(\xi), \tag{A.2}$$

in which $\mathbb{1}_X(x)$ is the indicator function (that is, $\mathbb{1}_X(x) = 1$ if $x \in X$ and $\mathbb{1}_X(x) = 0$ if $x \notin X$), and $\mathbb{R}^+$ is the set of positive reals. The cumulative distribution function (cdf) $F_{W_n}(w_n)$ of the r.v. W_n may be evaluated recalling the cdf of R_n for a u.d. of MSs in a disk of radius R_c [112]:

$$F_{R_n}(r_n) = \mathbb{1}_{(R_\mathrm{c}, +\infty)}(r_n) + \left(\frac{r_n}{R_\mathrm{c}}\right)^2 \mathbb{1}_{[0, R_\mathrm{c}]}(r_n). \tag{A.3}$$

By inverting W_n with respect to R_n and substituting the result in (A.3) one in fact obtains:

$$F_{W_n}(w_n) = 1 - F_{R_n}\left(\sqrt{\frac{\chi_\mathrm{E}}{w_n}}\right) = \left(1 - \frac{\chi'_\mathrm{E}}{w_n}\right) \mathbb{1}_{[\chi'_\mathrm{E}, +\infty)}(w_n), \tag{A.4}$$

where $\chi'_\mathrm{E} = \chi_\mathrm{E}/R_\mathrm{c}^2$. Now, using the product distribution [113], and then deriving the result, the cdf and the pdf of P_n may be expressed, respectively, as:

$$F_{P_n}(p_n) = \int_0^{+\infty} f_\Xi(\xi) F_{W_n}\left(\frac{p_n}{\xi}\right) \mathrm{d}\xi = \frac{I_0(p_n) - I_1(p_n)}{2} \mathbb{1}_{\mathbb{R}^+}(p_n), \tag{A.5}$$

$$f_{P_n}(p_n) = \frac{\mathrm{d}F_{P_n}}{\mathrm{d}p_n} = \frac{I_1(p_n)}{2p_n} \mathbb{1}_{\mathbb{R}^+}(p_n), \tag{A.6}$$

where the function $I_j(x)$ is defined in (6.8).

As a second step, consider the r.v. S, describing the SINR at B_L for the target MS M_N in the presence of $N-1$ interfering MSs. According to (6.6), S is a ratio between r.v.s:

$$S = \frac{P_N}{U}, \tag{A.7}$$

where the undesired (interference-plus-noise) power U is approximated, for $N \geq 2$, by considering the power incoming from the nearest interferer scaled by the harmonic number of order $N-1$, denoted as H_{N-1} [112]. This yields:

$$U = \sum_{n=1}^{N-1} P_n + \rho_{\mathrm{E}} \approx H_{N-1} \max\{P_1, \ldots, P_{N-1}\} + \rho_{\mathrm{E}}. \tag{A.8}$$

This approximation allows one to avoid unpractical convolution powers, since the cdf of U may be estimated using the rules for the maximum, scaling, and translation of r.v.s as [113]:

$$F_U(u;N) \cong F_{P_n}^{N-1}\left(\frac{u-\rho_{\mathrm{E}}}{H_{N-1}}\right). \tag{A.9}$$

Denoting as $f_U(u;N)$ the pdf of U, the ccdf of S is thus derived by (A.7) and (A.9) as:

$$\begin{aligned}\bar{F}_S^{\mathrm{TU}}(s;N) &= \Pr\{S > s\} = \Pr\{U \leq P_N/s\} = \int_0^{+\infty} f_{P_N}(p_N) \left[\int_0^{p_N/s} f_U(u;N)\mathrm{d}u\right] \mathrm{d}p_N \\ &= \int_0^{+\infty} f_{P_N}(p_N) F_U\Big(\frac{p_N}{s};N\Big)\mathrm{d}p_N = \int_0^{+\infty} f_{P_N}(p_N)\, F_{P_n}^{N-1}\left(\frac{p_N - s\rho_{\mathrm{E}}}{sH_{N-1}}\right)\mathrm{d}p_N.\end{aligned} \tag{A.10}$$

Using (A.5) and (A.6) in (A.10), one finally obtains (6.7), which holds also for the case $N = 1$ provided that one defines $H_0 = 1$ for calculation purposes. □

Appendix B

Proof of Proposition 2

As a first step, consider the r.v. R_l, denoting the slant range dependent of the r.v. Θ_l that describes the elevation angle. The cdf of Θ_l, which has been derived in [105], may be written as:

$$F_{\Theta_l}(\theta_l) = \mathbb{1}_{[\bar{\theta}_1,+\infty)}(\theta_l) - \frac{1}{\zeta}\arccos\left\{\frac{\cos[\gamma(\theta_l)]}{\bar{\eta}_2}\right\}\mathbb{1}_{[\bar{\theta}_1,\bar{\theta}_2]}(\theta_l), \tag{B.1}$$

where $\gamma(x)$ is given by (6.3). By inverting (6.10) with respect to the elevation angle, one may determine the cdf of R_l from:

$$F_{R_l}(r_l) = F_{\Theta_l}\left[\arcsin\left(\frac{h^2+2hR_{\mathrm{E}}-r_l^2}{2r_lR_{\mathrm{E}}}\right)\right]. \tag{B.2}$$

As a second step, consider the r.v. P_l, describing the power received by S_q from B_l. According to (6.11), $P_l = W_l \cdot \Psi$ is a product between r.v.s, where $W_l = \chi_{\mathrm{S}}/R_l^2$ and Ψ has pdf:

$$f_{\Psi}(\psi) = \frac{m^m}{\Gamma(m)}\psi^{m-1}e^{-m\psi}\,\mathbb{1}_{\mathbb{R}^+}(\psi), \tag{B.3}$$

in which m is the Nakagami parameter and $\Gamma(\cdot)$ is the gamma function. The cdf $F_{W_l}(w_l)$ of the r.v. W_l can be derived similarly to the cdf of W_n for the TU, since the two r.v.s formally have the same relationship with the respective distances. Exploiting this similarity, and subsequently using (6.3), (B.1), (B.2), after some algebra one obtains:

$$\begin{aligned} F_{W_l}(w_l) &= 1 - F_{R_l}\left(\sqrt{\frac{\chi_{\mathrm{S}}}{w_l}}\right) = 1 - F_{\Theta_l}\left\{\arcsin\left[\frac{w_l(h^2+2hR_{\mathrm{E}})-\chi_{\mathrm{S}}}{2R_{\mathrm{E}}\sqrt{\chi_{\mathrm{S}}w_l}}\right]\right\} \\ &= -\frac{1}{\zeta}\arccos\left\{\frac{1}{\bar{\eta}_2}\left[1-\frac{\chi_{\mathrm{S}}-h^2w_l}{2R_{\mathrm{E}}(R_{\mathrm{E}}+h)w_l}\right]\right\}\mathbb{1}_{[\bar{w}_1,\bar{w}_2]}(w_l)+\mathbb{1}_{[\bar{w}_1,+\infty)}(w_l), \end{aligned} \tag{B.4}$$

where $\bar{w}_i = \chi_{\mathrm{S}}\sin^2\bar{\theta}_i/[\bar{\eta}_i(R_{\mathrm{E}}+h)-R_{\mathrm{E}}]^2$ for $i=1,2$. Unfortunately, in this case the product distribution does not directly provide the cdf of P_l in closed-form.

However, an approximate expression for (B.4) may be derived for $m = 1, 2$ by observing that, for LEO satellites, the conditions $h << R_{\mathrm{E}}$ and $\chi_{\mathrm{S}} << R_{\mathrm{E}}(R_{\mathrm{E}}+h)w_l$ usually hold. This implies that the argument of the arccosine function in (B.4) may be assumed close to one, and hence one may adopt the approximation $\arccos x \cong \sqrt{2(1-x)}$, which, once applied to (B.4), leads to:

$$F_{W_l}(w_l) \cong -\frac{\sqrt{2}}{\zeta}\sqrt{1-\frac{1}{\bar{\eta}_2}\left[1-\frac{\chi_{\mathrm{S}}-h^2 w_l}{2R_{\mathrm{E}}(R_{\mathrm{E}}+h)w_l}\right]}\ \mathbb{1}_{[\bar{w}_1,\bar{w}_2]}(w_l)+\mathbb{1}_{[\bar{w}_1,+\infty)}(w_l). \tag{B.5}$$

Now, using the product distribution with (B.5) and (B.3) for $m = 1, 2$, and then deriving the result, one can evaluate after some manipulations the cdf and the pdf of P_l, respectively, as:

$$F_{P_l}(p_l) = \int_0^{+\infty} f_{\Psi}(\psi) F_{W_l}\left(\frac{p_l}{\psi}\right) \mathrm{d}\psi \cong [V_0(p_l)+1]\,\mathbb{1}_{\mathbb{R}^+}(p_l), \tag{B.6}$$

$$f_{P_l}(p_l) = \frac{\mathrm{d}F_{P_l}}{\mathrm{d}p_l} \cong V_1(p_l)\mathbb{1}_{\mathbb{R}^+}(p_l), \tag{B.7}$$

where the function $V_j(x)$ is defined in (6.15).

As a final step, consider the r.v. S, describing the SINR at the nSAT for the target BS B_L in the presence of $L-1$ interfering BSs. Since (6.13) and (6.6) are formally similar, the ccdf of S at the SU may be inferred from (A.10) with the formal replacements $N \to L$, $n \to l$, and $\rho_{\mathrm{E}} \to \rho_{\mathrm{S}}$. This yields:

$$\bar{F}_S^{\mathrm{SU}}(s;L) \cong \int_0^{+\infty} f_{P_L}(p_L)\, F_{P_l}^{L-1}\left(\frac{p_L - s\rho_{\mathrm{S}}}{sH_{L-1}}\right) \mathrm{d}p_L, \tag{B.8}$$

from which, by (B.6) and (B.7), one finally obtains (6.14). □

Appendix C

Proof of Proposition 3

As a first step, the pdf of S may be evaluated by taking the opposite of the derivative of the ccdf in (6.7) and then applying the substitution $x = (p_N - s\rho_E)/(sH_{N-1})$ in the remaining integral. Subsequently, observing that (6.8) approaches zero for $x \to 0^+$, one obtains (6.26).

As a second step, consider the r.v. Λ_k, describing the information rate for the k-th segment. By inverting (6.20), the ccdf and pdf of Λ_k may be calculated as:

$$\bar{F}_{\Lambda_k}(\lambda_k) = \bar{F}_S^{\mathrm{TU}} \left\{ \frac{2b}{a_1^{\frac{1}{a_2}}} \left[\log\left(1 - \frac{\lambda_k}{2}\right) - a_3 \right]^{\frac{1}{a_2}} ; N_k \right\}, \tag{C.1a}$$

$$f_{\Lambda_k}(\lambda_k) = -\frac{\mathrm{d}\bar{F}_{\Lambda_k}}{\mathrm{d}\lambda_k} = \frac{2b}{a_2 a_1^{\frac{1}{a_2}} (2 - \lambda_k)} \left[\log\left(1 - \frac{\lambda_k}{2}\right) - a_3 \right]^{\frac{1}{a_2} - 1} \cdot f_S^{\mathrm{TU}} \left\{ \frac{2b}{a_1^{\frac{1}{a_2}}} \left[\log\left(1 - \frac{\lambda_k}{2}\right) - a_3 \right]^{\frac{1}{a_2}} ; N_k \right\}. \tag{C.1b}$$

As a final step, consider the r.v. Λ, representing the average rate, whose ccdf $\bar{F}_\Lambda(\lambda)$, according to (6.21), may be calculated by performing $K-1$ convolutions $\bar{F}_{\Lambda_K}(\lambda_K) * f_{\Lambda_{K-1}}(\lambda_{K-1}) * ... * f_{\Lambda_1}(\lambda_1)$ and then scaling by K. Besides, remembering that a packet is successfully received when $\lambda \geq \bar{\lambda}$, its success probability is $\bar{F}_\Lambda(\bar{\lambda})$ and can hence be calculated as:

$$C^{\mathrm{TU}}(\bar{\lambda}; N_1, ..., N_K) \cong \int_0^{+\infty} ... \int_0^{+\infty} \bar{F}_{\Lambda_k}\left(K\bar{\lambda} - \sum_{k=1}^{K-1} \lambda_k \right) \cdot \prod_{k=1}^{K-1} f_{\Lambda_k}(\lambda_k) \mathrm{d}\lambda_1 ... \mathrm{d}\lambda_{K-1}, \tag{C.2}$$

which, by (C.1) with $s_k = 2b \left\{ \left[\log(1-\lambda_k/2) - a_3 \right] / a_1 \right\}^{\frac{1}{a_2}}$ for $k = 1, ..., K-1$, finally provides (6.23). □

Appendix D

Buffer Aware Contact Graph Routing (BA-CGR) algorithm

The CGR algorithm is one of the typical solutions for solving the routing problem in satellite DTN networks [114]. Its operations rely on the exploitation of the full information about the future contacts by computing efficient routes through which the bundles may be forwarded between source and destination endpoints. Thus, CGR is specifically designed for use in networks where changes in connectivity are planned and scheduled rather than predicted, discovered, or contemporaneously asserted. To this aim, a global CP is constructed and distributed in advance to all DTN nodes. The CP represents a time-ordered list of scheduled contacts, in which each event is an assertion that a transmission between a node pair at a certain nominal transmission rate will begin and end at fixed times [104]. This assertion implicitly defines the volume of the contact, that is, the maximum amount of data that can be transferred during the contact. Given a CP, each DTN node locally constructs a contact graph data structure, which contains, for each other node of the network, a list of objects. Each object encapsulates start time, end time, and data transmission rate of each contact. A route for a given bundle is defined as a sequence of contacts such that: the first contact is from the bundle's source node to some other node, the subsequent contacts are from the receiving node of the previous contact to some other node, and the last contact is from some node to the bundle's destination node, without loops. In the original version of CGR, each intermediate node calculates its own graph and makes its own decision minimizing the bundle delivery time, even if other metrics have been proposed [114]. The here presented BA-CGR extension considers, beside the bundle delivery time, the nSAT buffer occupancy in order to manage a heterogeneous DTN scenario characterized by long latencies and possible losses.

In the BA-CGR algorithm, each data bundle b (Type $= 0$) may be scheduled for upload by B_L considering an already or forthcoming visible nSAT. In particular, to reduce both the delivery time and the possible losses due

Algorithm 2: BA-CGR algorithm

Input: B' - destination base station; b_{size} - size of the bundle b;
Output: NH_b next hop for the bundle b;

$\mathcal{RP}_b$: set of possible routing paths for the bundle b; RP_Y^b: choosen routing path for the bundle b;
$\mathcal{RP}_b \leftarrow CalculateRoutingPaths\ (B', b_{size})$;
$RP_Y^b \leftarrow ChooseRoutingPath\ (\mathcal{RP}_b)$;
$NH_b = RP_Y^b[0]$;

Algorithm 3: Function CalculateRoutingPaths

CRP - routing path under construction; ST_z, ET_z, ACV_z, NH_z - start time, end time, available contact volume, and next hop of z-th row of B_l's CP, respectively; $b_{lifetime}$ - bundle b lifetime; TX_b - transmission time of bundle b;
function $CalculateRoutingPaths\ (B_l, b_{size})$;
foreach row z in the B_l's CP **do**
    if $(\ (ST_z \leq (b_{lifetime} - TX_b))\ \&\ (T_{now} \leq (ET_z - TX_b))\ \&\ (b_{size} \leq ACV_z)\ )$ **then**
        if (NH_z is not already in CRP) **then**
            if (NH_z is B_L) **then**
                if ($b_{size} \leq NH_z$ free buffer size) **then**
                    add $CRP \rightarrow \mathcal{RP}_b$;
            else
                add $NH_z \rightarrow CRP$;
                $CalculateRoutingPaths\ (NH_z, b_{size})$;
return $\mathcal{RP}_b$;

Algorithm 4: Function ChooseRoutingPath

$FHST_y^b$ - routing path RP_y^b's first hop start time;
foreach routing path RP_y^b in $\mathcal{RP}_b$ **do**
    if ($FHST_y^b$ is the lowest) **then**
        $RP_Y^b = RP_y^b$;
Update all RP_Y^b links' ACVs taking into account bundle b transmission;
return RP_Y^b;

to buffer overflow, B_L selects a nSAT S_q for the upload of b by jointly exploiting the known a priori information about the nSATs movement, that is, the timing information about contacts between nSATs and BSs, and the dynamically changing information about the nSAT buffer occupancy. To clarify this operation, consider the next hop choice procedure for a data bundle b reported in Algorithm 2. Through the CP stored inside its memory, B_L is aware of all contacts between BSs and nSATs during all network lifetime, including start times STs, end times ETs, and available contact volumes $ACVs$ (Algorithm 3). Exploiting this information, the BS B_L calls the function *CalculateRoutingPaths*, which scans the B_L's CP by computing each possible path RP_y^b between B_L and B', that is, by computing all pairs of links $B_L - S_q$ and $S_q - B'$ for $q = 1, \ldots, Q$, that can be exploited to send b from B_L to B'. The computation starts from the last hop, i.e., B', and proceeds backward to B_L. The $B_L - S_q$ link is exploitable if it is not ended yet and its available contact volume is greater than the size b_{size} of the bundle b. The $S_q - B'$ link is exploitable if its end time is higher than the transmission time TX_b of b through the $B_L - S_q$ link and its available contact volume is greater than b_{size}. After computing the complete set of possible paths $\mathcal{RP}_b$ for b, B_L calls the function *ChooseRoutingPath* to choose the path RP_Y^b that allows b to reach B' with the lowest delivery time. If the first hop of RP_Y^b (S_q) is already in contact with B_L, B_L checks if S_q has enough free space in its buffer to receive b avoiding buffer overflow. If this condition is satisfied, b is uploaded on S_q for the subsequent downloading to B'. If S_q is not visible to B_L, B_L waits for the next $B_L - S_q$ contact. Once the nSAT selection is completed, the CP of B_L is consequently updated. Observe that, the start and end contact times are fixed and a priori known, but the nSAT buffer occupancies change depending on the traffic flows. Therefore, at the beginning of each contact, the nSAT sends to B_L a bundle, called status bundle (Type $= 1$), which contains information about the amount of data stored inside the nSAT buffer for each destination BS in order to make B_L aware of the nSAT free storage space. By this improvement, the BA-CGR algorithm enables the data exchange among 5G MSs located in different cells through a nSAT constellation, accounting for delivery time reduction and buffer overflow avoidance.

Bibliography

[1] H. Heidt, J. Puig-Suari, A. Moore, S. Nakasuka, and R. Twiggs, "CubeSat: A New Generation of Picosatellite for Education and Industry Low-Cost Space Experimentation", *AIAA/USU Conference on Small Satellites*, Aug. 2000.

[2] M.R. Akdeniz, Y. Liu, M.K. Samimi, S. Sun, S. Rangan, T.S. Rappaport, and E. Erkip, "Millimeter wave channel modeling and cellular capacity evaluation", *IEEE J. Sel. Areas Commun.*, vol. 32, no. 6, pp. 1164–1179, Jun. 2014.

[3] G. Peters, "Satellite delivery of next generation broadband access to the UK", in *2010 5th Advanced Satellite Multimedia Systems Conference and the 11th Signal Processing for Space Communications Workshop*, IEEE, Sep. 2010, pp. 141–146, ISBN: 978-1-4244-6831-7.

[4] J.G. Andrews, S. Buzzi, W. Choi, S.V. Hanly, A. Lozano, A.C.K. Soong, and J.C. Zhang, "What will 5G be?", *IEEE J. Sel. Areas Commun.*, vol. 32, no. 6, pp. 1065–1082, Jun. 2014.

[5] N. Abramson, "The ALOHA System – Another Alternative for Computer Communication", in *Proceedings of the AFIPS Fall Joint Computer Conference*, ser. AFIPS '70 (Fall), vol. 37, New York, NY, USA: ACM, 1970, pp. 281–285.

[6] L. G. Roberts, "ALOHA Packet System with and Without Slots and Capture", *SIGCOMM Comput. Commun. Rev.*, vol. 5, no. 2, pp. 28–42, Apr. 1975, ISSN: 0146-4833.

[7] G. Choudhury and S. Rappaport, "Diversity ALOHA–A Random Access Scheme for Satellite Communications", *IEEE Transactions on Communications*, vol. 31, no. 3, pp. 450–457, Mar. 1983, ISSN: 0096-2244.

[8] S. Sen, N. Santhapuri, R. R. Choudhury, and S. Nelakuditi, "Successive interference cancellation: A back-of-the-envelope perspective", in *9th ACM SIGCOMM W. on Hot Topics in Networks (Hotnets-IX)*, 2010.

[9] M. Berioli, G. Cocco, G. Liva, and A. Munari, "Modern Random Access Protocols", *Foundations and Trends® in Networking*, vol. 10, no. 4, pp. 317–446, 2016, ISSN: 1554-057X.

[10] P. Patel and J. Holtzman, "Analysis of a Simple Successive Interference Cancellation Scheme in a DS/CDMA System", *IEEE Journal on Selected Areas in Communications*, vol. 12, no. 5, pp. 796–807, 1994, ISSN: 07338716.

[11] A. Zanella and M. Zorzi, "Theoretical Analysis of the Capture Probability in Wireless Systems with Multiple Packet Reception Capabilities", *IEEE Transactions on Communications*, vol. 60, no. 4, Apr. 2012.

[12] G. Liva, "Graph-Based Analysis and Optimization of Contention Resolution Diversity Slotted ALOHA", vol. 59, no. 2, Feb. 2011.

[13] E. Casini, R. De Gaudenzi, and O. del Rio Herrero, "Contention Resolution Diversity Slotted ALOHA (CRDSA): An Enhanced Random Access Scheme for Satellite Access Packet Networks", *IEEE Trans. Wireless Commun.*, vol. 6, no. 4, pp. 1408–1419, Apr. 2007.

[14] G. Liva, "A slotted ALOHA scheme based on bipartite graph optimization", *Source and Channel Coding (SCC), 2010 International ITG Conference on*, pp. 1–6, 2010.

[15] G. Liva, E. Paolini, and M. Chiani, "High-throughtput random access via codes on graphs", *2010 Future Network & Mobile Summit*, pp. 1–8, 2010.

[16] E. Paolini, C. Stefanovic, G. Liva, and P. Popovski, "Coded random access: applying codes on graphs to design random access protocols", *IEEE Communications Magazine*, vol. 53, no. 6, pp. 144–150, 2015, ISSN: 0163-6804.

[17] E. Paolini, M. P. C. Fossorier, and M. Chiani, "Generalized and Doubly Generalized LDPC Codes With Random Component Codes for the Binary Erasure Channel", *IEEE Transactions on Information Theory*, vol. 56, no. 4, pp. 1651–1672, Apr. 2010, ISSN: 0018-9448.

[18] A. Meloni and M. Murroni, "Random Access in DVB-RCS2: Design and Dynamic Control for Congestion Avoidance", *IEEE Transactions on Broadcasting*, vol. 60, no. 1, pp. 16–28, Mar. 2014, ISSN: 0018-9316.

[19] R. De Gaudenzi and O. del Rio Herrero, "Advances in Random Access protocols for satellite networks", in *2009 International Workshop on Satellite and Space Communications*, IEEE, Sep. 2009, pp. 331–336, ISBN: 978-1-4244-4384-0.

[20] E. Paolini, G. Liva, and M. Chiani, "Coded Slotted ALOHA: A Graph-Based Method for Uncoordinated Multiple Access", *IEEE Trans. Inf. Theory*, vol. 61, no. 12, pp. 6815–6832, Dec. 2015.

[21] E. Paolini, G. Liva, and M. Chiani, "High Throughput Random Access via Codes on Graphs: Coded Slotted ALOHA", in *2011 IEEE International Conference on Communications (ICC)*, IEEE, Jun. 2011, pp. 1–6, ISBN: 978-1-61284-232-5.

[22] M. Di Renzo, "Stochastic geometry modeling and analysis of multi-tier millimeter wave cellular networks", *IEEE Trans. Wireless Commun.*, vol. 14, no. 9, pp. 5038–5057, Sep. 2015.

[23] M.K. Samimi, G.R. Mac Cartney Jr., S. Sun, and T.S. Rappaport, "28 GHz millimeter-wave ultrawideband small-scale fading models in wireless channels", in *IEEE VTC Spring*, 2016.

[24] J. Ko, K. Lee, Y.-J. Cho, S. Oh, S. Hur, N.-G. Kang, J. Park, D.-J. Park, and D.-H. Cho, "Feasibility study and spatial–temporal characteristics analysis for 28 GHz outdoor wireless channel modelling", *IET Commun.*, vol. 10, no. 17, pp. 2352–2362, Nov. 2016.

[25] *IEEE Std for High Rate WPANs MAC/PHY Specific. Amend. 2: Millimeter Wave Based Alternative PHY Ext.* IEEE 802.15.3c, Oct. 2009.

[26] *IEEE Std for WLAN MAC/PHY Specific. Amend. 3: Enhanc. for Very High Throughput in the 60 GHz Band*, IEEE 802.11ad, 2014.

[27] Y. Zhang and J. Ge, "Performance analysis for non-orthogonal multiple access in energy harvesting relaying networks", *IET Commun.*, vol. 11, no. 11, pp. 1768–1774, Aug. 2017.

[28] L.G. Roberts, "ALOHA packet systems with and without slots and capture", ARPANET System Note 8 (NIC11290), Tech. Rep., 1972.

[29] F. Babich, M. Comisso, A. Crismani, and A. Dorni, "On the design of MAC protocols for multi-packet communication in IEEE 802.11 heterogeneous networks using adaptive antenna arrays", *IEEE Trans. Mobile Comput.*, vol. 14, no. 11, pp. 2332–2348, Nov. 2015.

[30] S. Grahn, "VIKING and MAILSTAR: Two Swedish Small Satellite Projects", in *Proceedings of the AIAA/USU Conference on Small Satellites*, 1987.

[31] The CubeSat Program, *CubeSat Design Specification*, 2014.

[32] M.A. Viscio, N. Viola, S. Corpino, F. Stesina, S. Fineschi, F. Fumenti, and C. Circi, "Interplanetary CubeSats system for space weather evaluations and technology demonstration", *Acta. Astronaut.*, vol. 104, pp. 516–525, 2014.

[33] M. Swartwout, *The Long-Threatened Flood of University-Class Spacecraft (and CubeSats) Has Come: Analyzing the Numbers*, 2013.

[34] G. Richardson, K. Schmitt, M. Covert, and C. Rogers, "Small satellite trends 2009-2013", in *Proceedings of the AIAA/USU Conference on Small Satellites*, Logan, UT, 2015.

[35] E. Buchen, "Small Satellite Market Observations", in *Proceedings of the AIAA/USU Conference on Small Satellites*, Logan, UT, 2015.

[36] A. Canabal, R.P. Jedlicka, and A.G. Pino, "Multifunctional phased array antenna design for satellite tracking", *Acta. Astronaut.*, vol. 57, pp. 887–900, 2005.

[37] A. Babuscia, B. Corbin, M. Knapp, R. Jensen-Clem, M. Van de Loo, and S. Seager, "Inflatable antenna for cubesats: Motivation for development and antenna design", *Acta. Astronaut.*, vol. 91, pp. 322–332, 2013.

[38] F. Tubbal, R. Raad, and K. Chin, "A survey and study of planar antennas for pico-satellites", *IEEE Access*, vol. 3, pp. 2590–2612, 2015.

[39] R.E. Hodges, D.J. Hoppe, M.J. Radway, and N.E. Chahat, "Novel deployable reflectarray antennas for CubeSat communications", in *IEEE MTT-S Int. Microw. Symp.*, 2015.

[40] C. A. Balanis, *Antenna Theory: Analysis and Design*, Third. New York: John Wiley & Sons, Inc., 2012, ISBN: 9781118585733.

[41] R. Garg, P. Bhartia, I. Bahl, and A. Ittipiboon, *Microstrip antenna design handbook*. Artech House, 2001, ISBN: 0890065136.

[42] J. Huang, "Microstrip antennas: Analysis, design, and application", in *Modern antenna handbook*, C. A. Balanis, Ed., John Wiley & Sons, Inc., 2008.

[43] D. M. Pozar, "Microstrip antennas", *Proceedings of the IEEE*, vol. 80, no. 1, pp. 79–91, 1992, ISSN: 00189219.

[44] C. A. Balanis, *Antenna theory: analysis and design*, second. New York: John Wiley & Sons, Inc., 1996, ISBN: 0471592684.

[45] M. Kara, "Formulas for the computation of the physical properties of rectangular microstrip antenna elements with various substrate thicknesses", *Microwave and Optical Technology Letters*, vol. 12, no. 4, pp. 234–239, 1996.

[46] M. Kirschning, R. Jansen, and N. Koster, "Accurate model for open end effect of microstrip lines", *Electronics Letters*, vol. 17, pp. 123–125, 1981, ISSN: 00135194.

[47] E. O. Hammerstad, "Equations for Microstrip Circuit Design", *5th European Microwave Conference*, pp. 268–272, 1975.

[48] M. Haneishi and S. Yoshida, "A design method of circularly polarized rectangular microstrip antenna by one-point feed", *Electronics and Communications in Japan (Part I: Communications)*, vol. 64, no. 4, pp. 46–54, 1981.

[49] T. Teshirogi, M. Tanaka, and W. Chujo, "Wideband circularly polarized array antenna with sequential rotations and phase shift of elements", in *Antennas and Propagation Society International Symposium*, 1985, pp. 117–120.

[50] J. Huang, "A technique for an array to generate circular polarization with linearly polarized elements", *IEEE Transactions on Antennas and Propagation*, vol. 34, no. 9, pp. 1113–1124, Sep. 1986.

[51] M. Poian, S. Poles, F. Bernasconi, E. Leroux, W. Steffe, and M. Zolesi, "Multi-objective optimization for antenna design", in *2008 IEEE International Conference on Microwaves, Communications, Antennas and Electronic Systems*, IEEE, May 2008, pp. 1–9, ISBN: 978-1-4244-2097-1.

[52] B. Allen and M. Ghavami, *Adaptive Array Systems*. New York: John Wiley & Sons, Inc., 2005.

[53] G. V. Tsoulos and C. G. Christodoulou, "Arrays and smar antennas", in *Modern antenna handbook*, C. A. Balanis, Ed., John Wiley & Sons, Inc., 2008.

[54] R. L. Haupt, "Genetic Algorithms for Antennas", in *Modern antenna handbook*, C. A. Balanis, Ed., John Wiley & Sons, Inc., 2008.

[55] M. F. Iskander, W. Kim, J. Bell, N. Celik, and Z. You, "Antenna Array Technologies for Advanced Wireless Systems", in *Modern antenna handbook*, C. A. Balanis, Ed., John Wiley & Sons, Inc., 2008.

[56] J. Huang and D. M. Pozar, "Microstrip arrays: Analysis, design, and applications", in *Modern antenna handbook*, C. A. Balanis, Ed., John Wiley & Sons, Inc., 2008.

[57] Haupt, Randy L. and Y. Rahmat-Samii, "Antenna array developments: A perspective on the past, present and future", *IEEE Antennas Propag. Mag.*, vol. 57, no. 1, pp. 86–96, 2015.

[58] *Digital video broadcasting (DVB); Second generation DVB interactive satellite system (DVB-RCS2); Part 2: Lower layers for satellite standard*, ETSI EN 301 545-2 V1.2.1, 2014.

[59] L. Vangelista, A. Zanella, and M. Zorzi, "Long-range iot technologies: The dawn of lora", in *Future Access Enablers for Ubiquitous and Intelligent Infrastructures: First Int. Conf., FABULOUS 2015, Ohrid, Republic of Macedonia, September 23-25, 2015. Revised Selected Papers*, V. Atanasovski and A. Leon-Garcia, Eds. Springer International Publishing, 2015.

[60] F. Babich and M. Comisso, "Including the angular domain in the analysis of finite multi-packet peer-to-peer networks with uniformly distributed sources", *IEEE Trans. Commun.*, vol. 64, no. 6, pp. 2494–2510, Jun. 2016.

[61] H. Inaltekin, S. B. Wicker, and H. V. Poor, "On unbounded pathloss models: effects of singularity on wireless network performance", vol. 27, no. 7, Sep. 2009.

[62] W. Han, J. Ge, and J. Men, "Performance analysis for NOMA energy harvesting relaying networks with transmit antenna selection and maximal-ratio combining over Nakagami-m fading", *IET Commun.*, vol. 10, no. 18, pp. 2687–2693, Dec. 2016.

[63] G.L. Stuber, *Principles of mobile communication*. Norwell MA, Kluwer Academic Publishers, 1996.

[64] M. Wilhelm, V. Lenders, and J. B. Schmitt, "On the reception of concurrent transmissions in wireless sensor networks", vol. 13, no. 12, Dec. 2014.

[65] F. Ricciato and P. Castiglione, "Pseudo-random ALOHA for enhanced collision-recovery in RFID", vol. 17, no. 3, 2013.

[66] *Model SAO-2734030810-28-S1: Full Ka-Band Omnidirectional Antenna, 360 Degree, 7.5 dBi Gain*.

[67] S. Toumpis and A.J. Goldsmith, "Capacity regions for wireless ad hoc networks", *IEEE Trans. Wireless Commun.*, vol. 2, no. 4, pp. 736–748, Jul. 2003.

[68] S. Singh, R. Mudumbai, and U. Madhow, "Interference analysis for highly directional 60-GHz mesh networks: The case for rethinking medium access control", *IEEE/ACM Trans. Netw.*, vol. 19, no. 5, pp. 1513–1527, Oct. 2011.

[69] *CubeSat design specif.: Rev. 13*, California Polytech. State Univ., 2015.

[70] J. A. King, J. Ness, G. Bonin, M. Brett, and D. Faber, "Nanosat Ka-Band Communications - A Paradigm Shift in Small Satellite Data Throughput", in *Proceedings of the AIAA/USU Conference on Small Satellites*, Logan, UT, 2012.

[71] B. Klofas and K. Leveque, "The Future of CubeSat Communications: Transitioning Away from Amateur Radio Frequencies for High-speed Downlinks", in *AMSAT Space Symposium*, Orlando, Fl, 2012.

[72] J.F. Sauder, N. Chahat, R. Hodges, E. Peral, Y. Rahmat-Samii, and M. Thomson, "Designing, building, and testing a mesh Ka-band parabolic deployable antenna (KaPDA) for CubeSat", in *AIAA Aerospace Sciences Meet.*, 2015.

[73] J.A. King, K. Leveque, M. Bertino, J. Kim, and H. Aghahassan, "Ka-band for CubeSats", in *AIAA/USU Conf. Small Satellites*, 2015.

[74] A. Babuscia, K.-M. Cheung, D. Divsalar, and C. Lee, "Development of cooperative communication techniques for a network of small satellites and CubeSats in deep space: The SOLARA/SARA test case", *Acta. Astronaut.*, vol. 115, pp. 349–355, 2015.

[75] C. Underwood, S. Pellegrino, V.J. Lappas, C.P. Bridges, and J. Baker, "Using CubeSat/micro-satellite technology to demonstrate the Autonomous Assembly of a Reconfigurable Space Telescope (AAReST)", *Acta. Astronaut.*, vol. 114, pp. 112–122, 2015.

[76] PicoSaTs CubeSat Enterprise, last access: Feb. 21rd, 2017.

[77] R. Martinez Rodriguez-Osorio and E. Fueyo Ramírez, "A hands-on education project: Antenna design for inter-CubeSat communications", *IEEE Antennas Propag. Mag.*, vol. 54, no. 5, pp. 211–224, 2012.

[78] R. Garg, P. Bhartia, I. Bahl, and A. Ittipiboon, *Microstrip antenna design handbook*. Artech House antennas and propagation library, 2001.

[79] P.S. Hall, J. Huang, E. Rammos, and A. Roederer, "Gain of circularly polarised arrays composed of linearly polarised elements", *Electronics Lett.*, vol. 25, no. 2, pp. 124–125, 1989.

[80] J. Huang, "A Ka-band circularly polarized high-gain microstrip array antenna", *IEEE Trans. Antennas Propag.*, vol. 43, no. 1, pp. 113–116, 1995.

[81] A. Chen, Y. Zhang, Z. Chen, and C. Yang, "Development of a Ka-band wideband circularly polarized 64-Element microstrip antenna array with double application of the sequential rotation feeding technique", *IEEE Antennas Wireless Propag. Lett.*, vol. 10, pp. 1536–1225, 2011.

[82] M. Comisso and R. Vescovo, "Fast iterative method of power synthesis for antenna arrays", *IEEE Trans. Antennas Propag.*, vol. 57, no. 7, pp. 1952–1962, 2009.

[83] G. Buttazzoni and R. Vescovo, "An efficient and versatile technique for the synthesis of 3D copolar and crosspolar patterns of phase-only reconfigurable conformal arrays with DRR and near-field control", *IEEE Trans. Antennas Propag.*, vol. 62, no. 4, pp. 1640–1651, 2014.

[84] *Clyde Space*, last access: Feb. 21rd, 2017.

[85] *Comtech Telecommunications Corp.* last access: Feb. 21rd, 2017.

[86] *Digital Video Broadcasting (DVB); Second generation framing structure, channel coding and modulation systems for broadcasting, interactive services, news gathering and other broadband satellite applications; Part 2: DVB-S2 Extensions*, ETSI DVB-S2X Draft Std, 2014.

[87] *ARTES 5.1 Statement of work: Miniaturised Ka-band FSS transponder for small satellites 5E.001*, European Space Agency, 2015.

[88] M. Mc Nicholas, J. De Luna, R. Manno, and Y.-H. Shu, "Low cost Ka-band transmitter for CubeSat systems", in *IEEE Topic. Work. Internet of Space*, 2017.

[89] *18 GHz Microwave PLL Synthesizer, Analog Devices*, last access: Feb. 21rd, 2017.

[90] *SWIFT-KTX: High Throughput Software-Defined K-band Communications, Tethers Unlimited, Inc.* last access: Feb. 21rd, 2017.

[91] A.C. Ludwig, "A simple graph for determining polarization loss", *Microwave J.*, vol. 19, no. 9, p. 63, 1976.

[92] W.J. Larson and J.R. Wertz, *Space mission analysis and design*. Microcosm Press Springer, 1999.

[93] *ITU-R Propag. models software library*, Centre Nat. Etudes Spatiales, 2010.

[94] M. Jia, X. Gu, Q. Guo, W. Xiang, and N. Zhang, "Broadband hybrid satellite-terrestrial communication systems based on cognitive radio toward 5G", *IEEE Wireless Commun.*, vol. 23, no. 6, pp. 96–106, Dec. 2016.

[95] X. Artiga, J. Núñez-Martínez, A. Pérez-Neira, G.J.L. Vela, and J.M.F. García, "Terrestrial-satellite integration in dynamic 5G backhaul networks", in *IEEE ASMS/SPSC*, 2016.

[96] J. Zhang, X. Zhang, M.A. Imran, B. Evans, Y. Zhang, and W. Wang, "Energy efficient hybrid satellite terrestrial 5G networks with software defined features", *J. Commun. Netw.*, vol. 19, no. 2, pp. 147–161, Apr. 2017.

[97] S. Kim, E. Visotsky, P. Moorut, K. Bechta, A. Ghosh, and C. Dietrich, "Coexistence of 5G with the incumbents in the 28 and 70 GHz bands", *IEEE J. Sel. Areas Commun.*, vol. 35, no. 6, pp. 1254–1268, Jun. 2017.

[98] A. Osseiran *et al.*, *5G mobile and wireless communications technology*. Cambridge Univ. Press, Cambridge, UK, 2016.

[99] V. Cerf, S. Burleigh, A. Hooke, L. Torgerson, R. Durst, K. Scott, K. Fall, and H. Weiss, "Delay-tolerant networking architecture", RFC 4838, Apr. 2007.

[100] K. Fall, "A delay-tolerant network architecture for challenged internets", in *ACM SIGCOMM*, 2003.

[101] C. Caini, H. Cruickshank, S. Farrell, and M. Marchese, "Delay-and disruption-tolerant networking (DTN): an alternative solution for future satellite networking applications", *Proc. IEEE*, vol. 99, no. 11, pp. 1980–1997, Nov. 2011.

[102] S. Jain, K. Fall, and R. Patra, "Routing in a delay tolerant network", in *ACM SIGCOMM*, 2004.

[103] K. Scott and S. Burleigh, "Bundle protocol specification", RFC 5050, Nov. 2007.

[104] S. Burleigh, "Contact graph routing", Internet-Draft, Jul. 2010.

[105] S.-Y. Li and C.H. Liu, "An analytical model to predict the probability density function of elevation angles for LEO satellite systems", *IEEE Commun. Lett.*, vol. 6, no. 4, pp. 138–140, Apr. 2002.

[106] G.D. Gordon and W.L. Morgan, *Principles of communications satellites*. New York, John Wiley and Sons, 1993.

[107] R. Abelló *et al.*, "Low-Earth orbit (LEO) 26 GHz K-band study group final report", Interagency Operat. Advisory Group, Tech. Rep., 2016.

[108] T. Bai and R.W. Heath Jr., "Coverage and rate analysis for millimeter-wave cellular networks", *IEEE Trans. Wireless Commun.*, vol. 14, no. 2, pp. 1100–1114, Feb. 2015.

[109] F. Babich, A. Soranzo, and F. Vatta, "Useful mathematical tools for capacity approaching codes design", *IEEE Commun. Lett.*, vol. 21, no. 9, pp. 1949–1952, Sep. 2017.

[110] *Digital video broadcasting (DVB); Second generation framing structure, channel coding and modulation systems for broadcasting, interactive services, news gathering and other broadband satellite applications (DVB-S2)*, ETSI EN 302 307 V1.2.1, Aug. 2009.

[111] D. Vallado, P. Crawford, R. Hujsak, and T. Kelso, "Revisiting spacetrack report No. 3", AIAA/AAS Astrodynamics Specialist Conference and Exhibit, 2006.

[112] F. Babich and M. Comisso, "A reliable approach for modeling the actual antenna pattern in millimeter-wave communication", *IEEE Commun. Lett.*, vol. 19, no. 8, pp. 1335–1338, Aug. 2015.

[113] R.D. Yates and D.J. Goodman, *Probability and stochastic processes*. New York, John Wiley and Sons, 1999.

[114] G. Araniti, N. Bezirgiannidis, E. Birrane, I. Bisio, S. Burleigh, C. Caini, M. Feldmann, M. Marchese, J. Segui, and K. Suzuki, "Contact graph routing in DTN space networks: Overview, enhancements and performance", *IEEE Commun. Mag.*, vol. 53, no. 3, pp. 38–46, Mar. 2015.

List of Publications

[115] G. Buttazzoni, A. Cuttin, and R. Vescovo, "Design Procedures for Rectangular Patch Antennas", in *2018 12th European Conference on Antennas and Propagation (EuCAP 2018)*, accepted.

[116] F. Babich, M. Comisso, A. Cuttin, and F. Ricciato, "Exploiting capture and interference cancellation for uplink random multiple access in 5g millimeter-wave cellular networks", *IET Communications, Special Issue on Recent Advances on 5G Communications*, under review.

[117] G. Buttazzoni, M. Comisso, A. Cuttin, M. Fragiacomo, R. Vescovo, and R. Vincenti Gatti, "Reconfigurable phased antenna array for extending cubesat operations to Ka-band: Design and feasibility", *Acta Astronautica*, vol. 137, pp. 114–121, 2017, ISSN: 00945765.

[118] F. Babich, M. Comisso, A. Cuttin, M. Marchese, and F. Patrone, "Nanosatellite-5G integration in the millimiter wave domain: A full top-down approach", *IEEE Transactions on Communications*, under review.

[119] F. Babich, M. Comisso, and A. Cuttin, "Uplink Capacity of Interfered Millimeter-Wave Communications: 3D Theoretical Analysis", in *IEEE Global Telecommunications Conference (GLOBECOM)*, Washington, DC, 2016.

[120] ——, "Impact of Interference Spatial Distribution on Line-of-Sight Millimeter-Wave Communications", in *European Wireless 2017*, 2017, pp. 363–368, ISBN: 9783800744268.

[121] G. Buttazzoni, M. Comisso, A. Cuttin, and R. Vescovo, "On the design of an antenna array for CubeSats operating in the Ka-frequency band", in *XXI Riunione Nazionale di Elettromagnetismo*, Parma, 2016.

[122] A. Cuttin, G. Buttazzoni, R. Vescovo, and L. Tenze, "Radiation pattern synthesis of a high gain, circularly polarized rectangular antenna array in the Ka band for CubeSat class satellites", in *Proceedings of the 3rd IAA Conference On University Satellite Missions And Cubesat Workshop*, Roma: International Academy of Astronautics, IAA Book Series, Conference and Symposium Proceedings, 2015.